GEOSYSTEMS ENGINEERING

REVIEW OF THE SEISMIC PERFORMANCE OF STRUCTURES WITH SHALLOW FOUNDATIONS AT LIQUEFIABLE SITES

by

Ava Fathian Sabet, David Silva, Jonathan D. Bray, and Jason T. DeJong

Report No. UCB/GT 2025-01

March 10, 2025

Department of Civil and Environmental Engineering
University of California
Berkeley, California

ABSTRACT

Federal Highway Administration guidelines state shallow foundations are not feasible at sites with liquefiable soils, irrespective of the depth, thickness, or extent of these layers. This restriction results in significant cost implications for retrofitting existing bridges and constructing new ones. Recent studies suggest shallow foundations can be designed to perform satisfactory under specific conditions, particularly at sites with limited liquefaction. Additionally, deep foundations have been shown in some instances to have exacerbated damage during seismic events due to issues such as promoting the manifestation of ejecta at the ground surface. This report summarizes a review of the literature of past field case histories, centrifuge tests, and numerical parametric studies to identify critical parameters and mechanisms that inform the performance of shallow foundations at sites with liquefiable soils.

ACKNOWLEDGEMENTS

This research was supported financially by the California Department of Transportation (Caltrans) through Agreement 65A1138. Additional support was provided by the Faculty Chair in Earthquake Engineering Excellence at UC Berkeley. The findings, opinions, and conclusions presented in this report are those of the authors and do not necessarily reflect the views of the sponsors. The views and conclusions contained in this document are those of the authors and should not be interpreted as necessarily representing the official policies, either expressed or implied, of the U.S. Government or the State of California.

The authors would also like to extend gratitude to Professor Ross Boulanger for providing UC Davis's centrifuge FLAC model and to Professor Katerina Ziotopoulou for providing access to laboratory testing data on Ottawa F65.

Table of Contents

Chapter 1 INTRODUCTION

1.1 Research Motivation

Federal Highway Administration (FHWA) guidelines (e.g., FHWA-RC/TD-10-001 by Samtani et al. 2010) state shallow foundations are not feasible at sites with liquefiable soils, irrespective of the depth, thickness, or extent of these layers. This restriction implies that existing bridges supported by shallow foundations at sites with potential liquifiable layers must either be retrofitted or obtain an exception to policy. For instance, the Morrisson Creek Bridge is situated in an area prone to strong earthquake-induced ground motions. The subsurface profile at this site includes loose to medium-dense granular material below the groundwater table. Under current guidelines, the foundation of the bridge would need to be replaced with piles, which can be prohibitively expensive. Similarly, deep piles are recommended for new bridges at sites with deep or minor liquefiable layers, which adds significant costs. For instance, the San Elijo Lagoon Bridge required piles longer than 60 meters (200 feet) due to potential liquefaction hazards at depths of 27-37 m (90-120 feet).

Recent studies indicate shallow foundations can be designed to perform satisfactorily at sites with limited liquefaction (e.g., Bray & Dashti, 2014). Moreover, deep foundations have, in some instances, exacerbated damage. For example, one bent of the Juan Pablo deep drilled pier foundation sank 0.8 m (2.6 feet) due to liquefaction of soils along the pier, which led to ejecta and subsequent loss of support (Ledezma, et al., 2012). A shallow foundation that did not extend into the deep liquefiable layer might have performed better in this case.

Given this context, a revision of the current guidelines is necessary to provide clear criteria for when shallow foundations can meet performance standards at sites with liquefiable soils. This research aims to study case histories of bridges and buildings with shallow foundations that have experienced strong ground motions at liquefiable sites. It will also examine instances where deep foundations contributed to different types of damage during liquefaction and consider how shallow foundations might have mitigated or reduced these damages. Furthermore, this literature review will explore recent studies that investigate the seismic performance of structures (mostly buildings) with shallow foundations at liquefiable sites to identify concepts and mechanisms that can be transferred to evaluate shallow bridge foundations under similar conditions.

1.2 Liquefaction Settlement Mechanisms

Cyclically-induced pore water pressure generation and liquefaction may produce several mechanisms of foundation movement. Several of the key mechanisms of liquefaction-induced structural settlement are illustrated in Figure 1.1. It is useful to categorize movements as ejecta-induced, shear-induced, or volumetric-induced deformations (Bray & Macedo, Simplified Evaluation of Liquefaction-Induced Building Settlements, 2017).

When liquefaction occurs, ejecta-induced deformations (ε_e) can govern structural settlement (Figure 1.1a). Soil that was supporting the shallow foundations of a structure can be transported from underneath the structure to the ground surface. Hence, this mechanism physically removes soil that was below its foundation. The resulting impacts can be significant and lead to large settlements of structures with shallow foundations.

Shallow-founded structures exert shear stresses in the underlying soil that can produce liquefaction-induced settlement, wherein the structure punches into the surrounding ground. Partial bearing failure under the static load of structures due to cyclic softening/strength loss in the foundation soil can result in punching settlement or tilting of the structure ($\varepsilon_{q\text{-}BC}$) (Figure 1.1b). Cumulative ratcheting foundation displacement due to soil-structure interaction (SSI)-induced cyclic loading near the edges of the foundation ($\varepsilon_{q\text{-}SSI}$) (Figure 1.1c) can be especially damaging, as soil cannot sustain tension, and loading the soil downward after an upward loading is particularly disruptive to the soil fabric.

Volumetric-induced displacement mechanisms are also important. Localized volumetric strains can occur due to partially drained cyclic loading ($\varepsilon_{p\text{-}DR}$) induced by the high transient hydraulic gradients that occur during cyclic loading. Downward displacement of the structure due to sedimentation or solidification after liquefaction or soil structure break-down ($\varepsilon_{p\text{-}SED}$) occurs when a high pore water pressure ratio is reached (Figure 1.1d). Consolidation-induced volumetric strain ($\varepsilon_{p\text{-}CON}$) occurs as excess pore water pressures dissipate and the soil's effective stress increases (Figure 1.1e). This mechanism is present when excess pore water pressure is generated.

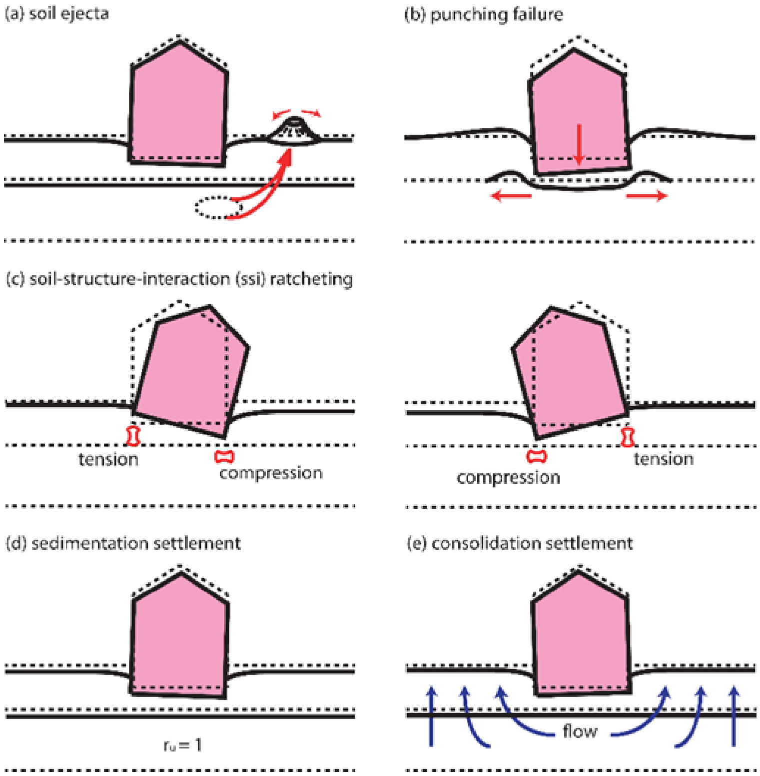

Figure 1-1 Liquefaction-induced displacement mechanisms: (a) ground loss due to soil ejecta; shear-induced settlement from (b) punching failure, or (c) SSI ratcheting; and volumetric-induced settlement from (d) sedimentation or (e) post-liquefaction reconsolidation (from Bray & Macedo, 2017).

One of the primary mechanisms contributing to bridge failures during liquefaction is lateral displacement. Lateral spreading refers to the horizontal movement of the surficial soil downslope of gently sloping ground or toward a free surface due to a reduction in strength in the underlying liquefied soil. This process generates large shear forces at the connections of bridge piers and abutments, as well as compressional forces in the superstructure. These forces can cause bridge decks to push into, through or over abutment walls, or even lead to buckling. In some other cases, the connections may hold tops of piers and abutments in place while the bases are displaced towards the river (Youd, 1993). Lateral displacements can reach several meters on gentle slopes or ground with a free-face, resulting in differential settlements between foundation elements.

Bridges are particularly vulnerable to this type of failure because they are often constructed on floodplain alluvium, which is typically found in areas with high groundwater levels. Floodplain alluvium, being relatively young and unconsolidated, is especially prone to liquefaction. Moreover, the topography of floodplains, with their gentle slopes and incised river channels, further increases the risk of lateral spreading (Youd & Perkins, 1978).

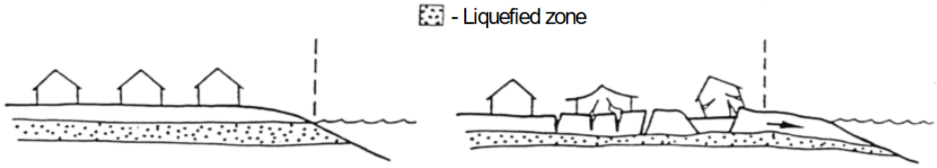

(a) Spreading Towards a Free Face

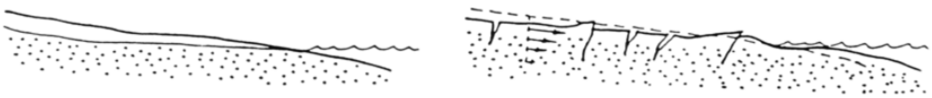

(b) Spreading Downslope or Downgrade

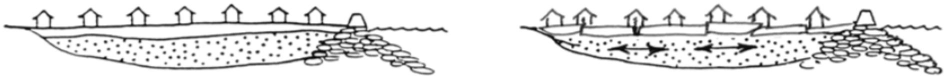

(c) Localized, Non-directionally Preferential Differential Lateral Displacements

Figure 1-2 Examples of modes of liquefaction-induced lateral translation (from Seed et al., 2003).

1.3 Report Organization

This report is organized as follows after this introductory chapter:

- Chapter 2 discusses field case histories of bridges and buildings on shallow foundations during various earthquakes and highlights observed performance and failure mechanisms.
- Chapter 3 summarizes previous experimental studies on shallow-founded structures.
- Chapter 4 explores the analytical methods available for analyzing liquefaction effects on shallow foundation structures. It reviews key studies on this topic, identifies critical parameters and mechanisms, and summarizes lessons learned from previous research.
- Chapter 5 summarizes the key insights gained from this literature review.

Chapter 2 FIELD CASE HISTORIES

2.1 Introduction

Liquefaction-induced ground failure is a major cause of earthquake damage, particularly for bridges. Bridges are especially susceptible to liquefaction since they are often constructed on recently deposited floodplain alluvium in areas with high groundwater tables. The typical floodplain topography, which is characterized by gentle slopes and incised river channels with free-faces, can exacerbate the effects of liquefaction, particularly lateral spreading (Youd, 1993). Case histories consistently show lateral spreading is one of the primary failure mechanisms for bridges during liquefaction events.

This study focuses on cases where lateral spreading has been mitigated using ground improvement techniques or structural reinforcement. However, understanding the mechanisms of bridge failure due to liquefaction-induced lateral spreading remains crucial. Studying instances where bridges have suffered significant damage from lateral spreading can provide valuable insights into failure mechanisms and help inform design and mitigation strategies.

Case histories of liquefaction-induced damage due to settlement without lateral spreading involving bridges are limited. However, insights can be drawn from the performance of buildings on shallow foundations under similar conditions. While buildings and bridges differ in certain aspects, such as natural period, many concepts are transferrable between these case studies. This section is organized into two parts:

1. Lateral Spreading Cases for Bridges: examining cases where bridges were affected by liquefaction-induced lateral spreading.
2. Buildings on Shallow Foundations: highlights cases where buildings on shallow foundations were affected by liquefaction.

By exploring these case histories, the study aims to identify key concepts and failure mechanisms that will guide the focus of subsequent experiments and analyses. This approach ensures a comprehensive understanding of the factors influencing liquefaction-induced damage of different structural systems.

2.2 Field Case Histories of Bridges on Liquefiable Sites

2.2.1 Lateral Spreading

Showa Bridge, 1964 M_w 7.6 Niigata Earthquake, Japan

The June 14, 1964, M_w 7.6 Niigata earthquake occurred at the convergence boundary of the Eurasian and North American plates with a reverse faulting mechanism. The earthquake's epicenter was located about 55 km away from the Showa bridge, which was one of the bridges that collapsed due to the event. The hypocenter of the earthquake was at a depth of about 40 km, and the peak ground acceleration (PGA) was estimated to be between 0.08g and 0.25g based on the intensities measured (Hamada & O'Rourke, 1992). Although the exact dipping direction of the faults remains a topic of debate, the closest rupture distance to the Showa Bridge is estimated to be between 14.5 and 17 km (Bhattacharya, et al., 2014).

Showa Bridge is in Niigata's coastal alluvial plain, which consists of marine sediments formed by currents along the Japan Sea coast and river or lake deposits from the Shinano River. Boring logs from the region indicated that the upper 5-15 m (16-49 ft) soils are typically soft sandy deposits with SPT-N values of less than 10, reflecting a high susceptibility to liquefaction. Due to the high ground water level and analyses conducted, the bridge's collapse has been attributed to extensive liquefaction and lateral spreading. The liquefaction extended to a maximum depth of 10 m (33 ft) below the riverbed and was laterally extensive across the site (Bhattacharya, et al., 2014).

Showa Bridge was a simple steel girder bridge supported by pile foundations. Its total length was about 307 m (1007 ft), with 12 composite girders and a width of approximately 24 m (79 ft). The main span length was about 28 m (92 ft), and the side spans were about 15 m (49 ft). Each supporting pier's foundation consisted of a single row of nine tubular steel piles with a length of 25 m (82 ft) and outer diameter of 0.609 m (2 ft). These piles were connected laterally by a pile cap. The material used for the piles had a yield strength of 315 MPa and the ultimate strength of 490 MPa. Notably, the bridge had been constructed only 15 days before the earthquake which precluded any reduction in material strength due to corrosion. Additionally, the piles were designed with significant longitudinal flexibility (Hamada & O'Rourke, 1992).

Approximately 1-2 minutes after the peak ground acceleration was experienced, the bridge began to fail. Figure 2-1 shows a schematic of the piers after the earthquake. The collapse started with piers P5 and P6 moving in opposite directions, causing girder G5-6 to fall into the water. This initiated a domino effect, resulting in the failure of girders G2-3 through G6-7. Reports indicated liquefaction-induced ground movements contributed to the failure.

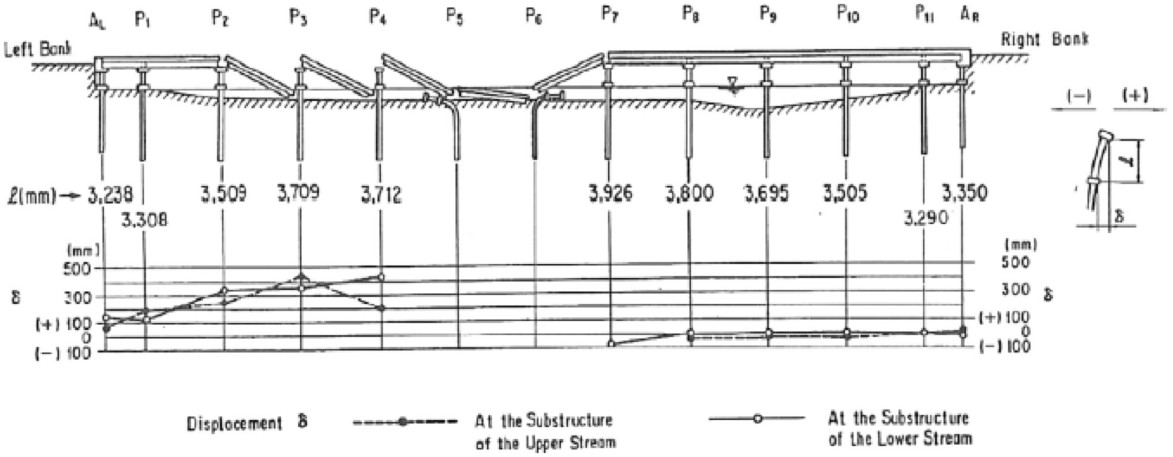

Figure 2-1 Schematic diagram of the collapse of the Showa Bridge along with the deflections of the pile cap (from Bhattacharya et al., 2014).

According to Hamada and O'Rourke (2014), the liquefaction of the ground on the left bank and in the riverbed led to lateral movement towards the river center. This ground displacement continued after the earthquake as excess pore water pressure dissipated. The permanent ground displacement, which reached several meters, deformed the foundation piles and caused the girders to fall, indicating that lateral displacement was the primary cause of the bridge failure.

Developing an alternative hypothesis of the primary cause of the bridge failure, Bhattacharya et al. (2014) later argued that lateral spreading began around 83 seconds after the start of the shaking, while the bridge failed approximately 70 seconds into the main shock. Thus, they claim the bridge failed before significant lateral spreading commenced. They argue piers P5 and P6 would have collapsed in the same direction if lateral spreading had been the main cause of failure. Additionally, piers near the riverbank, where lateral spreading was most severe, did not fail. Their study concluded that resonance between the bridge and the ground motion during the earthquake displaced the piles, which was the primary cause of bridge failure.

Landing Road Bridge, 1987 M_w 6.3 Edgecumbe Earthquake, New Zealand

The March 2, 1987, M_w 6.3 Edgecumbe earthquake occurred on a normal fault. The fault lies beneath the Rangitaiki Plains within the Taupo Volcanic Zone, which is part of the tectonic boundary between the Pacific and Australian plates in the North Island of New Zealand. The hypocenter was estimated to be at a depth of 8 km, and the closest distance to rupture from the Landing Road Bridge site was estimated to be 8 km. The Landing Road Bridge experienced moderate damage due to lateral ground displacement triggered by the seismic event. Ground motion recordings from the nearest strong motion station (SMS) indicated a PGA of 0.33 *g* at the base of an 80-m (262 ft) high rockfill dam. Considering the site characteristics of the dam and bridge, it is likely that the shaking levels at the Landing Road Bridge site were comparable to this recorded motion (Berrill et al., 2001).

Due to the migration of the river over the years, the bridge was located on a point-bar structure comprised of loose, medium to coarse sands extending to a depth of 6 m (20 ft), overlaid by about 1-2 m (3 to 6.5 ft) of floodplain silts and clays. Laterally accreted sands such as those found in point-bars are highly susceptible to liquefaction. Cone penetration test (CPT) data indicate cone tip resistance (q_c) values for the loose sand in the range of 4-6 MPa. Pre-construction boring logs revealed that the bridge's pile foundations were driven through these softer layers and embedded 2-3 m (6.5 to 10 ft) into denser sands and gravels, which exhibited cone tip resistance values between 15-20 MPa. The groundwater table was measured between 1.5 to 2 m (5 to 6.5 ft) below the surface; its depth was influenced by tidal fluctuations.

The Landing Road Bridge had 13 spans, each 18.3 m (60 ft) long, supporting a two-lane, cast-in-place concrete deck and two footpaths. Each span consisted of five precast post-tensioned concrete I-beams. The spans were bolted together and to the abutments, and the beams were bolted down to the piers. The substructure consisted of concrete slab piers spanning the entire width of the superstructure, each supported by eight 406 mm (16 in)-square pre-stressed concrete piles inclined at slope of 1H:6V.

Photogrammetry measurements indicated that the total settlement due to liquefaction and lateral spreading was around 400 mm (16 in). Total horizontal displacements, inferred from the widths of cracks observed in photographs taken in 1987, were estimated to range between 1.5-2 m (5 to 6.5 ft). Structural analyses indicated a complete collapse mechanism did not occur, as the piers remained nearly vertical post-liquefaction. However, trench investigations by Berrill et al. (2001) demonstrated most of the drag forces were exerted due to passive failure in the non-liquefied crust overlying the liquefied sand layer. The buried raked-pile foundations limited lateral spreading, and the piles, which extended through liquefiable layers into firm soil, were subjected to significant loads from lateral spread forces.

The South Brighton and Dallington Bridges, 2010-2011(M_w 6.2, 7.1) Primary Canterbury Earthquakes, New Zealand

Between September 2010 and December 2011, the City of Christchurch experienced a series of strong earthquakes with moment magnitudes ranging from 5.0 to 7.1. This section focuses on the effects of the September 4, 2010, M_w 7.1 Darfield earthquake, and the February 22, 2011, M_w 6.2 Christchurch earthquake. Both events caused severe liquefaction and spreading-induced damage to bridges. Two bridges that experienced lateral spreading in liquefied zones, the South Brighton Bridge and Dallington (Gayhurst) Bridge, are discussed.

The Darfield event occurred on a fault approximately 20-50 km (12.5 to 31 miles) west of the Central Business District (CBD) of Christchurch and generated a median PGA of about 0.20 *g* in the CBD. The Christchurch earthquake was located 4–5 km (2.5–3 miles) from the CBD and the Avon River, generated a median PGA of 0.44 *g* in the CBD, with slightly more intense shaking (up to 0.67 g) in the eastern parts of Christchurch (Bray et al. 2014).

The Darfield event caused lateral spreading of up to 30-60 cm (12 to 24 inch) at Dallington Bridge and 80-100 cm (32 to 39 inch) at South Brighton Bridge. The Christchurch event caused lateral displacements of 50-100 cm (39 inch) on the north banks and around 20 cm (8 inch) at the south bank for both bridges (Cubrinovski et al., 2014).

South Brighton Bridge:

The South Brighton Bridge is a three-span reinforced concrete (RC) bridge with a length of 65 m (213 ft), which crosses the Avon River west of New Brighton. Its superstructure has a cast-in-place RC deck supported by precast I-beams that are supported through elastomeric bearings on two octagonal hammerhead RC piers and seat-type RC abutments. The foundation of the bridge consists of 44 precast concrete piles, with 10 piles beneath each abutment and 12 piles beneath each pier. These 450-mm (18 in) diameter octagonal piles are either vertical or raked (1H:4V) and connect to the abutments or pier pile caps. The length of the abutment piles are 18.7 m (61.4 ft) and the piles beneath the piers are 13.3 m (43.6 ft) long (Cubrinovski et al., 2014).

The bridge is in a wetland with approximately 40 m (131 ft) of recently deposited soil. The 4 m (13 ft) high embankments at both approaches consist of uncontrolled fill material. At the eastern abutment, the fill includes up to 2 m (6.6 ft) of sandy silt with lenses of peat and 5–6 m (16–20 ft) of loose, uniform fine-to-medium sands. Below this unit, medium-dense sands extend to a depth of at least 25 m (82 ft). Post-liquefaction analyses indicate the upper 8 m (26 ft) of soil below the groundwater table liquefied during the Christchurch earthquake, with partial liquefaction and limited shear strains developing at greater depths. Permanent lateral ground displacements reached approximately 2.9 m (9.5 ft) at a point about 23 m (75 ft) south of the bridge's west abutment.

As seen in Figure 2-2, significant ground distortion and slumping were observed on both sides of the bridge approaches. This resulted in substantial settlement and vertical misalignment between the pile-supported bridge deck and the embankments, which rest on soft native soils. The slumping was accompanied by lateral spreading of the approaches, both towards the river and down the slopes of the embankments parallel to the river.

Due to the deck-pinning of the bridge, the abutments were back-rotated about the beam-abutment (Figure 2-2b). This occurred because the foundation piles could not resist the spreading of the foundation soil toward the river. The back rotation of the abutments forced the top of the abutment piles to displace laterally around 20 cm (7.9 inch) toward the river. Due to this large displacement, the piles were bent and resulted in tensile cracks on the river side of the piles (Figure 2-2c) and concrete-crushing on the land side of the piles (Figure 2-2d) (Cubrinovski et al., 2014).

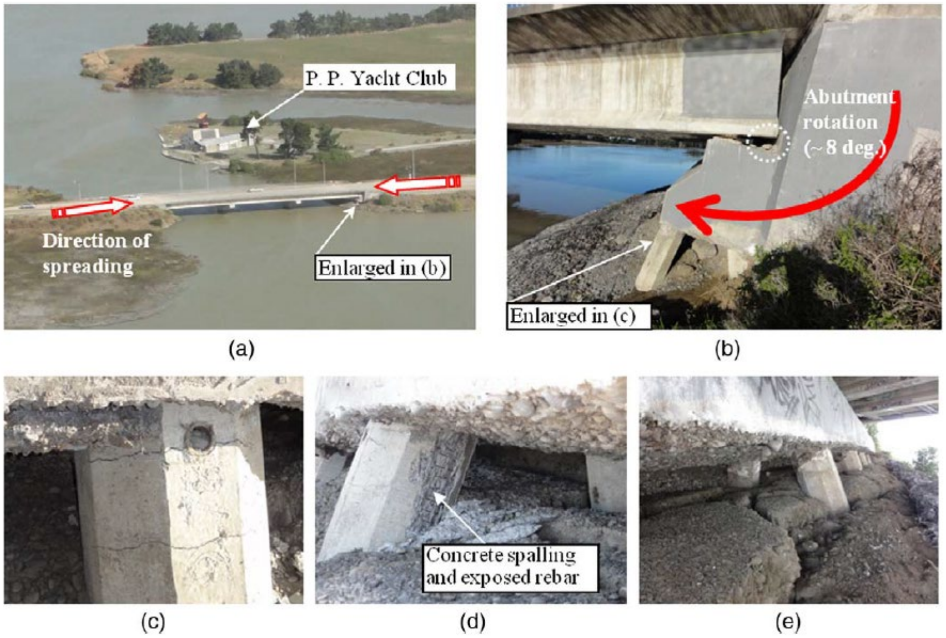

Figure 2-2 South Brighton Bridge: (a) Aerial view of the bridge toward south; (b) permanent rotation of the west abutment due to deck-pinning; (c) cracks at the top of the abutment piles due to bending; (d) concrete crushing on the land-side of abutment piles; (e) distress in the foundation due to the lateral spreading (from Cubrinovski et al. 2014).

Dallington Bridge:

The Dallington Bridge is approximately 1 km east of CBD and crosses the Avon River. This bridge is an integral structure with a continuous RC deck, RC piers, and RC abutment walls with wing walls. It has three spans without any expansion joints, with a total length of 26.8 m (88 ft). The piers and abutments are supported by square RC piles that are 350-mm (14 in) wide (D) and 10.4-m (34.1 ft) long. Beneath the piers, seven piles are spaced at 1.4 m (i.e., 4D), and six piles are spaced at 2.1 m (6D) at each abutment (Cubrinovski et al., 2014).

The bridge spans point bar deposits on the north side and cut banks on the south side. The soil profile consists of 2.5 m (8.2 ft) of brown sandy silt and silt with some peat, overlying fine sand with occasional gravelly sand extending to a depth of 15 m (49 ft), sandy silt from 15 to 20 m (49 ft to 66 ft) and fine sand from 20 to 24 m (66 ft to 79 ft). The fine sand layer between 2.5 and 9 m (8 and 30 ft) depth were identified as loose with CPT q_c of 5 MPa. The piles were extended to dense sand layers at about 13-16 m (43-53 ft) depth. On the south side, the material was significantly stronger, resulting in lower liquefaction potential and lateral displacement than observed in the north side.

Severe liquefaction and lateral spreading of about 30 to 70 cm (12 to 28 inch) was observed on the north side of the bridge. The horizontal ground movements were accompanied by vertical ground settlements of around 1 m (3.3 ft) on the north side of the bridge (Figure 2-3a). Similar failure mechanisms to those observed at the South Brighton Bridge, such as deck-pinning and back-rotation of the abutment walls, were also observed at this bridge. Figure 2-3c illustrates the large differential movements and failure of the north wing wall due to these mechanisms (Cubrinovski et al., 2014).

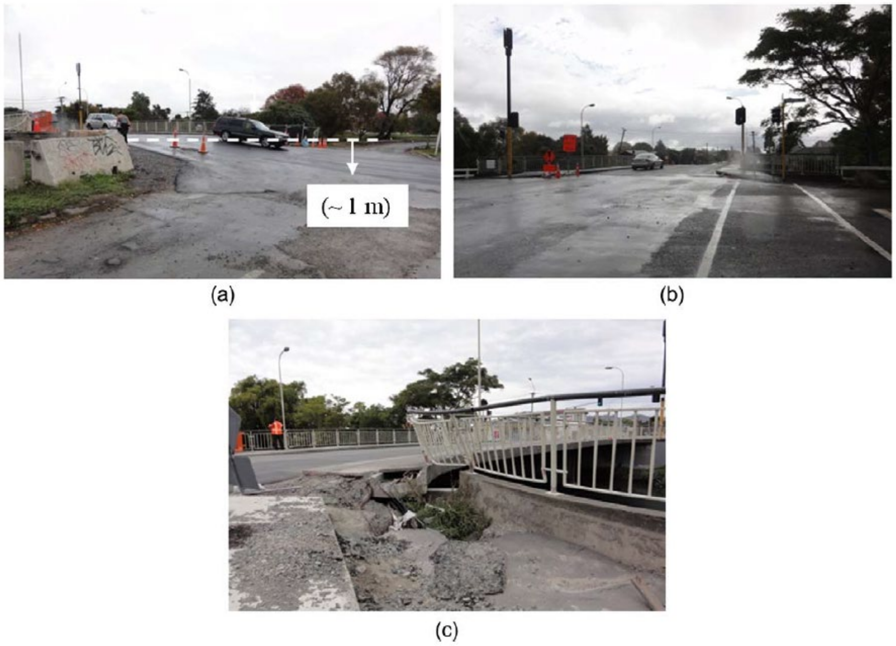

Figure 2-3 Dallington (Gayhurst) Bridge: (a) Settlement of about 1 m (3 ft) at the north approach; (b) no visible damage or distress at the south approach; (c) failure of the north wing wall due to the large differential movements (from Cubrinovski et al. 2014).

Juan Pablo II Bridge, 2010 Maule Earthquake, Chile

The offshore Mw 8.8 Maule interface earthquake occurred on February 27, 2010 on a thrust fault at the boundary between Nazca and South American tectonic plates (Yen et al., 2011). Due to the high intensity and long duration of strong shaking of this event, numerous bridges and roads suffered varying levels of damage. The Juan Pablo II Bridge was one of the several bridges that experienced liquefaction-induced damage. This section focuses on damage due to lateral spreading, while Section 2.2.2 will address settlement-induced damage observed at this bridge during the event.

The Juan Pable II Bridge is the longest vehicular bridge in Chile with the length of 2,310 m (7,579 ft). The bridge crosses the Bío-Bío River and connects the cities of Concepción and San Pedro de la Paz. The bridge has 70 spans, each 33 m (108 ft) long and 21.9 m (72 ft) wide. Each span is supported by seven reinforced concrete girders and a concrete deck, resting on reinforced concrete bents with two drilled piers (Ledezma et al., 2012).

The Bío-Bío River, originating in the Andes and flowing 380 km to the Pacific Ocean, deposits progressively finer material as it approaches the coast due to decreasing flow energy. Observations of sand boils at the Juan Pablo II bridge site, along with the SPT data, indicated that the bridge is situated on a deposit that contains layers of loose, fine sandy material. The bridge's drilled piers were shallow caisson foundations (18 m (59 ft) deep) that did not always extend to denser, non-liquefiable layers.

Although the reported maximum accelerations at nearby SMS were uncorrected and potentially influenced by structural conditions at the sites, they estimate the PGA at the Juan Pablo II site to be about 0.65 *g*. The reconnaissance team noted shear failures in columns, vertical displacements of the bridge deck reaching up to 1 m (3.3 ft), and rotation of the bridge bent of 1° to 3°. Therefore, they concluded that the liquefaction and lateral spreading at the northeast of the bridge resulted in significant damage to this bridge. These observations led to the conclusion that liquefaction and lateral spreading on the northeastern side of the bridge contributed significantly to the damage (Ledezma et al., 2012). Lateral displacement at the site was estimated to be approximately 0.3 m (1 ft) (Yen et al., 2011). Figure 2-4 illustrates tension cracks, bent rotations, and shear failures in a column on the north side of the bridge.

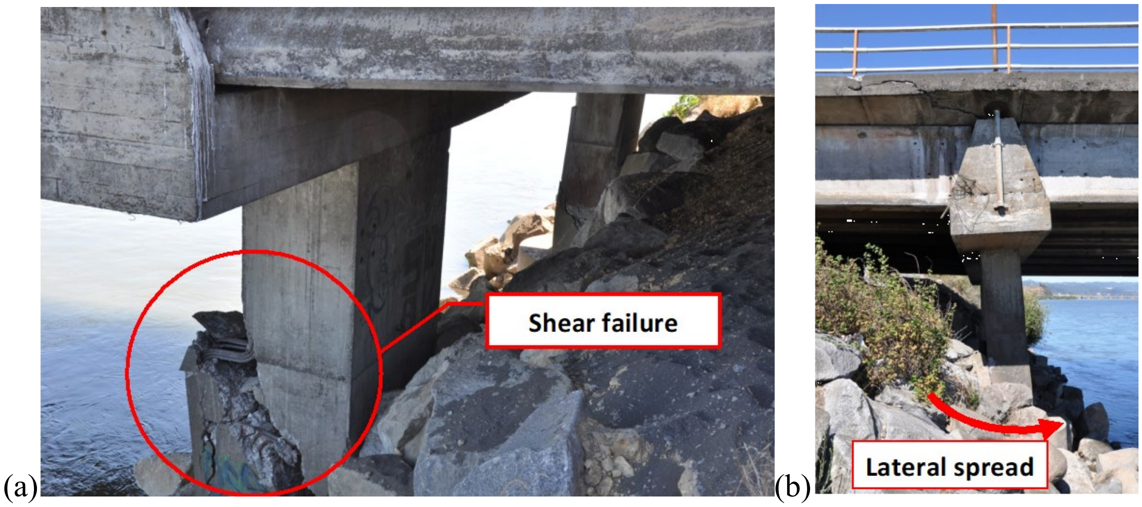

Figure 2-4 Juan Pablo II Bridge northeast side: (a) shear failure observed in the columns from the west side; (b) rotation and lateral displacement of the bent from the east side (from Ledezma et al., 2012).

2.2.2 Bridge Foundation Settlement

Juan Pablo II Bridge, 2010 M_w 8.8 Maule Earthquake, Chile

The case of liquefaction and lateral displacement affecting the Juan Pablo II Bridge during the 2010 Maule earthquake in Chile was presented in Section 2.2.1. This section further examines the case history with a focus on the bridge foundation settlement. As mentioned previously, the bridge foundation consists of drilled piers that did not always extend to denser, non-liquefiable layers, which contributed to the significant bridge settlements observed at some piers.

During the earthquake, settlement of the piers (not caused by lateral spreading which affected some piers at and near the bridge abutments) ranging from negligible to 0.6 m (2 ft) to 0.8 m (2.6 ft) at Piers #45 and #60, respectively, occurred, as illustrated in Figure 2-5. The differential settlement of the bridge in the areas of Piers #45 and #60 induced uneven movement of the deck, which caused it to rotate about its centerline and contributing to structural distress. Observations of the ground at the site indicated signs of soil ejecta, suggesting substantial pore pressure build-up and liquefaction in the surrounding soil. The areas immediately adjacent to the piers showed signs of depression, with standing water collecting in these zones, indicating a loss of lateral and vertical support for the affected drilled piers (Ledezma et al., 2012).

Figure 2-5 Juan Pablo II Bridge: Observed pier settlements (from Ledezma et al., 2012).

2.3 Field Case Histories of Buildings on Shallow Foundations on Liquefiable Sites

2.3.1 1999 M_w 7.4 Kocaeli Earthquake, Turkey

The August 17, 1999, M_w 7.4 Kocaeli earthquake occurred in western Turkey along a branch of the North Anatolian fault with a right-lateral strike-slip mechanism. The surface rupture was about 7 km (4.4 miles) from the City of Adapazarı, which suffered significant damage from the earthquake (Ansal et al., 1999). The nearby Sakarya SMS recorded an east-west horizontal component PGA of 0.41 *g*, peak ground velocity (PGV) of 81 cm/s, and peak ground displacement (PGD) of 220 cm. The north-south fault-normal component of the SMS failed to record the main event, but it likely contained a pulse-like motion due to forward-directivity and was of higher intensity (Bray et al. 2004).

Adapazari lies in a plain formed by recent fluvial activity of the meandering Sakarya and Çark rivers. Most of the soil profile consists of loose silts and silty sands in the upper 4 to 5 m (13 to 16 ft), underlain by clay deposits with some silty sand layers. The average shear wave velocity (V_{s30}) is around 150 m/sec (492 ft/sec). Most of the damage in the city was in the zones containing saturated, loose silts in the upper 5 m (16 ft) that liquefied during the earthquake. The deeper layers were dense and did not contribute much to the failures.

Most buildings in Adapazari were 3 to 6 story RC frame structures, but some of the older buildings were 2-story timber/brick structures. Due to the poor ground conditions, most of these buildings were built on shallow foundations that were very robust compared to foundation systems commonly designed for buildings of similar height. The foundations commonly consisted of 30 to 40 cm (12 to 16 in)-thick RC mats that were stiffened with 30 cm (12 in)-wide and 100 cm to 120 cm (3.2 to 3.9 ft)-deep RC concrete grade beams that were typically spaced apart 4 to 6 m (13 to 20 ft) in both directions. The open cells were filled with compacted soil and capped with a concrete floor slab. Overall, the mat foundations of the RC frame structures were about 1.5 m (4.9 ft)-thick and very stiff. Due to the high stiffness of these mat foundations, the building foundations responded as essentially rigid bodies. The initial fundamental period of the buildings was estimated to be between 0.1 to 0.4 seconds (Bray & Sancio, 2009).

Bray and Sancio (2009) categorized the observed ground failures into three different types:

- Uniform vertical displacement: Many buildings had excessive settlements without noticeable tilt. Figure 2-6 below shows an example of this case. Occasional heave was also observed on the edges of the buildings. This type of failure is the conventional bearing capacity failure, associated with the generation of excess pore pressure due to the cyclic loads of earthquake and subsequent loss of strength of the soil. Due to the heavy loads induced by the weight of the building and the earthquake-induced shear stresses, the soil is squeezed laterally, causing heave on the edges.

Figure 2-6 Examples of vertical displacement and heave observed in Adapazari after the 1999 Kocaeli earthquake (from Bray and Sancio, 2009).

- Vertical displacements with tilt: some buildings experienced non-uniform settlements with toppling. As seen in Figure 2-7, these buildings typically toppled with minimal structural damage. This was more often seen in buildings with larger height (H) to width (B) ratios. Horizontal ground shaking created an overturning moment at the foundation level or an eccentricity of the vertical load. The effect of these eccentric loads is greater for narrower foundations as the load is spread over smaller areas. When the stresses exceed the bearing capacity of the soil underneath the foundation, the buildings begin to tilt. As the tilting continues, the stresses increase as the area in which the stresses are applied to are reduced. This tilting mechanism causes eventual toppling unless the bearing capacity of the soil increases due to dilation or due to an increase of effective stress as the excess pore water pressure is dissipated.

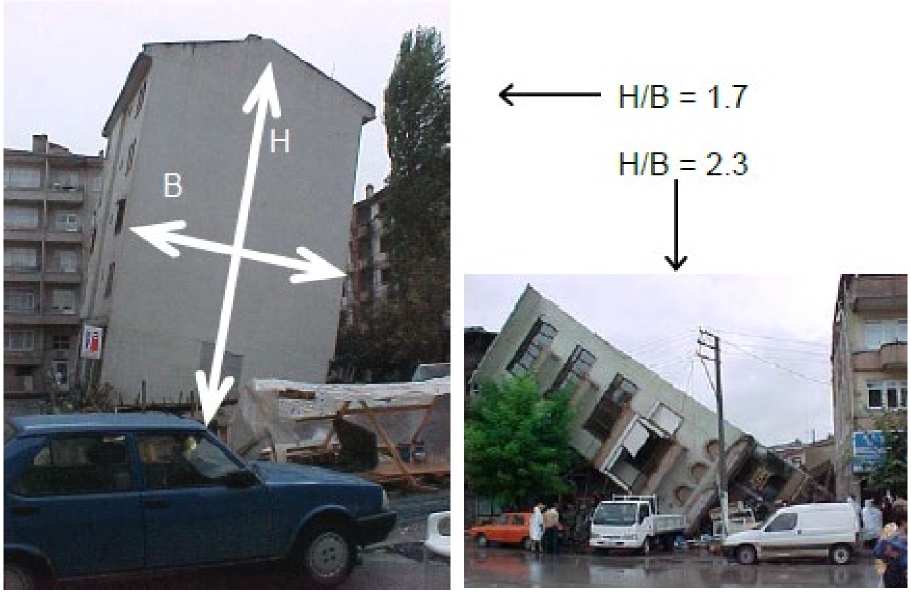

Figure 2-7 Vertical displacement with significant tilt and bearing capacity failure observed in Adapazari after the 1999 Kocaeli earthquake (from Bray and Sancio, 2009).

- Lateral translation: some buildings translated laterally over the soil directly beneath the foundation. Figure 2-8 shows an example of this case. The generation of high excessive pore pressures under and near the buildings as well as the weight of the buildings caused softening and lateral displacement of the soils underneath the foundation.

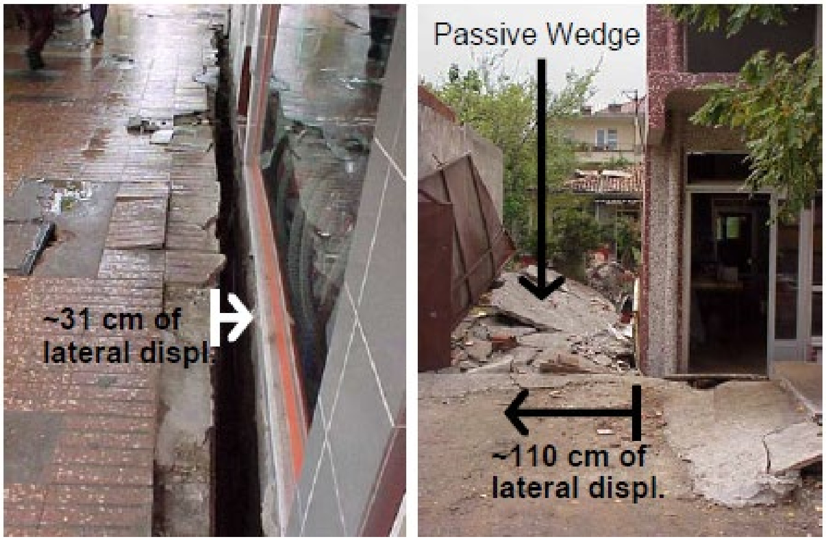

Figure 2-8 Examples of lateral displacement observed in structures on mat foundations in Adapazari after the 1999 Kocaeli earthquake (from Bray and Sancio, 2009).

2.3.2 2010 Maule M_w 8.8 Earthquake, Chile

The seismological information about the February 27, 2010, Maule earthquake was discussed in Section 2.2.1. This section focuses on the performance of buildings on shallow foundations in this earthquake. Most buildings performed well, but some modern buildings failed due to liquefaction and ground failure. This section will focus on the newly constructed hospital facility in Curanilahue, about 80 km (50 miles) southwest of Concepcion and four apartment buildings in Concepcion.

Curanilahue Hospital:

This recently constructed Curanilahue hospital facility has 10 structurally independent concrete wings with heights ranging from one to six stories, with the tallest one being the tallest building in the city. Figure 2-9 shows the schematic of the facility. The structure is composed of structural concrete pier shear walls linked via deep spandrel beams that mainly resist lateral loadings. Taller buildings (wings 1A, 1B, 1C) include shear walls in isolation along the transverse axis. Interior concrete columns are used to carry gravity loads with a slab-girder style diaphragm, which is conventional cast-in place. The foundation comprised shallow spread and strip footings with interconnecting grade-beams (Bray and Frost, 2010).

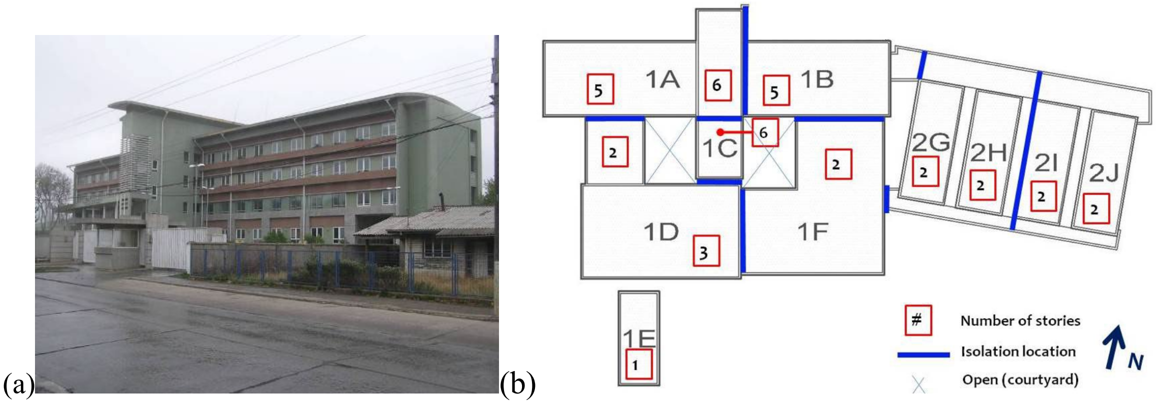

(a) (b)

Figure 2-9 (a) View of the Curanilahue Hospital looking from the southeast direction (b) hospital schematic (from Bray & Dashti, 2014).

Geotechnical investigations showed that due to the river channel running under Wings 1A to 1F, the soil from depths of 4 to 8 m (13 to 26 ft) consist of silty gravel, silty sand, and sandy silt of low to moderate plasticity. The upper soil consists of artificial fill that contains silt, debris, and coal. This is underlaid by non-plastic sandy silt, low plasticity clayey silt and silty clay with some gravel. Groundwater was found to be at an average of 0.8 m (2.6 ft).

The PGA recorded at this site during the 2010 Maule earthquake was 0.4 *g*. Downward movement, tilting, rotation and soil ejecta were observed throughout and adjacent to the buildings. Figure 2-10 shows the measurements of relative buildings movements. Wing 1C (the tallest wing) displaced downward around 11 cm (4.3 in) relative to Wing 1A, 9.5 cm (3.7 in) relative to the southwest corner of Wing 1B, and 1 cm (0.4 in) relative to Wing 1D. Wing 1C has the largest settlement than any other wings of the hospital. The northeast side of Wing 1D tilted around 1.5° towards Wing 1C and was pulled down locally with respect to Wing 1C. There was evidence of internal distortion of these structures and their foundations such as the one shown in Figure 2-11 (Bray & Frost, 2010).

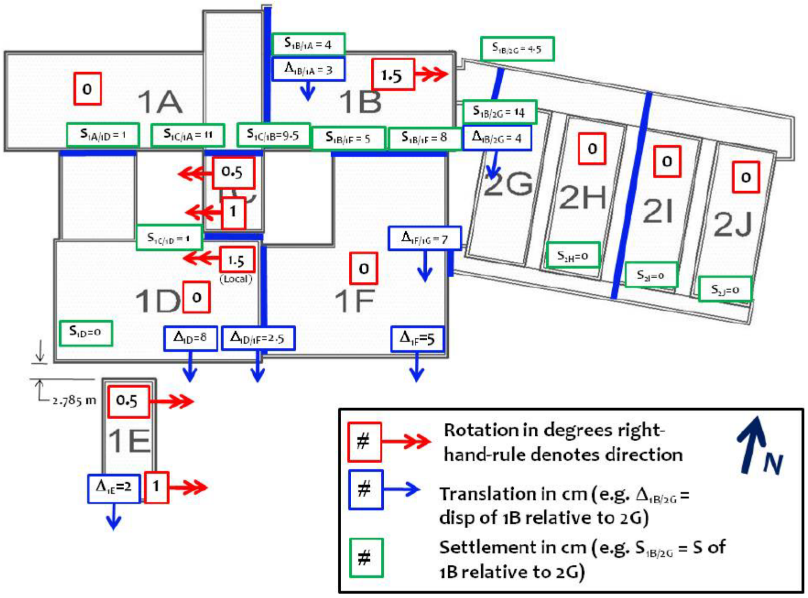

Figure 2-10 Measurements of relative building movements at Curanilahue Hospital after the Maule 2010 earthquake (from Bray et al. 2012).

Figure 2-11 Floor distortions and bulging observed at Curanilahue Hospital (from Bray & Frost, 2010).

No tilting was observed in Wings 1F and 1D. However, sediment ejecta were found along the southern sides of these wings. The northeast corner of Wing 1B extension shifted 4.5 cm (1.8 in) downward and 4 cm (1.6 in) southward relative to Wing 2G, while its southeast corner moved 14 cm (5.5 in) downward relative to Wing 2G. Wing 1B tilted by 1.5° with respect to Wing 2G, which showed no apparent tilt. Furthermore, the southeast corner of Wing 1B displaced 8 cm (3.15 in) downward relative to Wing 1F, and its northwest corner shifted 4 cm (1.6 in) downward relative to Wing 1A. Wings 2G, 2H, 2I, and 2J did not go through significant movements. However, ejecta was found adjacent to these wings and some hairline fractures were observed in its brick facing. The northern side of Wing 1E tilted 1° towards the south on the southern side and 0.5° in the northern side. There was no significant downward movement of Wing 1E.

The most pronounced structural damage was associated with the closure of the seismic gap between Wings 1D and other wings. It was concluded that damage was largely attributed to the foundation movements (Bray & Frost, 2010).

Four 8-Story Buildings (Condominio los Presidentes) in Concepcion:

The recently-built four 8-story buildings in Concepcion were also damaged by seismically induced permanent ground movement and by strong shaking. All buildings had identical floor plans and structural details. However, two of the buildings on the south end of the properties were built a year before the other two buildings going from south to north. Each building is 11.4 m by 25.6 m (37.4 ft by 84 ft) with a height of 18.7 m (61 ft). The site consisted of marshy ground before the construction, but sandy fill was placed under the buildings to raise the ground level. The groundwater during the GEER visit was at 0.5 m (1.6 ft) (Bray & Frost, 2010). The depth to the liquefiable layer was about 1.5 m (5 ft), and it consisted of well-graded silty sand with approximately 10-15% non-plastic to low plasticity fines (Bray & Dashti, 2014).

The buildings were built on spread footings with interconnected grade beams. The exterior wall footings have a design base width of 1.4 m (4.6 ft) and a stem width of 20 cm (7.9 inch). The slab-on-grade is a floating slab at the first floor living spaces. The buildings are separated by a full height elevator and stairwell approximately centered along the core of the building. Seismic load resistance in the longitudinal direction of shaking is provided by a full height structural shear wall. The transverse direction of the buildings comprises a structural shear wall for gravity and seismic load resistance (Figure 2-12) (Bray and Frost, 2010).

Figure 2-12 General components of the structural system in Riesco Building (from Bray and Frost, 2010).

The Riesco building, located on the southwest corner, suffered the most structural damage. As shown in Figure 2-13a, large sand ejecta was observed at the northeast corner of the Riesco Building. The northeast corner of this building settled about 40 cm (15.7 inch) with respect to the adjacent Bulnes Building, which did not appear to displace permanently. On the other hand, the southern end of the Riesco Building displaced only about 10 cm (3.9 inch), while the ground surrounding the building settled about 20 cm (7.9 inch). The northern end of the Riesco Building tilted approximately 1° to the east and 1° to the north due to the differential settlement in the building (Figure 2-13b). The differential movement of the foundation and the rotation of the northern half of the building overloaded the coupling beams and led to shear failure at the interface of all coupling beams and the shear walls. Shear walls in the transverse direction of the Riesco Building appeared to be undamaged. However, first floor transverse shear walls in the other three buildings exhibited a pattern of shear cracks along the longest transverse end of wall of the building (Bray, et al., 2012).

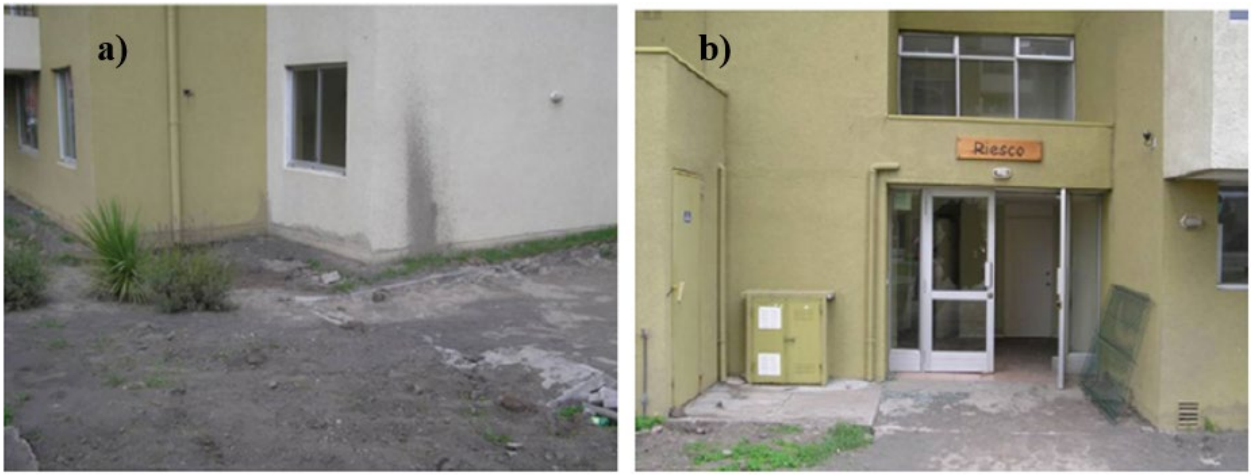

Figure 2-13 (a) Evidence of large sediment ejecta at the northeast corner of the Riesco Building; (b) Entrance to the building in the middle of its east facing side with 1˚ tilt observed in the coupling beam (from Bray & Frost, 2010).

In contrast to the Riesco Building, the Errázuriz (on the southeast) and Montt Buildings (on the northeast) settled uniformly about 10 cm (3.9 inch) while the surrounding ground settled about 20 cm (7.9 in). As mentioned, the Bulnes Building on the northwest side of the site did not undergo seismically induced permanent settlement. The ground in the open space between the buildings settled a non-uniform amount ranging from 0 around the Bulnes Building to around 10 to 20 cm (3.9 to 7.9 in) in the areas closer to other buildings (e.g., Figure 2-14) (Bray & Frost, 2010). The street that surrounded the property did not appear to settle and there was no evidence of ground failure in the adject one to two-story properties that were built by different contractors within the same timeframe as the condominiums (Bray et al. 2012).

Figure 2-14 Ground settlement between the Riesco and Bulnes Buildings (from Bray & Frost, 2010).

2.3.3 2011 M_w 6.2 Christchurch Earthquake, New Zealand

The seismological details of the 2010-2011 earthquake series in New Zealand are described in Section 2.2.1. This section highlights how buildings on shallow foundations behaved during the earthquake. Significant liquefaction-induced ground settlement and building damage was observed in the CBD during the 2011 M_w 6.2 Christchurch earthquake. This was due to the closer proximity to the causative faults, shallower groundwater table, and presence of liquefiable layers (Bray et al., 2017). Two of these cases are discussed in this section.

CTUC Building:

The CTUC building was a 21 m (69 ft)-high six-story RC frame structure with RC core walls and block in-fill walls with a steel framed roof. The width of the structure was 20 m (66 ft) in the east-west direction and 25 m (82 ft) in the NS direction (Luque & Bray, 2017). The structure was supported on 2.44 m (8 ft) square footings with embedment depths of 0.46 or 0.6 m (1.5 to 2 ft) that were connected to each other with weak tie beams. The footings supported square RC columns with the width of 0.5 m (1.6 ft) (Bray et al., 2017). Footing pressures including the dead load and 20% of the live load were estimated to be 190-250 kPa (3968 to 5221 psf) (Luque & Bray, 2017) .

The structure was situated on top of shallow fill layer, underlain by a silty sand/sandy silt (SM/ML) layer that extended to 2.5 m (8.2 ft) depth across the site except for the southern side where the layer extended to 5 m (16.4 ft). The CPT corrected cone tip resistance (q_t) of this layer is less than 5 MPa (0.73 ksi) with an estimated relative density of 35-45%. The groundwater was estimated to be 2.5 m (8.2 ft) deep. Therefore, the loose silty sand layer underneath the groundwater was highly susceptible to liquefaction. A dense gravelly sand with q_t of 20-30 MPa (3 to 4 ksi) and relative density of 80-90% underlies the loose silty layer and extends to the depth of 7.5-9 m (25-30 ft). This layer is underlain by a medium dense sand and silty sand with q_t values of 10-20 MPa (1.5-3 ksi) and relative densities of 60-70% that extend to depths of 16 to 17 m (53-56 ft). A dense sand layer and an over-consolidated clay unit underly the dense sand layer. The dense Riccarton Gravel unit underlies the clay unit. The dramatic change in the shallow soil condition between the northern and the southern side of the building led to significant differential settlement of an average of 250 mm (9.8 in) that produced structural deformation and cracking (Figure 2-15) (Bray et al., 2014).

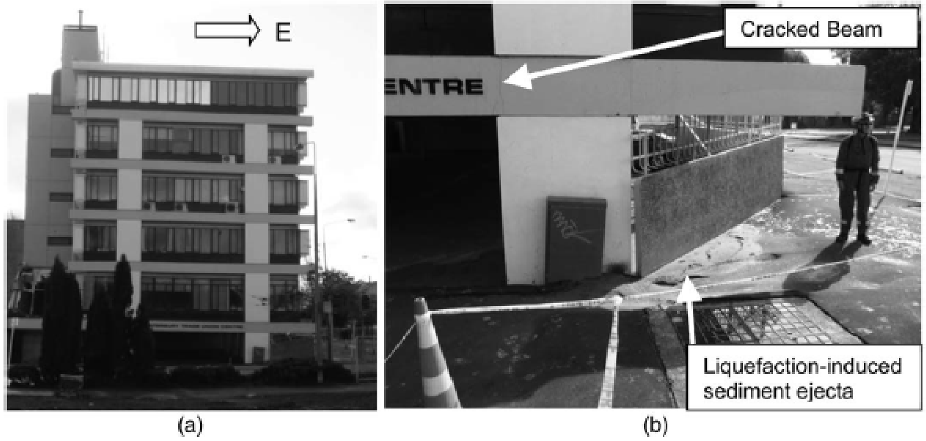

Figure 2-15 (a) South end of the CTUC Building tilting to the east; (b) Ejecta observed at the southeast corner of the building (from Bray et al., 2014).

As seen in Figure 2-15b, the southeast column settled significantly more than other columns. The differential settlement led to angular distortion of 1/50 in the south side. A large amount of ejecta was observed in the southeast corner of the building. The settlement induced by this ejecta was measured to be between 70-150 mm (2.8-5.9 in). Differential punching settlement was measured to be around 60 mm (2.4 in) in the northeast and 310 mm (12.2 in) in the southeast corners. Total liquefaction-induced settlements of approximately 160-300 mm (6.3 to 11.8 in) and 320-600 mm (12.6-23.6 in) were estimated in the northeast and southeast sides, respectively (Bray et al., 2014).

Nonlinear dynamic studies by Luque & Bray (2017) concluded that bearing capacity failure at the southeast corner of the building and loss of soil under the footing due to ejecta formation were the primary mechanisms that caused the damage of the CTUC structure. Because the columns on the southeast corner of the building were situated on top of the loose silty sand/sandy silt layers, large strain values of up to 8% were observed. However, on the northeast corner, since the loose silty sand/sandy silt was not present below the groundwater, large shear strains did not develop. Therefore, these differing responses of the soils led to differential settlements observed between the northeast and southeast corners of the building.

FTG-7 Building:

FTG-7 building was a 23.9 m (78.4 ft) high, seven-floor steel frame structure. The width of the structure was 29.1 m (95.5 ft) in the east-west direction and 31.8 m (104 ft) in the north-south direction. Its foundation consisted of shallow RC strip footings with widths of 2 to 3.3 m (6.6 to 10.8 ft) and depth of 0.6 m (1.97 ft). The footings were interconnected with square-shaped RC tie beams. The base of the perimeter strip footings was 1.2 m deep (3.9 ft), and the base of the interior footings were 0.7 m (2.3) (Bray et al., 2014). The pressure on the footing was estimated to be 80-100 kPa (1670-2088 psf), which includes the dead load and 20% of the live load.

The soil profile consists of a shallow (1-1.5 m (3.3-4.9 ft) fill layer, underlain by sandy silt/silty sand up to a depth of 7-8.5 m (23 to 28 ft). The “equivalent clean sand” relative density for this layer was estimated to be around 35-55%. Below this layer, a medium dense sand with relative density between 60-70% is found that extends to the depth of 14-16.5 m (46 to 54 ft). A very dense sand layer (Dr ≈ 90%), a 1-2 m (3.3 to 6.6 ft) thick clayey silt (ML/MH) with some peat and the Riccarton Gravel unit underlie the medium dense sand layer. The groundwater was at around a depth of 2 m (6.6 ft) during the earthquake (Bray et al., 2014).

Surveys indicated that the building tilted towards the southeast. A downward displacement of 100 mm (3.9 inch) of the southeast corner relative to northwest was measured. The total building settlement of around 400 mm (15.7 inch) was estimated after the Christchurch earthquake. Due to the wider foundation of this building, however, the total amount of settlement and differential settlement was less than surrounding buildings with similar conditions. Therefore, although the building was taller, it suffered less damage than other nearby buildings (Bray et al., 2014).

Numerical studies by Luque and Bray (2017) showed that the primary mechanism for building settlement in this case was due to SSI ratcheting. This mechanism was seen in the calculated vertical displacement time histories. The rocking of the building induced high seismic demands in the soils beneath the edge of the building. This led to lateral displacement of the soils beneath the edges of the building towards the free field, which caused downward vertical movement of the building. The study also mentions that shear-induced partial bearing capacity and volumetric-induced mechanisms also contributed to the building settlement.

2.3.4 2011 M_w 9.0 Tohoku Earthquake, Japan

The March 22, 2011, M_w 9.0 Tohoku earthquake occurred at 2:46 PM off the coast of the Tohoku in Japan. The tsunami generated by the earthquake caused severe damage to the built environment. In addition, liquefaction-induced ground failures were observed in many areas. This section examines a specific case that highlights how pile foundations, shallow foundations, and the free field respond differently to liquefaction.

Figure 2-16 below illustrates the responses of a pile-supported building and a building with a shallow foundation relative to the free field in the city of Urayasu. The PGA recorded in Urayasu varied from 0.2g to 0.3g, depending on the thickness of the loose sandy fill present throughout the city (Tokimatsu et al., 2011). Adjacent to the pile-supported building shown on the left side of Figure 2-16, the ground settled approximately 40 cm (15.7 in). This level of free-field settlement was pervasive in this part of Urayasu (Bray & Dashti, 2014).

In contrast, the three-story building on the right side of Figure 2-16, which was supported by a shallow foundation, punched into the ground, displacing 30 cm (11.8 in) into the surrounding soil and moving a total of 70 cm (27.6 in) relative to the pile-supported building. Consequently, the liquefaction-induced settlement included 40 cm (15.7 in) of displacement in the free field and an additional 30 cm (11.8 in) for the shallow foundation, whereas the pile foundation prevented any significant downward movement.

These observations demonstrate that 1-D volumetric reconsolidation liquefaction-induced settlement accounts for only part of the expected settlements for shallow foundations, often underestimating the total settlement. Shear-induced mechanisms should also be considered for structures with shallow foundations (Bray & Dashti, 2014).

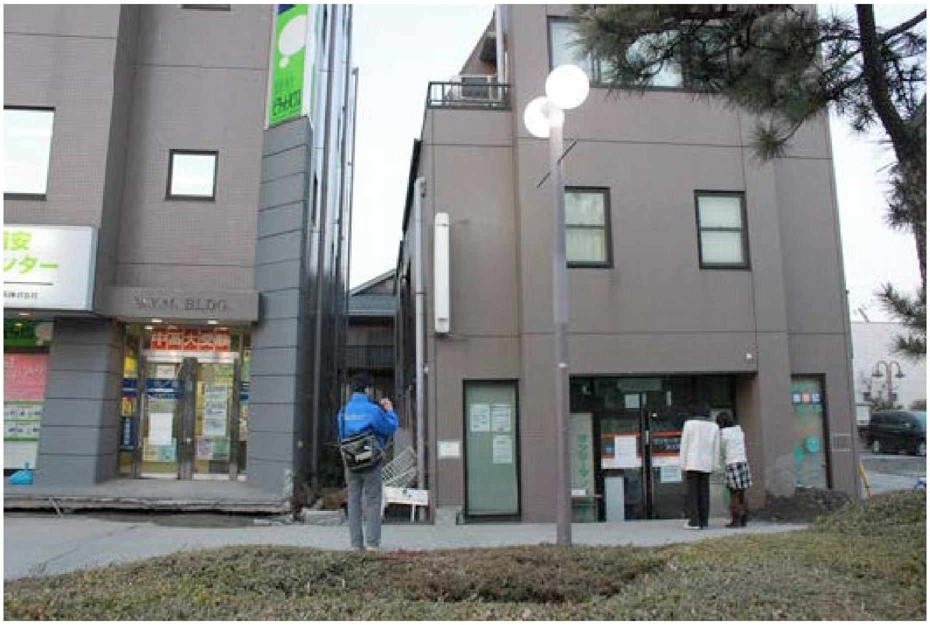

Figure 2-16 Differing responses of a pile-supported building (building on the left), and a building on shallow foundation (on the right) relative to the free-field ground (from Tokimatsu et al., 2013).

2.3.5 2023 M_w 7.8 Kahramanmaraş Turkey Earthquake

On February 6, 2023, Turkey experienced two major left-lateral earthquakes, followed by numerous aftershocks, along the East Anatolian Fault Zone (EAFZ). The first event had a M_w of 7.8 and occurred along a northeast-southwest alignment of the fault at a focal depth of 8.6 km. The second event, with a M_w of 7.5, struck nine hours later along a west-northeast alignment of the fault at a focal depth of 7.0 km. Both earthquakes caused extensive damage, including liquefaction-induced impacts on buildings and other infrastructure (Cetin et al. 2023). This section highlights key observations from the port city of Iskenderun.

Post-earthquake reconnaissance identified that most liquefaction-induced damage occurred within reclaimed areas along Iskenderun's current shoreline, primarily as a result of the M_w 7.8 mainshock event. Moug et al. (2024) grouped the affected sites into five zones, which are shown as Areas 1 through 5 in Figure 2-17. The PGA experienced across these areas ranged from approximately 0.32 to 0.33 g. At the time of the earthquake, the estimated depth to the water table across all areas was approximately 1.5 m (4.9 ft) (Arnold et al., 2025).

Figure 2- 17 Overview of liquefaction observations and study areas within Iskenderun (from Moug et al., 2024).

Structures in these areas were evaluated based on observed settlements, using the following parameters: one-dimensional (1D) free-field post-liquefaction volumetric-induced reconsolidation settlement (S_v), the lateral spreading displacement index (LDI), the liquefaction severity number (LSN), the liquefaction demand parameter (L_D) for estimating ejecta-induced settlement, and the liquefaction building index (LBS).

Observations from each area revealed distinct patterns of damage and settlement influenced by variations in subsurface conditions and structural factors. Moug et al. (2024) documented unique ground deformation patterns induced by building settlements in these areas. In some cases, the building settlement induced settlement of the adjacent ground over several meters from the building perimeter. This type of settlement decreased with increasing distance from the buildings and resulted in convex ground surfaces near the buildings, described as hogging. A schematic representation of this type of deformation is shown in Figure 2-18.

The hogging deformation was observed in buildings with significant settlements. However, this type of deformation differs from the hogging associated with differential settlement, where the exterior of a foundation settles more than the center. Most of the structures in Iskenderun had stiff foundations that appeared to settle uniformly, without significant internal distortion. Moug et al. (2024) noted that free-field observations did not indicate evidence of ground settlement or heave that could provide an alternative explanation for this behavior. Additionally, some cases exhibited punching settlement, where the localized settlement of foundations penetrated into the underlying soil. However, in general, the extent of punching settlement was notably less than the settlement associated with ground hogging (Moug, et al., 2024).

In contrast to hogging, sagging around the ground deformation (concave ground curvature) was also observed in some instances, where larger settlement occurred beneath the middle of the building relative to its corners (Moug, et al., 2024). These varying deformation patterns were analyzed in detail for each area, as described below.

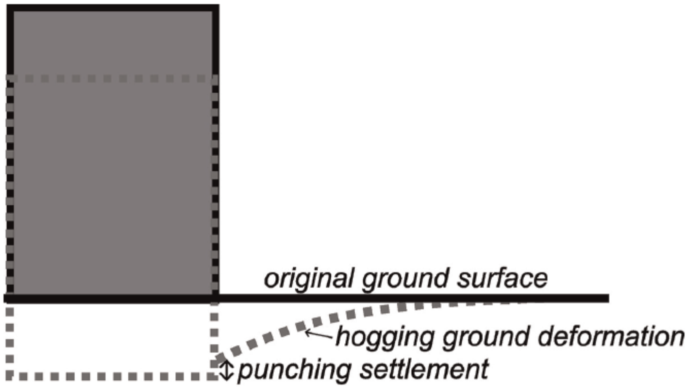

Figure 2-18 A schematic of building-ground interaction with contributions from punching and building-induced ground hogging (from Moug et al., 2024).

AREA 1:

Area 1 is located within the reclaimed shoreline in the Cay District of northeast Iskenderun. This area includes four buildings: Buildings G, H, I, and J (Figure 2-19). These four 6-story buildings are constructed with reinforced concrete frames with infill walls (RCF-IW) and include 2.5 m (8.2 ft) deep basements. Buildings G and J have a 90-cm (35 inch) thick RC mat foundation overlain with 1-m (3.3 ft) deep intersecting beams that form a grid. In contrast, Buildings I and H have 30-cm (11.8 inch) slabs without cross-beams (Moug et al., 2024).

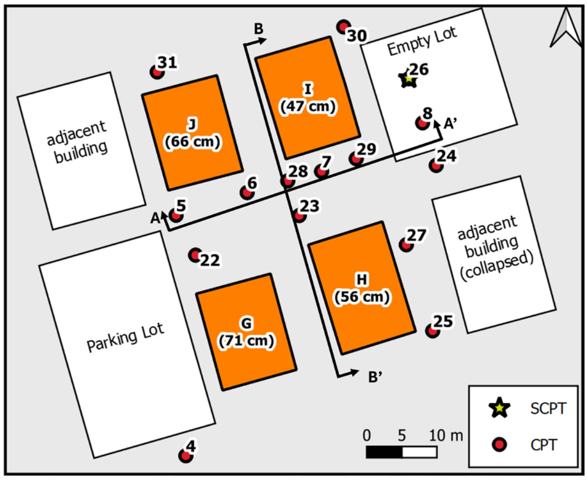

Figure 2-19 Overview of Area 1, note that the numbers inside the buildings show the settlements measured by Moug et al. (2024).

Geotechnical investigations revealed that the subsurface profile in this area consists of very dense fill material (debris and cobbles) in the upper 3 to 4.5 m (9.8 to 14.7 ft), underlain by a predominantly sandy layer extending to a depth of about 10 m (32.8 ft). This sand layer has a cone penetration test (CPT) Q_{tn} ranging from 75 to 120 and an average I_c of 1.8. Below the sand unit lies an interbedded sandy silt and silty clay layer with lower Q_{tn} values less than 35 and fluctuating I_c values between 2.4 and 2.9, transitioning into a clay unit below 14.5 m (47.5 ft). Shear wave velocity (V_s) increases from 200 m/sec (656 ft/sec) to 250 m/sec (820 ft/sec) over the depth of the sounding. The CPT profile indicates that the subsurface conditions are uniform across the area, with no significant variation in the thickness of the liquefiable layer. Liquefaction assessments determined that the upper sand unit from 3 to 10 m (9.8 to 32.8 ft) is liquefiable, along with thinner zones of liquefiable material in the looser layer from 10 to 15 m (32.8 ft to 49.2 ft) (Arnold et al., 2025).

The observed building settlements in Area 1 range from 47 to 71 cm (18.5 to 28 in). Most of this settlement is attributed to the ejecta- and shear-induced components of liquefaction-induced settlement (Arnold et al., 2025). Figure 2-19 depicts the total settlement of each building in this area. The 1D post-liquefaction volumetric strain (S_v) of the surrounding ground, as well as beneath the buildings, ranges from 16 to 25 cm (6.3 to 9.8 in). The liquefaction severity number (LSN), which reflects the ejecta component, ranged from 25 to 33, while the liquefaction building index (LBS), representing the shear component, ranged from 23 to 35. The liquefaction demand parameter (L_D) values ranged between 40 and 80, indicating severe ejecta effects with estimated localized free-field ejecta-induced settlements of 3 to 20 cm (Arnold et al., 2025).

Hogging ground deformation was observed in the courtyard between buildings J and G, as well as buildings I and J (Figure 2-20). Settlement measurements showed that the least ground settlement occurred in the middle of the courtyard, with settlement increasing toward the buildings. As illustrated in Figure 2-20, the convex warped ground is visible from the displaced tiles and the pooling of floodwater around the bases of the buildings.

Figure 2-20 Hogging in the courtyard of four buildings in Area 1: (a) facing west with Building G on the left and Building J on the right; (b) facing east with Building I on the left and Building H on the right (from Moug et al., 2024).

Lidar measurements suggest that free-field conditions did not exist between the buildings. The hogging pattern is likely due to overlapping zones of influence between adjacent buildings, where the settlements of one building impacted the settlement patterns of nearby structures. The close proximity of these buildings amplified this interaction (Moug et al., 2024). Figure 2-21 provides a schematic representation of the interpreted building-ground interactions.

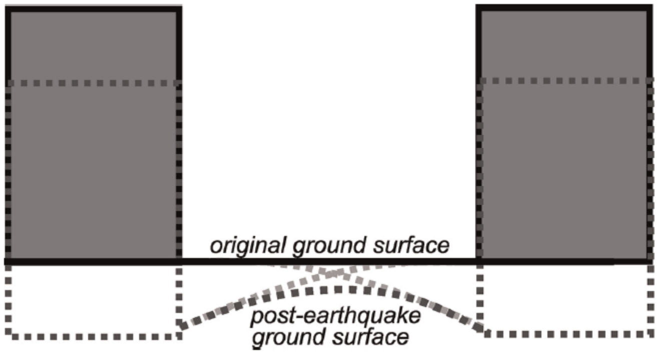

Figure 2-21 A schematic of interpreted building-ground interaction at the group of four buildings in Area 1 (from Moug et al., 2024).

AREA 2:

Area 2 contains three buildings located approximately 75 m (29.5 ft) west of Area 1: Buildings M, L, and K (Figure 2-22). Buildings K and M are constructed with reinforced concrete frames and infill walls (RCF-IW), while Building L is a one-story steel-frame structure on a concrete slab foundation. Buildings K and M have similar construction styles to the structures in Area 1, featuring salon-type first floors.

Building M is a 5-story structure with a partial 6th floor and a 2.5 m (8.2 ft) deep basement resting on a 30-cm (11.8 in) thick slab. Building K is also a 5-story structure but has a 2-m (6.6 ft) deep partial basement that does not extend across the full building footprint (Arnold et al., 2025). Building L, which is 10.7 m (35.1 ft) wide, is located directly adjacent to Building M, while Building K is approximately 2.7 m (8.9 ft) away from Building L (Moug et al., 2024).

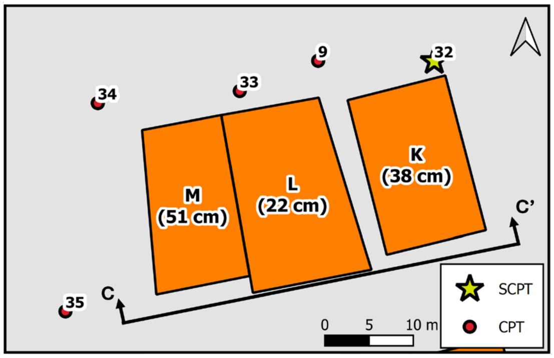

Figure 2- 22 Overview of Area 2. Note that total settlement of each building is written inside the building (from Arnold et al. 2025).

Geotechnical investigations in Area 2 revealed a subsurface profile similar to Area 1. The profile consists of a 3 m (9.8 ft) thick layer of very dense fill material, underlain by a sand unit with comparable CPT parameters to Area 1: Q_{tn} values between 75 and 120, and an I_c value of 1.8. Below the sand unit lies interbedded sandy silt and silty clay, which contains fewer liquefiable layers than Area 1 but exhibits similar CPT indices. The V_s in this area fluctuates between 180 (591 ft/sec) and 220 m/sec (722 ft/sec) over the depth of the sounding. Subsurface conditions across all buildings in Area 2 were determined to be uniform (Arnold et al., 2025).

Liquefaction-induced settlement parameters for Area 2 showed S_v values ranging from 15 to 22 cm (5.9 to 8.7 in), and L_D values ranging from 23 to 31, 27 to 30, and 55 to 110 for Buildings L, K, and M, respectively. These values are consistent with those observed in Area 1 but are slightly reduced, except for L_D values, which indicate Severe-to-Extreme ejecta effects. Localized free-field ejecta-induced settlements were estimated to be between 3 and 20 cm (1.2 to 7.9 in). Observed building settlements in Area 2 ranged from 22 to 51 cm (8.7 to 20.1 inch), which is slightly lower than those in Area 1. This reduction may be attributed to the interbedded sandy silt and silty clay layers, which exhibit a finer-grained response compared to Area 1 (Arnold et al., 2025).

The large settlements observed at Buildings K and M appeared to induce hogging ground deformation beneath the lighter-weight Building L. Figure 2-23 shows that damage to Building L includes extension cracks in the façade and the concrete floor slab. The hogging pattern in Area 2 is similar to that observed in Area 1, suggesting that the presence of a lightweight structure (Building L) between two heavier structures (Buildings K and M) had minimal effect on the overall ground deformation (Moug et al., 2024).

(a) (b) (c)

Figure 2-23 (a) Buildings K, L and M in Area 2 with Building L in the middle; (b) damage to the exterior at Building L due to the hogging deformation; (c) damage to the concrete slab at Building L due to the hogging deformation (from Moug et al., 2024).

AREA 3:

Area 3 is located approximately 1 km (0.6 mile) west of Areas 1 and 2, on the historical shoreline. This area contains three structures: two 6-story RCF-IW buildings, Buildings V and T, and a 2-story middle structure, Building U. While plans for these structures were unavailable, they are assumed to have similar construction to the buildings in Areas 1 and 2. Building V includes a basement, whereas Building T does not (Arnold et al., 2025).

Building T measures 16.8 m (55.1 ft) in width, 22.5 m (73.8 ft) in length, and 18.7 m (61.4 ft) in height, while Building V is more prominent, measuring 36.4 m (119.4 ft) in width, 25.3 m (83 ft) in length, and 21.8 m (71.5 ft) in height (Moug et al., 2024). Figure 2-24 provides a schematic representation of Area 3 and observed building settlements.

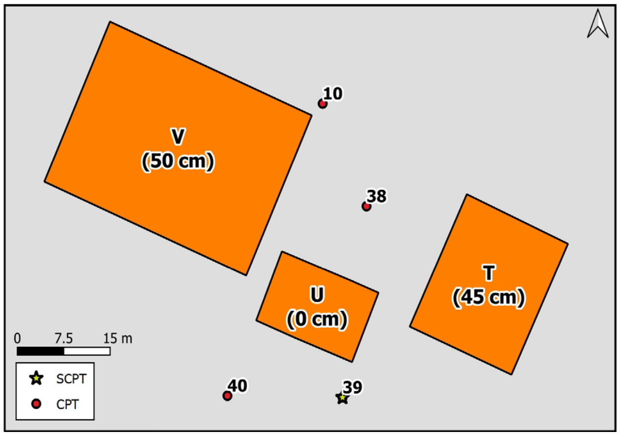

Figure 2- 24 Overview of Area 3 with settlement of each structure (from Arnold et al., 2025).

Geotechnical investigations revealed differences in subsurface conditions compared to Areas 1 and 2 (Arnold et al. 2025). The first 3 m (9.8 ft) on the north side of the buildings comprises a very dense gravelly fill layer, similar to Areas 1 and 2, but this layer thins to 1.5 m (4.9 ft) toward the south. Beneath the fill lies a dense sand unit with Q_{tn} values between 100 and 300 and I_c values ranging from 1.3 to 2. This sand layer extends to 3 m (9.8 ft) and gradually becomes less dense, with Q_{tn} values decreasing to less than 100 and I_c values of approximately 2, continuing to loosen to Q_{tn} values around 50 at a depth of 15 m (49 ft).

Below the sand layer lies a silty sand to clayey silt layer extending to 18 m (59 ft), with Q_{tn} values under 10 and I_c values of about 2.9. Deeper clay material exists below 18 m (59 ft), with Q_{tn} values under 5 and I_c of 3.2. This profile differs from Areas 1 and 2, which had more notable interbedded soil layers. Additionally, CPT results showed greater thickness in liquefiable layers for Area 3 compared to the other areas. V_s values ranged from 150 to 200 m/sec (492-656 ft/sec) in the upper 15 m (49 ft), increasing to 200–250 m/sec (656-820 ft/sec) at 30 m (98 ft) depth (Arnold et al., 2025).

Buildings V and T exhibited settlements comparable to those in Areas 1 and 2. In contrast, Building U showed no discernible settlement. The estimated S_v values for Area 3 ranged from 24 to 32 cm (9.4-12.6 in), higher than those in other areas. Liquefaction severity number (LSN) and liquefaction building index (LBS) values were also elevated, ranging from 32 to 38 and 37 to 44, respectively. Liquefaction demand (L_D) values ranged from 25 to 65, indicating severe ejecta effects, with localized free-field ejecta-induced settlements estimated at 3–20 cm (1.2-7.9 in).

The greater thickness of the liquefiable layer in Area 3 contributed to the increased S_v, LBS, and LSN indices. However, the larger area of the mat foundations of Buildings V and T potentially reduced shear-induced settlement. This interplay between settlement types resulted in total settlements for Area 3 being similar to Areas 1 and 2 despite the different subsurface conditions and foundation designs. Additionally, the reduced spacing between buildings in Area 3 likely amplified settlement interactions (Arnold et al., 2025)

Buildings T and V appeared to drag down the surrounding ground, creating a diminishing settlement gradient extending outward from their edges (Figure 2-25). This ground deformation mirrored a hogging pattern, with a convex central horizontal segment approximately 9 m (30 ft) long where no settlement was observed. This segment, considered free-field, aligns with the lack of settlement at Building U. The hogging zones of influence for Buildings T and V extended approximately 9.9 m (32.5 ft) each (Moug et al., 2024).

(a) (b) (c)

Figure 2-25 (a) Building T, where the liquefaction-induced settlement caused hogging; (b) Building U, unaffected by liquefaction; (c) Building V with liquefaction-induced hogging (from Moug et al., 2024).

The hogging pattern in Area 3 is comparable to the mid-rise buildings with smaller settlements, such as Building I in Area 1 and Building K in Area 2. However, the 9.9 m (32.5 ft) zone of influence in Area 3 is significantly larger than that observed for Building K (6.7 m (22 ft)) and Building I (6.2 m (20.3 ft)). This increased zone of influence may stem from differences in subsurface conditions, structural systems, and building weights in Area 3. Alternatively, the larger spacing between buildings in Area 3 could have limited building-ground-building interactions, as observed in the absence of settlement at Building U (Moug et al., 2024).

AREA 4 & 5:

Area 4 is directly south of the buildings in Area 3 and lies within the historical shoreline. Building W in Area 4 is a 5-story structure with no basement, resting on a 95-cm (37 in) thick slab. There is an empty lot on the northwest side of Building W, with an adjacent building on the southwest. Notably, Building W experienced lower settlement compared to similarly sized buildings in Areas 1, 2, and 3.

Area 5 consists of five buildings: S, R, Q, P, O, and N, located between Areas 2 and 3. Buildings S, Q, and N are 7-story structures, while Buildings O and R are smaller, with 6 and 5 floors, respectively. Building P is a historic 2-story structure. Figure 2-26 provides a schematic representation of Areas 4 and 5 (Arnold et al., 2025).

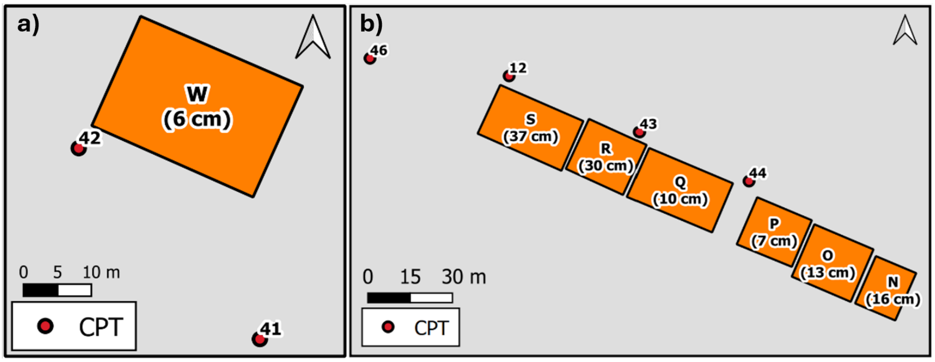

Figure 2-26 Overview of (a) Area 4 and (b) Area 5 with observed building settlements (from Arnold et al., 2025).

The CPT data for Areas 4 and 5 shows 1.5 to 3 m (4.9-9.8 ft) of dense gravelly fill layers, similar to those in Areas 1 and 2. However, the CPT responses for Areas 4 and 5 are more consistent with those from Area 3, albeit with slightly reduced thickness in the liquefied sandy layer. The liquefiable sandy layer in Areas 4 and 5 extends to 14 m (46 ft), compared to 15.5 m (51 ft) in Area 3 (Arnold et al., 2025).

The overall ranges of settlement indices in Area 4 are relatively consistent with those in other areas. However, the L_D value in Area 4 is slightly lower due to the reduced thickness of the liquefiable layer, indicating moderate-to-severe ejecta potential. The ranges of settlement indices in Area 5 are similar to those in Area 3 but are slightly larger than in Areas 1 and 2. The buildings in Area 5 experienced a wider range of settlements (between 7 to 37 cm (2.8-14.6 in)) compared to other areas, attributed to various factors, including design differences (Arnold et al., 2025).

Sagging deformation was observed in Building W in Area 4 and in Buildings S, R, and Q in Area 5. As shown in Figure 2-27, Building W exhibited sagging, with the middle of the building settling about 10 mm (0.39 inch) more than the corners. Moug et al. (2024) noted that the sagging in these structures is due to their flexible foundations. This observation aligns with findings from other case histories (e.g., Bray & Sancio, 2009; Bray et al., 2014).

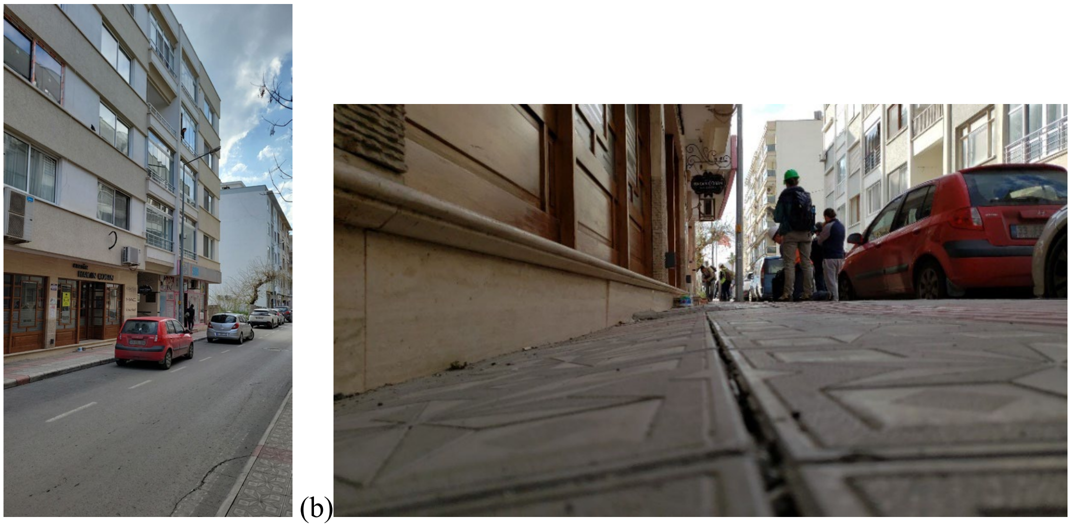
(a) (b)

Figure 2-27 (a) Street view of Building W in Area 4; (b) Ground and building settlement near the entrance of Building W (from Moug et al., 2024).

2.4 Key Insights

Based on the field case histories reviewed in this study, the most significant findings related to liquefaction mechanisms affecting bridges on pile foundations and buildings on shallow foundations are:

- Lateral spreading is a key factor in the seismic performance of bridges sited on liquefiable soils. Field case histories indicate that under-designed pile foundations often fail to support a bridge superstructure during significant liquefaction-induced lateral spreading fully. Significant lateral spread loads can be imposed on the piles that extend down from the liquefiable soil layer into firm soils below it and up into a competent crust that holds the pile tops within it as it translates horizontally. This mechanism can damage the pile due to bending and shear deformation and rotate pile-supported bridge abutments.

- The liquefaction-induced lateral spread hazard should be evaluated and if present, mitigated through ground improvement or resisted or accommodated through a robust pile design. It is unlikely that cost-effective design of shallow bridge foundations without comprehensive ground improvement that mitigates the lateral spread hazard can be developed. Thus, shallow-founded bridges should be avoided at sites with an unmitigated lateral spread hazard.

- The inertial forces and contact pressure of structures contribute significantly to observed liquefaction-induced ground failure. For instance, in Adapazari, ground failure was predominantly concentrated near buildings, while areas away from buildings experienced less ground failure.

- The ratio of a structure's height (H) to its width (B) plays a critical role in the severity of liquefaction-induced damage of structures with shallow foundations. Field case histories from Adapazarı and Christchurch reveal that taller buildings with narrower foundations (i.e., higher H/B ratios) experienced more significant damage, including increased differential settlement and tilting. Lower H/B ratios, in contrast, generally reduce these effects.

- Strong, stiff shallow building foundations that accommodate ground settlement through uniform settlement or rigid-body tilt without internal distortion of the overlying structure reduce structural damage due to liquefaction-induced ground movements. However, excessive rigid-body tilt can induce a toppling failure that should be avoided.

- Bridge systems can be adversely affected by excessive rigid body tilt of its piers that are supported on shallow foundations. Likely, the substantial amount of tilt observed in several of the building case histories exceeds the design limits for most bridge systems.

- The distance between adjacent buildings can significantly influence settlement patterns and ground deformation. Observations from Areas 3 and 1 in Iskenderun during the 2023 Kahramanmaraş earthquake showed that closer building proximity in Area 3 resulted in more pronounced hogging and larger settlements, despite similar subsurface conditions. This suggests that spacing between shallow foundations, such as those used for bridge piers, may play a critical role in mitigating ground deformation. While the load carried by a bridge pier's shallow foundation might differ from that of a small building, the potential for settlement-related issues such as hogging or differential settlement still warrants careful consideration of footing spacing to ensure the stability and performance of bridges.

- Flexible shallow foundations can lead to building-ground deformations such as sagging as observed in 2023 Turkey earthquake.

Chapter 3 EXPERIMENTAL STUDIES

3.1 Introduction

Experimental studies have evaluated the performance of shallow building foundations on liquefiable ground. Centrifuge tests often validate hypotheses derived from field case studies by accurately replicating the actual in-field stress conditions. The deformation of a soil element depends on stress, strain, and time. Therefore, centrifuge tests offer a unique opportunity to create model case histories replicating the estimated stress conditions in the field. Additionally, it allows researchers the opportunity to repeat experiments under different conditions. In geotechnical models, stresses must be maintained between the model and the prototype. Centrifuge tests offer a controlled environment where the properties of the liquefiable layer can be defined and controlled. Further, dense instrumentation arrays of the soil profile and the structures allow for the monitoring of system behavior during and after shaking. This capability enables replicating earthquake effects under known conditions, offering valuable insights into soil-structure interactions and structural responses. Table 3-1 describes the centrifuge scaling laws.

Compared to centrifuge model testing, 1g experiments are more straightforward and cost-effective but fail to replicate the actual stress field in the soil. These stresses tend to be lower in 1g conditions, so the soil's angle of shearing resistance tends to be significantly higher while the small-strain stiffness is lower. These discrepancies can notably affect the measured system response and impact on structures, making it essential to interpret 1g test results cautiously.

Table 3-1 Scale factors for centrifuge model tests from (Kutter, 1992).

Quantity	Symbol	Units	Scale Factor
Length	L	L	N^{-1}
Volume	ν	L^3	N^{-3}
Mass	M	M	N^{-3}
Gravity	g	LT^{-2}	N
Force	F	MLT^{-2}	N^{-2}
Stress	σ	$ML^{-1}T^{-2}$	1
Moduli	E	$ML^{-1}T^{-2}$	1
Strength	s	$ML^{-1}T^{-2}$	1
Acceleration	a	LT^{-2}	N
Time (dynamic)	then	T	N^{-1}
Frequency	F	T^{-1}	N
Time (diffusion)	t_{dif}	T	N^{-1} or N^{-2}

The diffusion time scale factor depends on whether the diffusion coefficient (e.g., coefficient of consolidation) is scaled. If the same soil is used in the model and prototype, t_{dif}=N^{-2}

A common approach to address scaling laws associated with earthquake-induced pore pressure generation in geotechnical modeling is to use a pore fluid with a higher viscosity than water. Previous studies have utilized fluids like silicone oil and methylcellulose. However, as Stewart et al. (1998) detailed, silicone oil has several disadvantages. As a result, methylcellulose has emerged as the preferred alternative. According to Stewart et al. (1998), methylcellulose offers the following advantages: (1) it is environmentally friendly, non-hazardous to the skin, and easy to clean; (2) it mixes easily with water and can achieve a range of viscosities; (3) its water content can be determined through evaporation if the methylcellulose concentration is known; (4) its unit weight closely matches that of water, reducing the need for adjustments; and (5) it is inexpensive and readily available. Figure 3-1 illustrates the relationship between the solution concentration of hydroxypropyl methylcellulose powder (HPMC) and kinematic viscosity at 20°C.

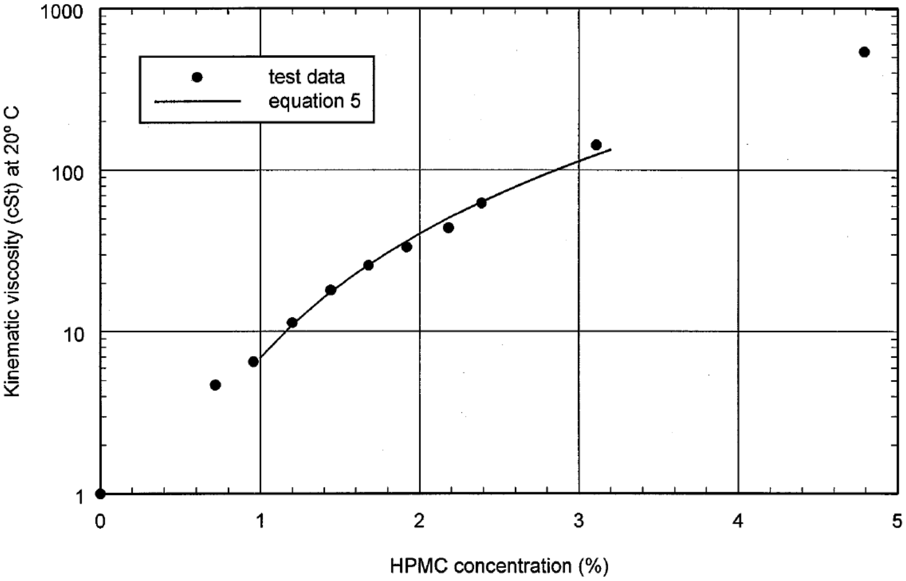

Figure 3-1 The viscosity of Grade F Methocel HPMC as a function of concentration (1 cyst = 10^{-6} m^2/s) from (Stewart et al., 1998).

3.2 Overview of Previous Centrifuge Experiments

Liu and Dobry (1997) investigated the mechanisms of liquefaction-induced settlements of shallow foundations using a series of eight 3-m centrifuge tests performed at the Rensselaer Polytechnic Institute (RPI) centrifuge. The tests examined the performance of circular rigid blocks (B = 4.56 m (14.96 ft) at prototype scale) on loose liquefied Nevada sand (D_R=52%) at 80 *g*. The thickness of the sand profile was about 12.5 m (41 ft) in prototype scale. The groundwater was placed at the surface for all tests. The models were shaken with the 1990 Luzon and 1964 Niigata motions with an average acceleration of 0.2 *g*. They also explored mitigation methods through soil densification using vibro-compaction, variations in soil permeability, changes of excess pore pressure generation, and redistribution around the footing. The study found the footing experienced significant settlement before the soil improvement, more than twice the free-field settlement. Most of the settlement occurred during shaking, and only a small portion occurred during post-liquefaction reconsolidation. The settlement was caused by rapid excess pore pressure generation underneath the footing, causing soil softening and significant punching during shaking. When soil improvement was applied through vibro-compaction, the results showed a significant reduction in settlement as the depth of compaction increased. When the compaction depth reached 1.5*B* to 2.76*B* (depths between 6.8 m (22.3 ft) and 12.5 m (41 ft) in prototype scale), the settlement decreased by more than 50%, and the settlement ratio (foundation settlement/free-field settlement) approached unity, indicating that the soil under and around the foundation settled uniformly.

Additionally, the results revealed that compacting beyond a depth of 1.5*B* had a minor effect on reducing the settlement. The researchers concluded that additional investigation is needed to establish whether these results are specific to the model tests or applicable to various foundation load combinations, geometries, liquefiable layer characteristics, and shaking durations and intensities.

Dashti et al. (2010a) conducted three centrifuge experiments at the University of California, Davis Center for Geotechnical Modeling (CGM) to study liquefaction-induced building settlement on shallow foundations. All tests were spun at 55g. The centrifuge models used a layered soil profile on loose Nevada sand as the liquefiable material and range of relative densities (D_R = 30% to 50%). The models had varied liquefiable layer thicknesses (T_L) (from 3 m to 6 m (9.8-19.7 ft) on the prototype scale). The surficial dense Monterey sand layer was used to minimize capillary rise and liquefaction directly below the footings.

Three shaking input motions (Moderate Port Island, Moderate TCU, and large Port Island) were applied at the base of models T6-30 (SHD01), T3-30 (SHD02), and T3-50 SILT (SHD04). The Moderate Port Island motions consisted of scaled versions of the north-south fault-normal component of the M_w 6.9 ground motion recorded in the Kobe Port Island down-hole array during the 1995 Kobe, Japan earthquake. The moderate TCU78 event is a modified and scaled version of the 1999 M_w 7.6 Chi-Chi, Taiwan Earthquake. The Port Island events' target peak base accelerations (PBA) were 0.19 and 0.55g. The TCU078 motion was selected for its longer duration and slower rate of energy buildup compared to the Port Island events. It was scaled to achieve a similar PBA as the moderate intensity Port Island Earthquake (0.13 – 0.15g). Table 3-2 shows the stratigraphy, structural properties, input motions, and seismic parameters for each model tested. Figure 3-2 lays out a schematic of the T3-30 model.

Table 3-2 Summary of centrifuge testing program (from Dashti et al., 2010b).

			Prototype input ground motion characteristics			
Test ID	Liquefiable layer prototype thickness/D_r	Structural models	Record	Peak acceleration (g)	Significant duration D_{5-95} (s)	Arias intensity I_a (m/s)
T6-30	6 m/30%	Two-story building on rigid mat foundation with: A: $W\times L\times H=6\times9\times5$ m B: $W\times L\times H=12\times18\times5$ m C: $W\times L\times H=6\times9\times9.2$ m	Moderate Port Island 1995 Kobe	0.18	8	0.4
T3-30	3 m/30%					
T3-50-SILT	3 m/50%; with silt on top of liquefiable soil		Large Port Island 1995 Kobe	0.55	9	4.5
T3-50	3 m/50%	Two-story building on rigid mat foundation ($W\times L\times H=6\times9\times5$ m) with: BL: base-line; SW: stiff structural wall; WB: latex water barrier	Moderate Port Island 1995 Kobe	0.15	8	0.3
			TCU078 1999 Chi-Chi	0.13	28	0.6
			Large Port Island 1995 Kobe	0.38	11	2.7

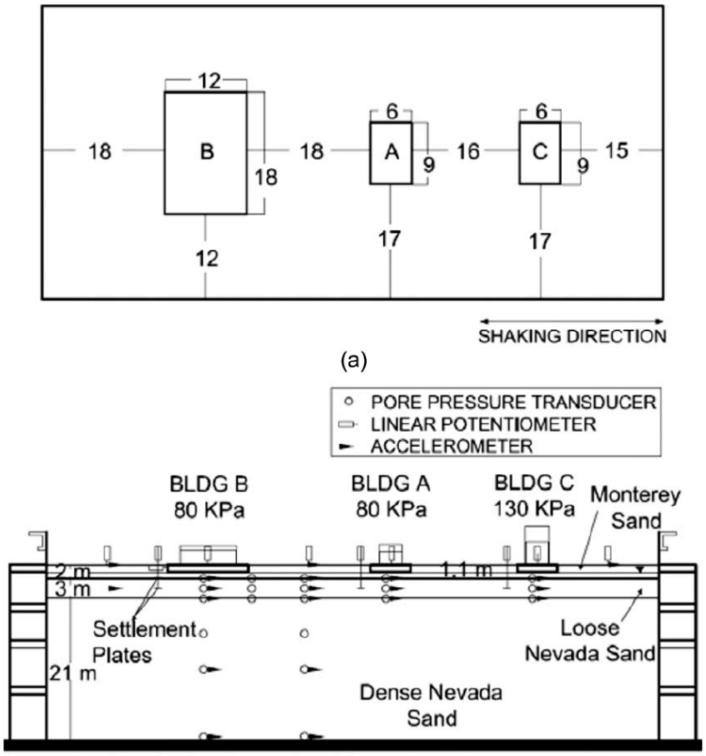

(a)

(b)

Test ID	Liquef. Layer Prototype Thickness / D_r
T3-30	3 m / 30%
T3-50-SILT	3 m / 50% (with silt placed on top of the liquefiable layer)
T6-30	6 m / 30%

(c)

Figure 3-2 Centrifuge model layout in experiment T3-30 with most of the approximately 120 transducers omitted for clarity: (a) plan view, (b) cross-section view, and (c) centrifuge testing program. All dimensions are given in prototype scale in meters from (Dashti et al., 2010a).

Dashti et al. (2010b) identified that most liquefaction-induced building settlements occurred during the strong shaking phase, contrary to the traditional post-liquefaction reconsolidation for free field settlements. Building settlement during shaking is driven by cyclic soil-structure-interaction (SSI), localized deviatoric strains, and volumetric strains induced by partial drainage and void redistribution. The governing mechanisms that occur in the centrifuge tests were categorized as: a) volumetric types: rapid drainage ($\varepsilon_{p\text{-}DR}$), sedimentation ($\varepsilon_{p\text{-}SED}$), and consolidation ($\varepsilon_{p\text{-}CON}$), and b) deviatoric types: partial bearing capacity loss ($\varepsilon_{q\text{-}BC}$), and SSI induced building ratcheting ($\varepsilon_{q\text{-}SSI}$) as described in Section 1.2. Table 3-3 describes the mechanisms that affect liquefaction-induced building settlement. Table 3-4 details how the mechanisms are affected by different test condition parameters.

Table 3-3 Primary mechanisms of ground and building displacement from Dashti et al. (2010a).

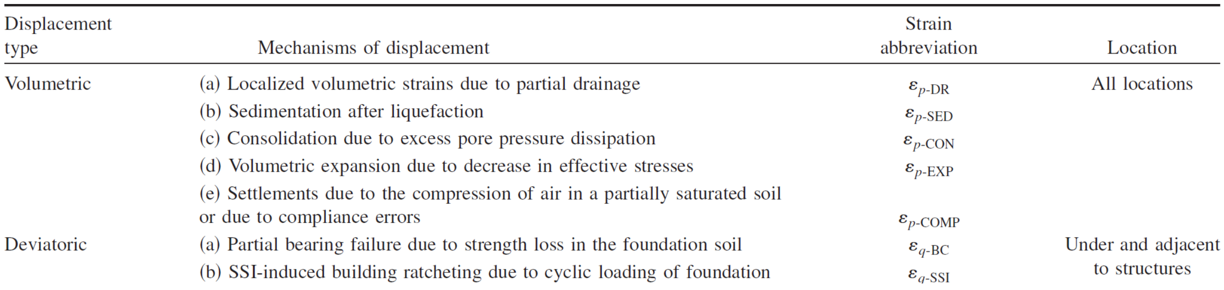

Displacement type	Mechanisms of displacement	Strain abbreviation	Location
Volumetric	(a) Localized volumetric strains due to partial drainage	$\varepsilon_{p\text{-DR}}$	All locations
	(b) Sedimentation after liquefaction	$\varepsilon_{p\text{-SED}}$	
	(c) Consolidation due to excess pore pressure dissipation	$\varepsilon_{p\text{-CON}}$	
	(d) Volumetric expansion due to decrease in effective stresses	$\varepsilon_{p\text{-EXP}}$	
	(e) Settlements due to the compression of air in a partially saturated soil or due to compliance errors	$\varepsilon_{p\text{-COMP}}$	
Deviatoric	(a) Partial bearing failure due to strength loss in the foundation soil	$\varepsilon_{q\text{-BC}}$	Under and adjacent to structures
	(b) SSI-induced building ratcheting due to cyclic loading of foundation	$\varepsilon_{q\text{-SSI}}$	

Table 3-4 Effect of key parameters on the dominant displacement mechanisms, assuming a shallow liquefiable layer underlying a large mat foundation on Dashti et al. (2010a).

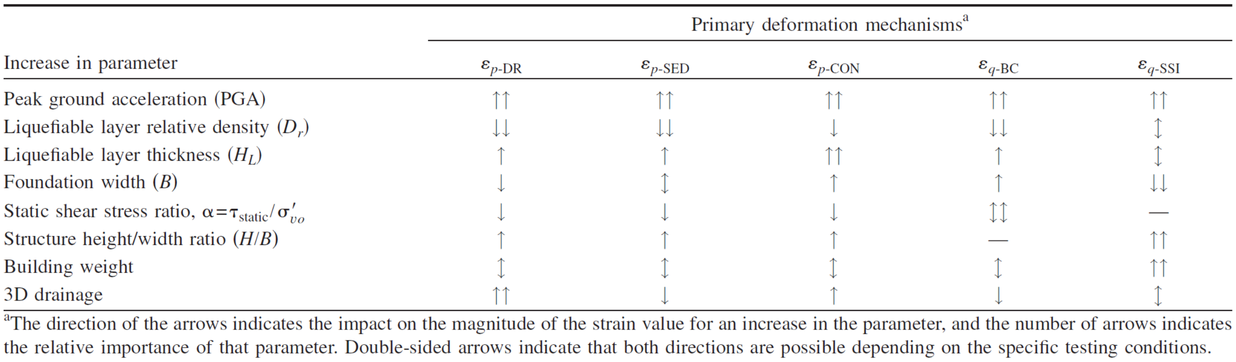

	Primary deformation mechanisms[a]				
Increase in parameter	$\varepsilon_{p\text{-DR}}$	$\varepsilon_{p\text{-SED}}$	$\varepsilon_{p\text{-CON}}$	$\varepsilon_{q\text{-BC}}$	$\varepsilon_{q\text{-SSI}}$
Peak ground acceleration (PGA)	↑↑	↑↑	↑↑	↑↑	↑↑
Liquefiable layer relative density (D_r)	↓↓	↓↓	↓	↓↓	↕
Liquefiable layer thickness (H_L)	↑	↑	↑↑	↑	↕
Foundation width (B)	↓	↕	↑	↑	↓↓
Static shear stress ratio, $\alpha=\tau_{\text{static}}/\sigma'_{vo}$	↓	↓	↓	↕↕	—
Structure height/width ratio (H/B)	↑	↑	↑	—	↑↑
Building weight	↕	↕	↕	↕	↑↑
3D drainage	↑↑	↓	↑	↓	↕

[a]The direction of the arrows indicates the impact on the magnitude of the strain value for an increase in the parameter, and the number of arrows indicates the relative importance of that parameter. Double-sided arrows indicate that both directions are possible depending on the specific testing conditions.

Different structural configurations were designed and compared to the free field results to represent different types of buildings, stresses and study different SSI behaviors:

- Structure A: Consisted of a 2-story building with moderate width (6 m (19.7 ft)) and height (5 m (16.4 ft)) and a bearing pressure of 80 kPa (1671 psf). The structure experienced cyclic soil-structure interaction, rapid drainage, and partial bearing capacity loss. Results showed moderate total settlement (~230-480 mm (9-19 in)) with limited differential settlement (~0.5% tilt) due to controlled cyclic SSI effects.
- Structure B: Structure B is the same height as Structure A but with a broader footprint area to distribute stresses and the same bearing pressure of 80 kPa (1670 psf). The structure experienced reduced cyclic SSI as the dominant mechanism and faster drainage. Results showed a smaller total settlement (~120-280 mm (4.7-11 in)) due to the broader foundation distributing stresses more effectively and minimal tilt (~0.1% differential settlement).
- Structure C: Structure C is a taller building with a higher height-to-width (H/B) ratio of 1.53 and increased bearing pressure of 130 kPa (2715 psf), simulating a multi-story building. The structure experienced severe cyclic SSI, rapid drainage, and significant bearing capacity loss. Results showed severe total settlement (around 350 to 720 mm (13.7 to 28.3 in)) and substantial differential settlement (~1.2% tilt), making it the most affected structure during intense shaking.
- Structure BL (Baseline for remediation tests): Structure BL is the "baseline" structure used in the model that studied mitigation in liquefaction (T3-50) without additional reinforcement. The bearing pressure was 80 kPa (1671 psf). Structure BL experienced a combination of cyclic SSI and rapid drainage similar to Structure A. Results showed significant settlement (around

230 to 470 mm (9-18.5 in)) due to the absence of mitigation schemes and moderate tilt (~0.5%).

- Structure SW (with stiff structural wall for mitigation): Structure SW was surrounded by stiff structural walls designed to limit shear deformation and water migration at the base. The bearing pressure was 80 kPa (1671 psf). The walls effectively reduced cyclic SSI and localized pore pressure generation, achieving a 40-55% reduction in total settlement (around 130 to 260 mm (5-10 in)) compared to the structure BL but increased tilt (~0.8% differential settlement) due to restricted lateral movement by the structural walls.
- Structure WB (with water migration barrier for mitigation): Structure WB was placed over an in-ground water barrier to inhibit horizontal pore pressure migration. The bearing pressure was 80 kPa (1671 psf). The water barrier reduced volumetric settlement by controlling drainage and void redistribution but did not mitigate cyclic SSI effects. A 25-30% reduction in total settlement (~170-350 mm (7-14 in)) with minimal tilt (~0.2% differential settlement) was achieved.
- Free Field: Total settlement was 47-50% lower than under-structure settlements due to the absence of deviatoric mechanisms. The primary mechanism was post-liquefaction reconsolidation settlement followed by volumetric settlement, but these were less localized compared to the structure conditions.

Figure 3-3 shows the total permanent building settlements normalized by the initial thickness of the liquefiable layer (T_L) during the Port Island event for the experiments T6-30, T3-30, and T3-50 SILT. It compares them to case histories and other centrifuge tests. Structures A and B exhibited lower normalized settlements compared to the taller and heavier Structure C.

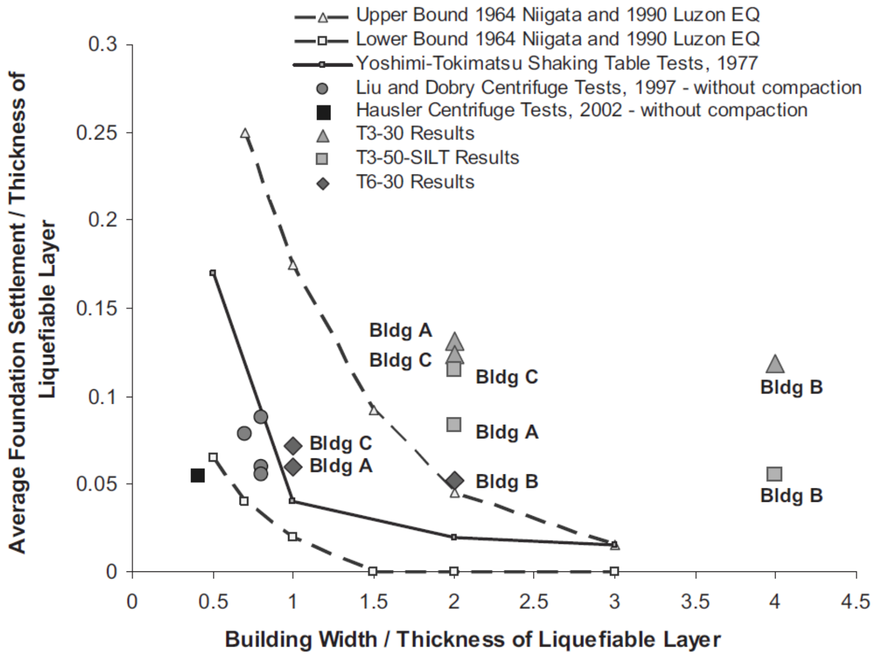

Figure 3-3 Normalized foundation settlements were measured in the three centrifuge experiments performed in this study during the significant Port Island event, compared to the available case histories and previous physical model tests from Dashti et al. (2010a).

Arias intensity was calculated for each test as an index representing energy accumulation of the ground motion (Arias, 1970). However, the shaking intensity rate (*SIR*) provides a better understanding of the rate at which the seismic energy is transmitted into the soil than PGA, influencing the rapid pore pressure generation and, consequently, SSI deformations during shaking. I_{a5-75} is the change in the Arias Intensity from 5 to 75% of its total value and D_{5-75} is its corresponding time duration. Higher *SIR* values are associated with faster rates of building settlement and greater total building settlement.

$$I_a(t) = \frac{\pi}{2g}\int_0^T a^2\,(t)dt \tag{1}$$

$$SIR = I_{a5-75}/D_{5-75} \tag{2}$$

Dashti et al. (2010b) showed that high *SIR* values, observed in the large Port Island ground motions (PBA= 0.55g), led to faster pore pressure buildup and severe settlements, which occurred due to both volumetric ($\varepsilon_{p\text{-}DR}$ and $\varepsilon_{p\text{-}SED}$) and deviatoric ($\varepsilon_{q\text{-}BC}$ and $\varepsilon_{q\text{-}SSI}$) mechanisms. During the Port Island shakes, the soil beneath the building foundations experienced faster and more extensive excess pore pressure softening. This led to significant dynamic soil-structure interaction and ratcheting-induced settlement. In contrast, the TCU078 earthquake produced a more gradual pore pressure accumulation, smaller *SIR*, and liquefaction-induced settlements.

Mason et al. (2013) conducted three 9-m-scale centrifuge experiments at 55 *g* at the CGM to investigate seismic soil-foundation-structure interaction (SFSI) and structure-soil-structure interaction (SSSI) effects on frame structures and shallow foundations without liquefaction. The tests included a single-story frame on shallow spread footings and a three-story frame on a deep basement. Both structures were placed on dry, dense Nevada Sand (D_R = 80%). The project studied near-fault, forward directivity ground motions representing the Los Angeles dense urban area. The test results showed that SFSI altered structural responses through rocking, sliding, and settlements compared to the traditional fixed-base assumptions for shallow foundations. Structures adjacent to each other showed SSSI effects, where the basement structure restrained the adjacent footings, reduced settlements but increased tilting, rocking and sliding. Moreover, the tests showed that kinematic interaction effects filtered high-frequency content and a reduction in the spectral accelerations for the foundation level compared to the surface free-field ones.

Trombetta et al. (2014) performed two experiments at 55 *g* at the CGM to study the seismic soil-foundation interaction-structure interaction, SFSI, and SSI between adjacent buildings on shallow foundations without liquefaction. The experiments involved a low-rise inelastic frame structure on spread footings and a mid-rise elastic shear-wall structure on a mat foundation. The structures were placed on dry, dense Nevada sand (D_R = 80%) and subjected to the motions previously discussed in Mason et al. (2013). The project scope was to study interactions under in-plane (iSSSI) and anti-plane (aSSSI) structural configurations under seismic shaking. During the shaking events the physical restraint imposed by adjacent structures effectively reduced settlements and large rotations but increased dynamic footing pressures. This restraint led to asymmetric nonlinear responses, where stiffness and moment capacities varied depending on the oscillating vertical loads. As vertical loads increased, the footing stiffness increased, but decreasing loads caused rotational stiffness degradation. Additionally, it was observed that wave-based SSSI effects had little influence on the seismic response of inelastic frame structures.

Allmond et al. (2015) introduced the new foundation-liquefaction database (FLIQ), which contains data from nine large-scale centrifuge experiments conducted at the CGM at 55g. The database contains 405 modeled case histories across 49 instrumented structural and free-field stations, covering a range of soil profiles, structural configurations, modeling properties, seismic parameters and input motions which are shown in Table 3-5 and Table 3-6. The tests consisted of shallow embedded footings that were subjected to varying bearing pressures ranging from 50 kPa (1044 psf) to 160 kPa (3342 psf). The studies for shallow liquefiable soils consisted of loose to medium-dense Nevada Sand with D_R ranging from 30%

to 50%, and 80% for the denser layers simulating field conditions. This information is critical for future development of centrifuge models to assess liquefaction-induced settlement.

Table 3-5 Structures from past CGM tests at 55g from Allmond et al. (2015).

Bldg. name	Scale factor	Width, B (m)	Length, L (m)	Thickness, t (m)	Height to mass, H_{cm} (m)	Bldg. mass, M_s (Mg)	Embedment depth, d_f (m)	Bearing pressure, q (kPa)	Fixed-base period, T_n (s)
A	55	6	9	0.7	2.12	358	0.7	80	0.21
B	55	12	18	0.7	2.12	1,321	0.7	80	0.26
C	55	6	9	0.7	4.20	551	0.7	130	0.33
J	55	7.5	7.5	1.4	10.45	1,050	1.4	179	0.87
K	55	6	9	0.7	2.42	989	0.7	177	0.32

Allmond et al. (2015) explored the cumulative absolute velocity (*CAV*) with a 0.005g threshold acceleration as an intensity measure (Equations 3 and 4). They found that *CAV* correlates well with the settlement time history, and it offers a better understanding of the seismic forces contributing to structural deformation and energy buildup compared to previous seismic intensity measures such as peak ground acceleration (PGA). High-intensity peaks in the time history do not simply trigger liquefaction and settlement. Instead, they result from the accumulation of cyclic loading, during which excess pore pressures develop progressively over time.

$$CAV = \int_{0}^{tmax} |a(t)|dt \tag{3}$$

$$CAV_{cap} = \int_{0}^{\infty} \langle x \rangle\, |a(t)|dt \; where \; \langle x \rangle = \begin{cases} 0 \; for \; |a(t)| < cap \\ 1 \; for \; |a(t)| < cap \end{cases} \tag{4}$$

Figure 3-4 shows the relationship between building and free-field settlements during moderate and large shaking events. During moderate events, structures with higher bearing pressures exhibit smaller settlements than in the free-field. The relative settlement is described as the difference between the settlement of the building and the free-field. When the relative settlement is less than zero, the structures settled less than the surrounding free field. On the contrary, heavier structures with higher bearing pressures settled less than some lighter structures during moderate events. This is caused by the increased confining stress imposed by the structure on the shallow liquefiable layer, which reduces the potential for liquefaction by increasing the initial effective stress and reducing the excess pore pressure generation (Allmond et al. 2015).

Hayden et al. (2015) conducted two 9-m-scale centrifuge experiments at 55g at the CGM to investigate the impact of liquefaction on adjacent mat-supported structures and isolated buildings, focusing on the structure-soil-structure interaction (SSSI) of neighboring structures. T4.5-50 and T4.6-40 tests involved loose to medium-dense Nevada sand (D_R of 40% and 50%). The structural models included three types of SDOF buildings, representing buildings with varying heights and bearing pressures ranging from 65 to 186 kPa (1358 to 3885 psf), as shown in Table 3-7. Figure 3-5 lays out the experiment setup and stratigraphy.

Table 3-6 Stratigraphy from past CGM tests at 55 g from Allmond et al. (2015).

[a]Test	Water depth (m)	Fluid viscosity (cSt)	Soil layer	Height (m)	[b]Soil type	D_R	G_s	e_{min}	e_{max}	Test Name (Researcher) Data Report Reference NEEShub Project No. DOI Reference
T6-30	1.10	20	L3	2	M	86%	2.64	0.541	0.855	SHD01
			L2	6	N	30%	2.67	0.533	0.888	Dashti (2009), Appx. I
			L1	18		86%				[c]NEES-2006-0224-Exp 1
T3-30	1.10	22	L3	2	M	90%	2.64	0.541	0.855	SHD02
			L2	3	N	30%	2.67	0.533	0.888	Dashti (2009), Appx. II
			L1	21		90%				[c]NEES-2006-0224-Exp 2
T3-50-	1.10	22	L4	1.2	M	85%	2.64	0.541	0.855	SHD03
SILT			L3	0.8	S	n/a	2.66	n/a	n/a	Dashti (2009), Appx. III
			L2	3	N	50%	2.64	0.52	0.78	[c]NEES-2006-0224-Exp 3
			L1	21		90%				
T3-50	1.10	22	L3	2	M	85%	2.64	0.536	0.843	SHD04
			L2	3	N	50%	2.65	0.520	0.780	Dashti (2009), Appx. IV
			L1	21		90%				[c]NEES-2006-0224-Exp 4
T3.9-50	−0.70	11	L3	2.8	AG	90%	2.65	0.48	0.70	JDA01
			L2	3.9	N	80%	2.66	0.52	0.77	Allmond and Kutter (2012)
			L1	16.8	N	50%	2.66	0.52	0.77	NEES-2008-0565-Exp 4
						80%				10.4231/D3C53F17M
T2.5-55	0.00	11	L3	2.6	N	80%	2.66	0.52	0.77	JDA02
			L2	2.5		55%				Allmond and Kutter (2013)
			L1	20.7		80%				
T2.3-70	−1.40	11	L3	2.5	N	90%	2.66	0.52	0.77	NEES-2008-0565-Exp 6
			L2	2.3		70%				10.4231/D37D2Q74Z
			L1	20.6		90%				
T4.5-50	0.70	21	L3	1.9	M	85%	2.64	0.536	0.843	JDZ01
			L2	4.5	N	50%	2.66	0.516	0.774	Zupan et al. (2013)
			L1	19.4		90%				NEES-2008-0639-Exp 6
										10.4231/D39W08Z6N
T4.6-40	0.20	21	L3	1.7	M	85%	2.64	0.536	0.843	CPH01
			L2	4.6	N	40%	2.66	0.516	0.774	Hayden et al. (2014)
			L1	19.3		90%				NEES-2008-0639-Exp 7
										10.4231/D3QF8JJ99

[a]Test = T[*Liquefiable Layer Thickness*] − [D_R *of Liquefiable Layer*] − [*Additional Classification*].
[b]Soil Type = M: Monterey Sand; N: Nevada Sand; S: Silt, AG: Aquarium Gravel.
[c]DOI Not Available.

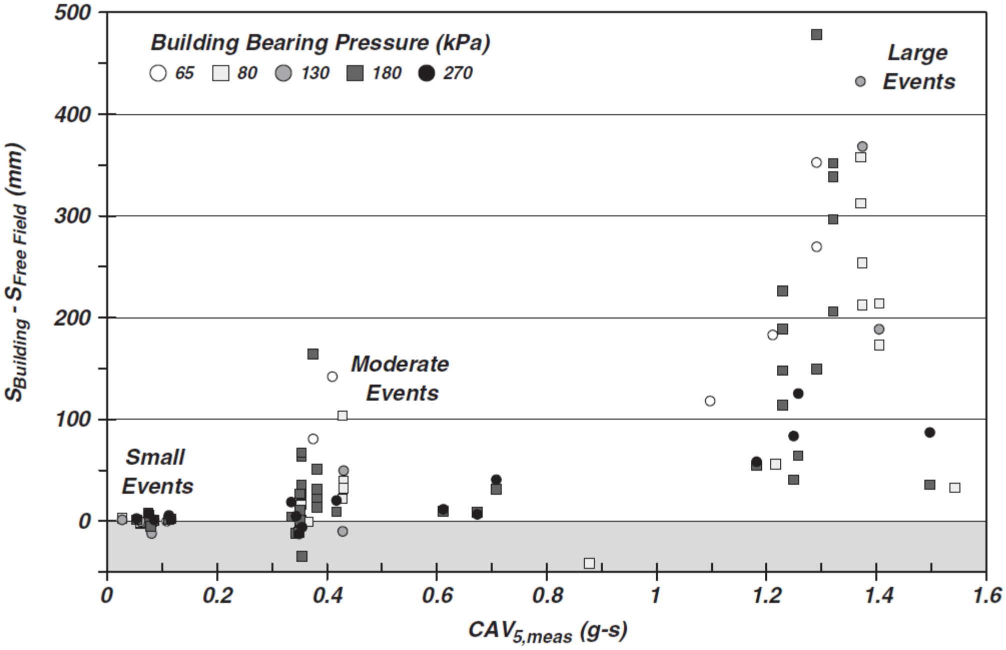

Figure 3-4 Building settlements relative to free-field ground surface versus incremental CAV_5, measured recordings for each event from Allmond et al. (2015).

Table 3-7 Structural properties of tests T4.5-50 and T4.6-40 from Hayden et al. (2015).

Structure	Mat width (m)	Mat length (m)	Height (m)	Weight (kN)	Bearing pressure (kPa)	Fixed-base period (s)[a]	Center of mass (m)[b]
A	6.0	9.0	4.4	3,510	65	0.33	3.9
K	6.0	9.0	5.3	9,700	180	0.38	3.9
J	7.5	7.5	13.5	10,470	186	0.85	15.0

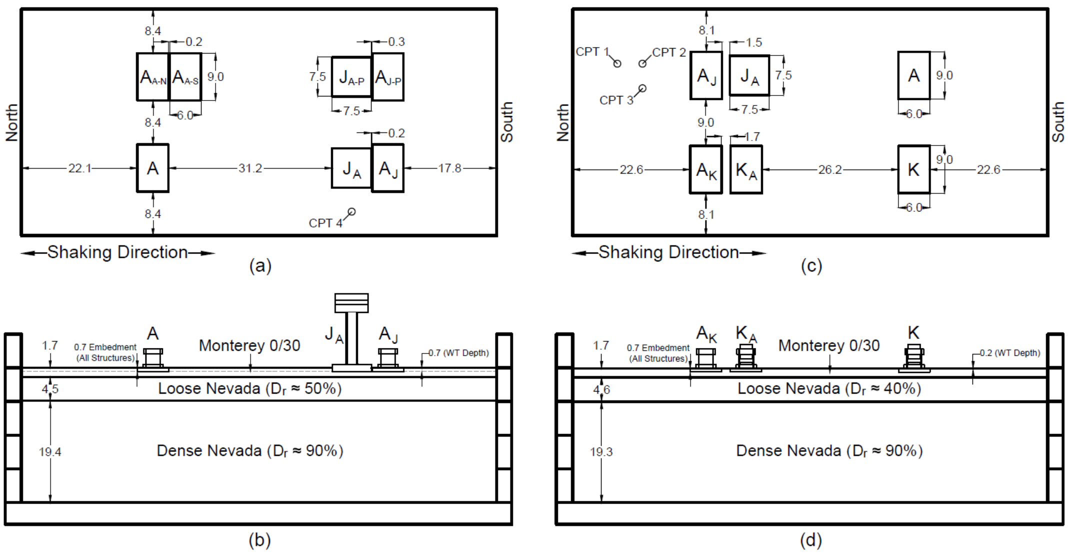

(a) (c)

(b) (d)

Figure 3-5 Centrifuge test layout with prototype dimensions in meters : (a) T4.5-50 plan view; (b) T4.5-520 profile view; (c)T4.6-40 plan view; (d) T4.6-40 profile view (from Hayden et al. 2015).

The tests showed that SSSI effects significantly reduced settlements and spectral accelerations under adjacent structures compared to isolated buildings. Adjacent structures tilted away from one another, reducing their total settlement and limiting lateral soil movement beneath them due to physical restraint. The heavier structures (J and K types) generated higher initial vertical effective stresses, inhibiting pore pressure generation beneath their foundations. During moderate shaking, these heavier footings experienced lower excess pore water pressures ($r_u = 0.3$ to 0.4), resulting in less severe settlements than lighter structures like the A-type. However, settlements under all structures increased substantially for larger shaking events, with A-type structures often settling more than twice the free-field settlement. Structures near each other exhibited lower spectral accelerations due to the physical restraint imposed by the neighboring foundations. Additionally, the horizontal separation distances between adjacent structures increased during both more significant and moderate shaking (Hayden et al. 2015).

Bertalot and Brennan (2015) conducted three 3-m-centrifuge tests at 50 *g*, where each model included four rigid square footings (B = 2.75 m (9 ft) at prototype scale) with varying bearing pressures (60 kPa (1253 psf), 90 kPa (1870 psf), and 130 kPa (2715 psf)) placed on loose liquefiable sand layers (D_R = 40%) of different thicknesses overlying a bottom dense layer (D_R = 80%). Each foundation was embedded 0.5 m (1.6 ft) below the ground surface. During earthquake shaking, they observed soil softening due to excess pore pressure generation beneath the footing edge for footings exerting high bearing pressures (greater than 100 kPa (2090 psf)) on the soil. Likewise, settlements on liquefiable soils tended to increase for bearing pressures greater than 100 kPa (2090 psf). However, the above settlements may begin to decrease as the initial shear stresses in the soil inhibit pore pressure generation.

Adamidis and Madabushi (2018) investigated the response of structures on shallow foundations resting on liquefiable layers of varying thickness. Following Liu and Dobry (1997), they normalized the structure's width by the liquefied layer thickness to differentiate between thin and thick layers. For thick liquefiable layers, settlement was attributed to increased lateral soil displacements beneath a bulb of stiffer soil forming below the foundation, extending approximately one foundation width (1*B*), a pattern that persisted for lighter structures regardless of shaking intensity. However, under motions with many load cycles, heavier structures accumulated embedment and responded by rocking, causing localized deformation at the foundation edges. In thin liquefiable layers, the stiffer soil extended only to the foundation base, transmitting large accelerations and inducing rocking, with SSI ratcheting ($\varepsilon_{q\text{-}SSI}$) becoming the dominant settlement mechanism.

3.3 Key Insights

Experimental studies provide important insights regarding the performance of shallow building foundations on liquefiable ground. The key findings from past centrifuge experiments are:

- Centrifuge tests demonstrated that most liquefaction-induced settlement mainly occurred during the intense ground shaking phase of the input motion.

- Several researchers (e.g., Bray & Dashti, 2014) have emphasized that total settlement near or beneath a structure exceeds free-field settlement, primarily because shear-induced settlement is the predominant mechanism contributing to structural settlement. Post-liquefaction reconsolidation played less important role in structure settlement relative to the surrounding ground for the range of conditions investigated.

- Shaking Intensity Rate (*SIR*) better captures the rate at which the seismic energy is transmitted to the soil compared to other intensity measures. Higher *SIR* leads to a faster excess pore pressure generation and larger settlement. CAV was found to correlate well with the settlement's time history. When using a 0.005 *g* threshold, dilation spikes are suppressed, making CAV_5 an ideal candidate to account for liquefaction evaluation and settlement estimates.

- During some moderate shaking events, foundations with higher bearing pressures experienced less settlement than those with lighter bearing pressures and even less than the free-field settlement.

- Several experiments showed that kinematic interaction effects filtered high-frequency content and a reduction in the spectral accelerations for the foundation level compared to the surface free-field ones.

- Physical restraints imposed by adjacent structures can reduce settlements and large rotations but can also temporarily increase dynamic footing pressures.

- Different mitigation measures can reduce specific types of settlements but may be ineffective for others. For example, Dashti et al. (2010b) showed that adding water barriers to inhibit horizontal pore pressure migration can reduce volumetric settlement by controlling drainage and void ratio distribution, but it does not mitigate cyclic soil-structure-interaction (SSI) effects.

- Soil liquefaction effects on structures are most significant when the liquefiable layers are shallow. When looser soils were improved in an experiment to depths of $1.5B$ below shallow-founded structures of width B, the settlement decreased by more than 50% from the cases before ground improvement. Moreover, the settlement ratio (foundation settlement/free-field settlement) approached unity, indicating that the soil under and around the foundation settled uniformly. Additionally, the experimental results revealed that compacting beyond a depth of $1.5B$ had a minor effect on reducing the settlement for these tests. However, the applicability of these findings might be case-specific and require further study for confirmation.

Chapter 4 NUMERICAL STUDIES

4.1 Introduction

Numerical simulations enable engineers to explore complex interactions between soil and structures during seismic events. They can provide valuable insights that enhance our understanding of potential vulnerabilities and the overall seismic performance of engineered systems. Numerous field case histories and physical experiments have provided data that have validated various numerical methods, which confirms their effectiveness in capturing the intricate responses of soil under dynamic loadings.

Analytical methods, such as the Finite Element Method (FEM) and the Finite Difference Method (FDM), require sophisticated constitutive models to capture the phenomenon of soil liquefaction and evaluate its effects on structures. The selection of a robust soil constitutive model is essential for accurately simulating soil-structure interaction (SSI) problems, which are critical to evaluating foundation performance during earthquakes.

This chapter provides an overview of different analytical methods employed in SSI numerical simulations of structures affected by soil liquefaction. It then introduces some of the most widely used constitutive models before reviewing insightful parametric studies of the performance of shallow foundations on liquefiable layers, which identify mechanisms that contribute to the seismic performance of structures and delineate the key parameters that govern the response of the soil-structure system.

4.2 Analytical Procedures

4.2.1 Overview of Analytical Methods

There are numerous analytical methods that can be used in geotechnical earthquake engineering analysis. This section briefly describes some of these methods as well as summarize their advantages and disadvantages. Among these, the Finite Element Method (FEM) and Finite Difference Method (FDM), are the most widely applied in SSI analyses. The Discrete Element Method (DEM) and Material Point Method (MPM) have been used far less frequently in studies to date. However, these methods hold potential for broader application in future research.

Finite Element Method:

FEM is commonly applied to cases with complex geometries or materials that are inhomogeneous and respond nonlinearly. FEM discretizes the material into smaller elements connected by nodes, which allows for capturing local variations in stresses, strains, and displacements, particularly under varying loading conditions such as cyclic loading. FEM typically employs an implicit solution algorithm that requires the development of a large stiffness matrix to solve the system of equilibrium equations. The main steps in FEM analysis involve discretizing the model into finite elements, deriving element-specific equations, assembling these into a global system, and then solving the global equations to find displacements or other parameters of interest at each node. While FEM's adaptability makes it well-suited for complex models, large-scale applications can be computationally intensive due to the typical implementation of an implicit solution algorithm, especially when simulating nonlinear material responses or SSI to solve geotechnical earthquake engineering problems (Potts & Zdravkovic, 1999).

Finite Difference Method:

FDM generally involves solving sets of differential equations explicitly based on given initial values or boundary values (e.g., FLAC software by Itasca 2019). In FDM, derivatives are replaced with algebraic expressions that relate variables, such as stress or displacement, at discrete points in space. FDM typically employs an explicit solution algorithm that uses the equations of motion to calculate new velocities and displacements from stresses and forces, with strain rates derived from velocities and new stresses computed based on these strain rates. FLAC utilizes the explicit FDM for analysis, which offers several advantages. It allows for faster calculations, as no iterative process is required to compute stresses from strains within elements, and the absence of matrix formation enables the method to handle large strain and strain softening effects without much additional effort. However, the explicit method has its limitations, as solutions are sensitive to the selected time step; it must be smaller than a critical value to ensure stability (Itasca Consulting Group, Inc., 2019).

Discrete Element Method:

DEM is commonly used to model granular materials by performing calculations that trace the response of individual particles (Coetzee, 2001). At each time step, with the contact forces between particles known, Newton’s second law is applied to derive the equations of motion. The equations of linear and rotational motion are determined by summing the forces and moments acting on each particle from its neighboring particles (Tanaka, Nishida, & Kunimochi, 2001). Unlike continuum-based methods such as the FEM and FDM, DEM is particularly helpful for modeling large displacements, deformations, and phenomena such as mixing and segregation of granular materials. It has been more widely used in applications like rock mechanics, fracture modeling, and rock crushing cutting due to the increased number of particles required to solve soil mechanic problems. A notable drawback of DEM is its high computational cost, particularly for applications where particle interactions are not the primary focus (Coetzee, 2001).

Material Point Method:

MPM represents the material as a collection of discrete material points. The motion of each material point is governed by Newton’s laws of motion. MPM adopts a hybrid Eulerian-Lagrangian approach, combining the advantages of moving material points (Lagrangian perspective) with a fixed computational grid (Eulerian perspective) (Soga Research Group, 2023). This dual framework makes MPM especially effective for simulating large deformations, where traditional mesh-based methods often encounter issues like severe mesh distortions that lead to unrealistic results. An advantage of MPM is its ability to incorporate FEM constitutive models, making it a valuable alternative for problems that do not converge in FEM simulations. However, the method's accuracy depends on grid density and the number of material points, which can significantly increase computational time compared to FEM for achieving equivalent numerical accuracy (Solowski, et al., 2021).

4.2.2 Overview of Constitutive Models

Constitutive models describe the relationships between stresses and strains in a material. There are several constitutive models that are used in geotechnical earthquake engineering, each of them with specific advantages and limitations. This section provides an overview of a few constitutive models, with a particular focus on the PM4Sand model, which is widely used to capture the response of liquefied soil.

UBCSAND Model:

The UBCSAND model is a fully coupled effective-stress model that is used to capture the seismic response of liquefied soil exhibiting a ‘sand-like’ response in plane strain analysis. The model uses an assumed hyperbolic relationship to capture the shear stress-strain response of the soil and estimates the associated volumetric response of it using a flow rule that is a function of the current stress ratio, η. This model is a modified form of the Mohr-Coulomb model that accounts for strain-hardening frictional behavior while neglecting cohesion. Unloading in this model is assumed to be nonlinear elastic, with the material's bulk modulus and shear modulus as a function of the mean effective stress, whereas reloading is assumed to be elasto-plastic (Beaty, 2021).

The primary parameters in the model are: $k_G^p, k_G^e, \eta_f/R_f, \eta_{cv}, \upsilon, ne,$ and np, which are summarized in Table 4.1. These parameters are typically calibrated using field and laboratory experiments and several of them can be related to overburden-corrected Standard Penetration Test (SPT) blow count, $(N_1)_{60}$, making the model particularly convenient for practical applications (Voyagaki et al., 2023). Despite its widespread use, the UBCSAND has notable limitations: 1) stress reversal is solely based on horizontal shear stress, and 2) the formulation applies only to two-dimensional analysis (Beaty, 2021). Refer to Beaty et al (2021) for more information on this model.

Table 4.1 Model parameters in UBCSAND model

Symbol	Description
k_G^p	Dimensionless plastic shear modulus parameter
k_G^e	Dimensionless elastic shear modulus parameter
η_f	Stress ratio at failure
R_f	Failure ratio
η_{cv}	Stress ratio under constant volume
υ	Poisson's ratio
ne	Elastic shear modulus exponent
np	Plastic shear modulus exponent

Stress-Density Model:

The Stress-Density (SD) model was developed to capture the response of sand over a wide range of relative densities and the effectives stresses. This model is built within the framework of the state concept, which describes the mechanical response of sand using its initial state relative to some reference state (critical or steady state, quasi-steady state). The initial state is quantified using the state index (I_s), which combines the effects of the density and normal stress on the stress-strain response. The stress-strain response of sand is captured using a modified hyperbolic relationship that incorporates the influence of the initial void ratio and stress state (Cubrinovski & Ishihara, 1998). Additionally, an energy-based stress-dilatancy relationship is introduced to describe the soil's volume change tendencies (Cubrinovski & Ishihara, 1998). Table 4.2 lists the four groups of parameters used in this model, and Figure 4-1 illustrates a flow chart for modeling the stress-strain curve using an initial void ratio (e) and mean effective confining stress (p') (Cubrinovski & Ishihara, 1998). Refer to Cubrinovski & Ishihara (1998) for a detailed explanation of these parameters.

One of the primary advantages of the SD model is its ability to represent soil response with a specific fabric using a single set of material parameters, regardless of the initial e-p' state. Once the parameters listed in Table 4.2 are defined, the sand's response can be predicted for any initial conditions. However, determining these parameters requires extensive laboratory testing, including 12 to 15 tests such as monotonic undrained tests, monotonic drained constant-pressure tests, and cyclic undrained (liquefaction resistance) tests (Cubrinovski & Ishihara, 1998). Consequently, the accuracy of the laboratory test results plays a crucial role in the reliability of the analysis.

Table 4.2 Parameters used in Stress-Density model (from Cubrinovski & Ishihara, 1998).

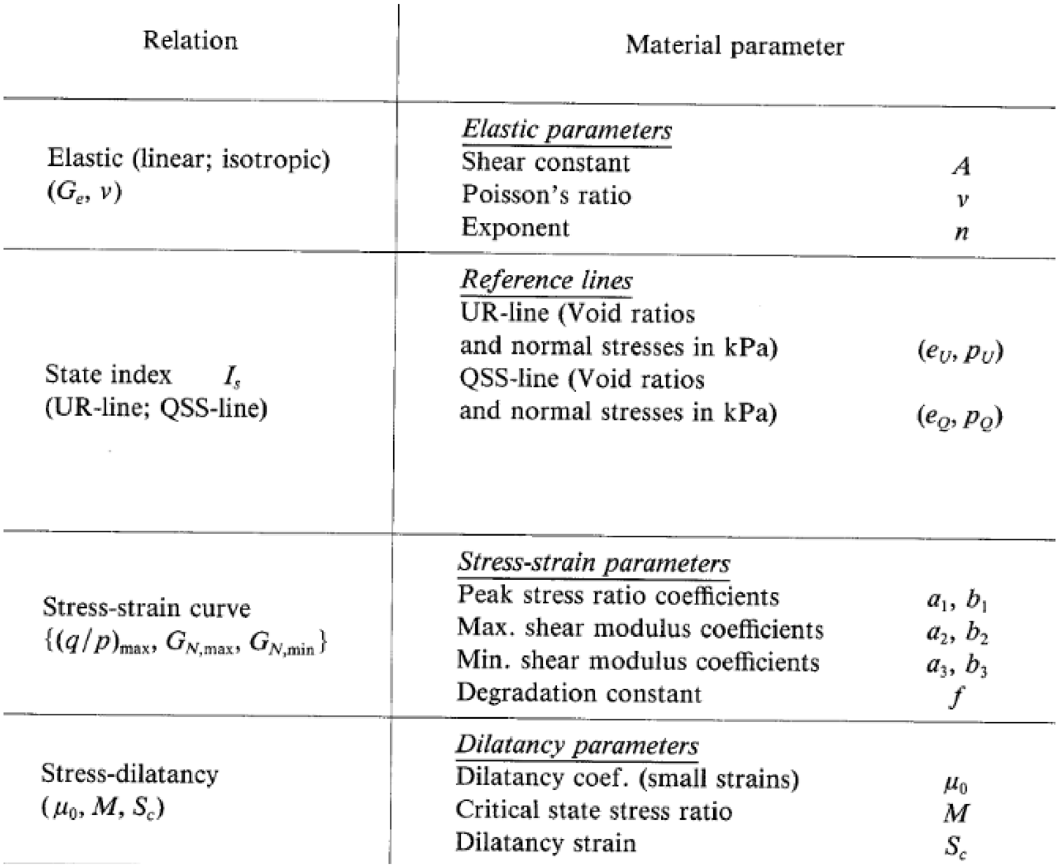

Relation	Material parameter	
Elastic (linear; isotropic) (G_e, ν)	*Elastic parameters*	
	Shear constant	A
	Poisson's ratio	ν
	Exponent	n
State index I_s (UR-line; QSS-line)	*Reference lines*	
	UR-line (Void ratios and normal stresses in kPa)	(e_U, p_U)
	QSS-line (Void ratios and normal stresses in kPa)	(e_Q, p_Q)
Stress-strain curve $\{(q/p)_{\max}, G_{N,\max}, G_{N,\min}\}$	*Stress-strain parameters*	
	Peak stress ratio coefficients	a_1, b_1
	Max. shear modulus coefficients	a_2, b_2
	Min. shear modulus coefficients	a_3, b_3
	Degradation constant	f
Stress-dilatancy (μ_0, M, S_c)	*Dilatancy parameters*	
	Dilatancy coef. (small strains)	μ_0
	Critical state stress ratio	M
	Dilatancy strain	S_c

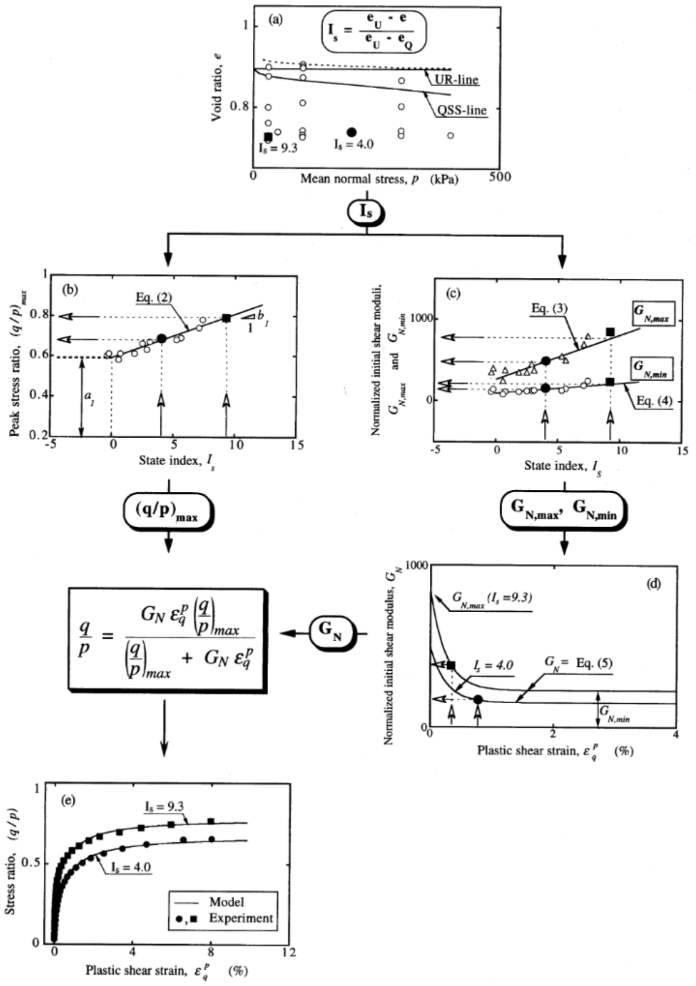

Figure 4-1 Modeling of p-constant normalized stress-strain curve for a given initial e-p' state for Stress-Density model (from Cubrinovski & Ishihara, 1998).

Pressure Dependent Model:

The University of California San Diego Pressure Dependent Model (UCSDSAND3, Khosravifar et al. 2018) is a 3D multi-surface elasto-plastic constitutive model that uses mixed stress and strain space yield domain to capture soil liquefaction and cyclic mobility with a non-associative flow rule to reproduce dilatancy effect. UCSDSAND3 reproduces liquefaction triggering and response, including dilatancy (shear-induced volume contraction or dilation) and non-flow liquefaction (cyclic mobility). The model features a yield function that defines the failure envelope, a hardening rule that governs the translation of yield surfaces within this envelope, and a novel flow rule that incorporates a phase transformation (PT) surface to describe dilation and contraction tendencies of soil under cyclic loading conditions (Elgamal et al., 2002).

Key parameters in the UCSDSAND3 model include standard dynamic soil properties such as the low-strain shear modulus and friction angle. Additional parameters account for dilatancy effects and liquefaction-induced yield strain, enabling the model to replicate behaviors like cyclic mobility and the post-liquefaction accumulation of shear strains. These parameters are typically calibrated through dynamic laboratory tests, such as cyclic triaxial and direct simple shear tests (Elgamal et al., 2002). Table 4.3 provides a summary of these parameters and the required calibration procedures.

Table 4.3 Calibration experiments for different parameters used in the pressure dependent model (from Elgamal et al., 2002)

Main calibration experiment	Parameter
Drained monotonic tests	Low-strain shear modulus G_r (at 80 kPa mean effective confinement) Friction angle ϕ
Undrained cyclic test	Liquefaction yield strain γ_y (Fig. 4, phase 1–2)
RPI centrifuge Model 1	Contraction parameter c_1 Contraction parameter c_2 (Fig. 4, phase 0–1)
RPI centrifuge Model 2	Phase transformation angle ϕ_{PT} Dilation parameter d_1 Dilation parameter d_2 (Fig. 4, phase 2–3)

While the model is helpful in capturing the development of large shear strains at minimal stress changes, making it highly effective for non-flow liquefaction scenarios, it has some limitations. For instance, it is difficult at times to accurately predict the number of loading cycles required to trigger liquefaction under varying cyclic shear stress ratios (CSR) (Khosravifar et al., 2022). Moreover, its performance in boundary value problems might not always provide accurate soil responses when flow liquefaction occurs (Elbadawy et al., 2022).

SANISAND:

The SANISAND model is an elasto-plastic, stress-ratio controlled, and critical state compatible framework based on the concept of rotational hardening. It incorporates three main features: (1) a fabric-dilatancy-related quantity, (2) the dependence of the plastic strain rate direction on a modified Lode angle in the multiaxial generalization, and (3) a consistent connection between the triaxial and general multiaxial formulations. A fabric-dilatancy-related tensor was introduced in the updated version of the model to account for the microscopically observed changes in sand fabric during plastic dilation and their influence on the contractive response upon reversal of the loading direction (Dafalias & Manzari, 2004).

The model constants are shown in Table 4.4, and the triaxial and corresponding multiaxial constitutive equations are shown in Table 4.5. One of the key advantages of the SANISAND model is its applicability to a wide range of pressures and densities. However, the SANISAND model has limitations in its ability to approximate engineering design relationships commonly used to estimate stress-strain behaviors crucial for predicting liquefaction-induced ground deformations during earthquakes. Refer to Dafalias & Manzari (2004) for more information about the SANISAND model.

Table 4.4 SANISAND model constants (from Dafalias & Manzari, 2004).

Constant	Variable	Value
Elasticity	G_0	125
	ν	0.05
Critical state	M	1.25
	c	0.712
	λ_c	0.019
	e_0	0.934
	ξ	0.7
Yield surface	m	0.01
Plastic modulus	h_0	7.05
	c_h	0.968
	n^b	1.1
Dilatancy	A_0	0.704
	n^d	3.5
Fabric-dilatancy tensor	$z_{\max}$	4
	c_z	600

Table 4.5 Triaxial and corresponding multiaxial constitutive equations with associated model constants (from Dafalias & Manzari, 2004).

Triaxial equations	Multiaxial equations	Constants
Critical state line		
—	$e_c = e_0 - \lambda_c (p_c/p_{at})^{\xi}$	$e_0,\ \lambda_c,\ \xi$
Elastic deviatoric strain increment		
$d\varepsilon_q^e = dq/3G$	$d\mathbf{e}^e = d\mathbf{s}/2G$	—
—	$G = G_0 p_{at}[(2.97-e)^2/(1+e)](p/p_{at})^{1/2}$	G_0
Elastic volumetric strain increment		
—	$d\varepsilon_v^e = dp/K$	
	$K = 2(1+\nu)G/3(1-2\nu)$	ν
Yield surface		
$f = \lvert\eta - \alpha\rvert - m = 0$	$f = [(\mathbf{s}-p\boldsymbol{\alpha}):(\mathbf{s}-p\boldsymbol{\alpha})]^{1/2} - \sqrt{2/3}pm = 0$	m
Plastic deviatoric strain increment		
$d\varepsilon_q^p = d\eta/H$	$d\mathbf{e}^p = \langle L\rangle \mathbf{R}'$	
$H = h(M^b - \eta)$	$K_p = (2/3)ph(\boldsymbol{\alpha}_\theta^b - \boldsymbol{\alpha}):\mathbf{n}$	
$M^b = M\exp(-n^b\Psi)$	$\boldsymbol{\alpha}_\theta^b = \sqrt{2/3}[g(\theta,c)M\exp(-n^b\Psi) - m]\mathbf{n}$	$M,\ c,\ n^b$
$h = b_0/\lvert\eta - \eta_{in}\rvert$	$h = b_0/(\boldsymbol{\alpha} - \boldsymbol{\alpha}_{in}):\mathbf{n}$	
—	$b_0 = G_0 h_0 (1 - c_h e)(p/p_{at})^{-1/2}$	$h_0,\ c_h$
Plastic volumetric strain increment		
$d\varepsilon_v^p = d\lvert\varepsilon_q^p\rvert$	$d\varepsilon_v^p = \langle L\rangle D$	
$d = A_d(M^d - \eta)$	$D = A_d(\boldsymbol{\alpha}_\theta^d - \boldsymbol{\alpha}):\mathbf{n}$	
$M^d = M\exp(n^d\Psi)$	$\boldsymbol{\alpha}_\theta^d = \sqrt{2/3}[g(\theta,c)M\exp(n^d\Psi) - m]\mathbf{n}$	n^d
$A_d = A_0(1 + \langle sz\rangle)$	$A_d = A_0(1 + \langle \mathbf{z}:\mathbf{n}\rangle)$	A_0
Fabric-dilatancy tensor update		
$dz = -c_z\langle -d\varepsilon_v^p\rangle(sz_{\max} + z)$	$d\mathbf{z} = -c_z\langle -d\varepsilon_v^p\rangle(z_{\max}\mathbf{n} + \mathbf{z})$	$c_z,\ z_{\max}$
Back-stress ratio tensor update		
$d\alpha = d\eta$	$d\boldsymbol{\alpha} = \langle L\rangle(2/3)h(\boldsymbol{\alpha}_\theta^b - \boldsymbol{\alpha})$	

PM4SAND:

The constitutive model PM4SAND is a stress-ratio controlled, critical state compatible, bounding surface sand plasticity model developed within the framework established by Manzari and Dafalias (2004) for the SANISAND model. PM4Sand introduces modifications to the SANISAND framework to enhance its ability: 1) to approximate stress-strain responses important to geotechnical earthquake engineering applications, based on trends derived from experimentally and case-history-based design correlations, and 2) to be calibrated within a reasonable amount of engineering effort (Boulanger & Ziotopoulou, PM4SAND (VERSION 3.2): A Sand Plasticity Model for Earthquake Engineering Applications, 2022). Current versions of PM4SAND include a 2D plane strain model, with a 3D version under development.

There are three primary input parameters used in PM4SAND: the apparent relative density D_R, the shear modulus coefficient G_o, and the contraction rate parameter h_{po}. D_R can be estimated using either correlations to the overburden-corrected SPT blow count ($(N_1)_{60}$), or overburden-corrected Cone Penetration Test (CPT) tip resistance (q_{c1N}) using Equations 1 and 2, respectively.

$$D_R = \sqrt{\frac{(N_1)_{60}}{C_d}} \tag{1}$$

$$D_R = 0.465 \left(\frac{q_{c1N}}{C_{dq}}\right)^{0.264} - 1.063 \tag{2}$$

where $C_d = 46$ and $C_{dq} = 0.9$. Note that the input value of D_R is the apparent relative density and is different from the values conventionally obtained from the laboratory results. Unlike the strict measurement of relative density in laboratory settings, the apparent relative density is treated as an adjustable input parameter. Its value influences the model's response and can be adjusted upward or downward to improve the calibration of the model to align with other relationships or data (Boulanger & Ziotopoulou, PM4SAND (VERSION 3.2): A Sand Plasticity Model for Earthquake Engineering Applications, 2022).

The second primary input parameter is the constant G_o which controls the elastic (small-strain) shear modulus and can be estimated either using the SPT $(N_1)_{60}$, as shown in Equation 3, or using the shear wave velocity (V_s) measurements to correlate with the small strain shear modulus (G_{max}) and subsequently estimate G_0 (Equation 4 and 5).

$$G_o = 167\sqrt{(N_1)_{60} + 2.5} \tag{3}$$

$$G = \rho\,(V_s)^2 \tag{4}$$

$$G = G_0 p_a (\frac{p}{p_a})^{\frac{1}{2}} \tag{5}$$

where p_a is atmospheric pressure, which is 101.3 kPa.

The third parameter, h_{po}, is determined using element tests with the PM4SAND model in FLAC to estimate the cyclic resistance ratio (CRR) at 15 cycles, e.g., as per the Boulanger and Idriss (2014) simplified liquefaction triggering procedure.

There are 18 secondary parameters that can be adjusted depending on the project but are commonly left as the default values. These parameters include: R and Q, which define the critical-state line in D_R -p' space; n_b and n_d, which control peak friction angle and "phase transformation" stress ratio, respectively; critical-state or constant-volume friction angle (φ_{cv}), maximum and minimum void ratios (e_{max}, e_{min}), poison's ratio, and other parameters. For more information on these parameters, refer to Boulanger and Ziotopoulou (2022).

The model defines the critical state in the D_R-p' space using the concept of relative state parameter index (ξ_R), shown in Equations 6 and 7 below, where D_R is the relative density at the current state and $D_{R,cs}$ is the relative density at the critical state. The soil's tendency to dilate or contract during shearing is characterized using ξ_R, which governs the generation of positive or negative pore pressure in undrained conditions.

$$\xi_R = D_{R,cs} - D_R \tag{6}$$

$$D_{R,cs} = \frac{R}{Q - \ln\left(100 \frac{p'}{p_a}\right)} \tag{7}$$

where *R* and *Q* are empirical correlations used to define the dilation behavior of sands under shear. Boulanger and Ziotopoulou (2022) recommend a baseline value of 1.5 for *R* and 10 for *Q* in Equation 7.

The model includes bounding (M_b), dilation (M_d) and critical state surfaces (M_c) and they are related to each other based on equations below:

$$M_b = M_c \exp\left(-n^b \, \xi_R\right) \tag{8}$$

$$M_d = M_c \exp\left(n^d \, \xi_R\right) \tag{9}$$

$$M_c = 2\sin(\varphi_{cv}) \tag{10}$$

where n^b and n^d are parameters defining M_b and M_c and φ_{cv} is the critical state (constant volume) friction angle, which is an input parameter. For stress ratios below M_d (dilation surface), the soil exhibits contractive behavior until it reaches M_d, at which point dilation begins. Under static loading, dense soil has a higher bounding surface (M_b) than the critical state ratio, resulting in a peak friction angle followed by strain softening to reach the critical state friction angle. In contrast, loose soil has a bounding surface closer to the critical state, resulting in contractive response with a peak friction angle similar to the critical state friction angle.

The model's yield surface is defined as a cone in *q-p'* space, where the center of cone is defined by the back-stress ratio tensor and the diameter of the cone is defined by a parameter "*m*". The fabric-dilatancy tensor adapted from Dafalias and Manzari (2004) has been modified to depend on plastic deviatoric strains instead of plastic volumetric strains (Boulanger & Ziotopoulou, PM4SAND (VERSION 3.2): A Sand Plasticity Model for Earthquake Engineering Applications, 2022).

The secondary parameters can be calibrated using laboratory and field test results. The critical state line (CSL) is derived from isotopically consolidated drained and undrained triaxial tests (CID and CIU) or direct simple shear tests (DSS). φ_{cv} can be obtained by analyzing monotonic drained and undrained triaxial tests (Luque, 2017). As mentioned, D_R is best correlated with the relationships shown in Equations 1 and 2, while G_0 can be estimated using shear wave velocity measurements or SPT measurements, following the correlations presented in Equations 3 through 5 (Boulanger & Ziotopoulou, 2022).

While PM4SAND is effective for numerous applications in earthquake engineering, it has certain limitations. The current implementation only supports 2D plane strain analyses and does not consider stress effects in situations where plane strain conditions may not hold. Furthermore, the model does not incorporate a cap for isotropic hardening and fails to fully account for anisotropic fabric effects and their changes over time. It also struggles with accurately modeling scenarios involving flow liquefaction as do most liquefaction constitutive models. Nonetheless, PM4SAND is generally easy to calibrate and can provide acceptable approximations of soil behavior in many contexts, which enhances its utility in specific geotechnical earthquake engineering applications.

An example of the responses provided by PM4SAND is demonstrated in Figures 4-2 to 4-4. Figure 4-2 shows the undrained responses to cyclic DSS loading for D_R=35%, representing loose soil, and D_R=75%, representing dense soil, under the same vertical effective consolidation stress of 100 kPa. As shown, the number of cycles to failure for D_R=35% is significantly lower than for the denser soil. Additionally, the maximum shear stress ratio experienced by the D_R=75% soil is approximately three times greater than that of the loose soil.

Figure 4-3 illustrates the undrained cyclic stress ratio (CSR) versus the number of uniform cycles under DSS cyclic loading for three relative densities: 35%, 55%, and 75%. It can be observed that as the relative density increases, the number of cycles to a given CSR also increases. These responses align with the expected behavior of soils with varying relative densities (Boulanger & Ziotopoulou, 2022).

Figure 4-4 demonstrates the responses of soils with D_R=35% and D_R=75% under monotonic DSS loading for different vertical effective consolidation stresses. As observed, soils under higher consolidation stresses exhibit more dilative behavior compared to those under lower effective consolidation stresses, for both D_R=35 and D_R=75%. In both cases, the soil initially shows contraction before transitioning to dilative behavior, with the denser soil (D_R=75%) experiencing less contraction than the loose soil (D_R=35%). These observations are consistent with expected soil behavior, demonstrating how PM4SAND can provide reasonable responses in earthquake engineering applications (Boulanger & Ziotopoulou, PM4SAND (VERSION 3.2): A Sand Plasticity Model for Earthquake Engineering Applications, 2022).

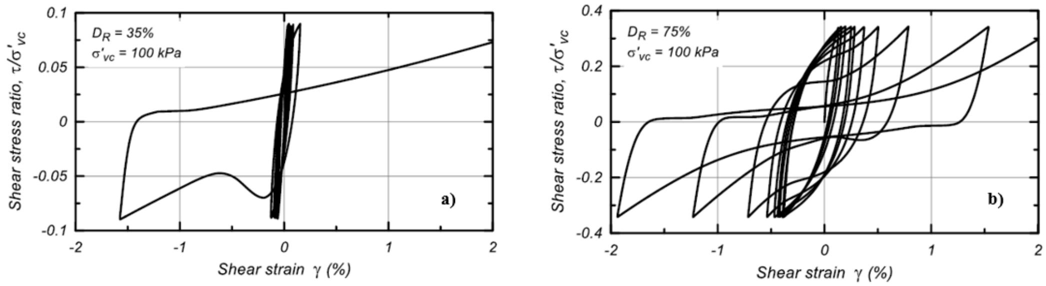

Figure 2-2 Example of undrained cyclic DSS loading responses using PM4SAND for (a) D_R=35% (loose sand) and (b) D_R=75% (dense sand) with a vertical effective consolidation stress of 100 kPa without initial static shear stress (from Boulanger & Ziotopoulou, 2022).

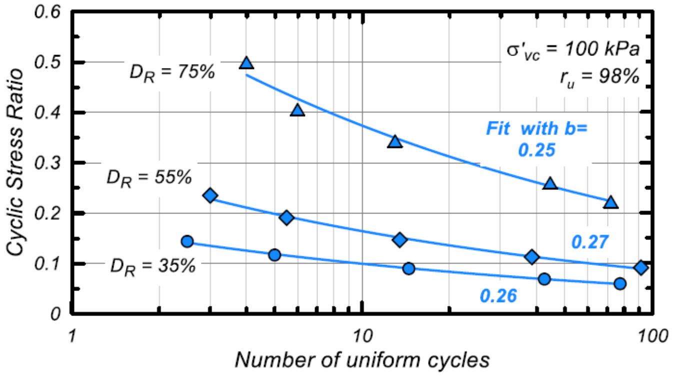

Figure 4-3 Example response of Cyclic Stress Ratio (CSR) versus number of equivalent uniform loading cycles in undrained DSS to cause r_u=98% for D_R= 35%, 55%, and 75% with a vertical effective consolidation stress of 100 kPa in PM4SAND. Each set of CSR-N simulations was fit with a power relationship with b-values labeled in the graph (from Boulanger and Ziotopoulou, 2022).

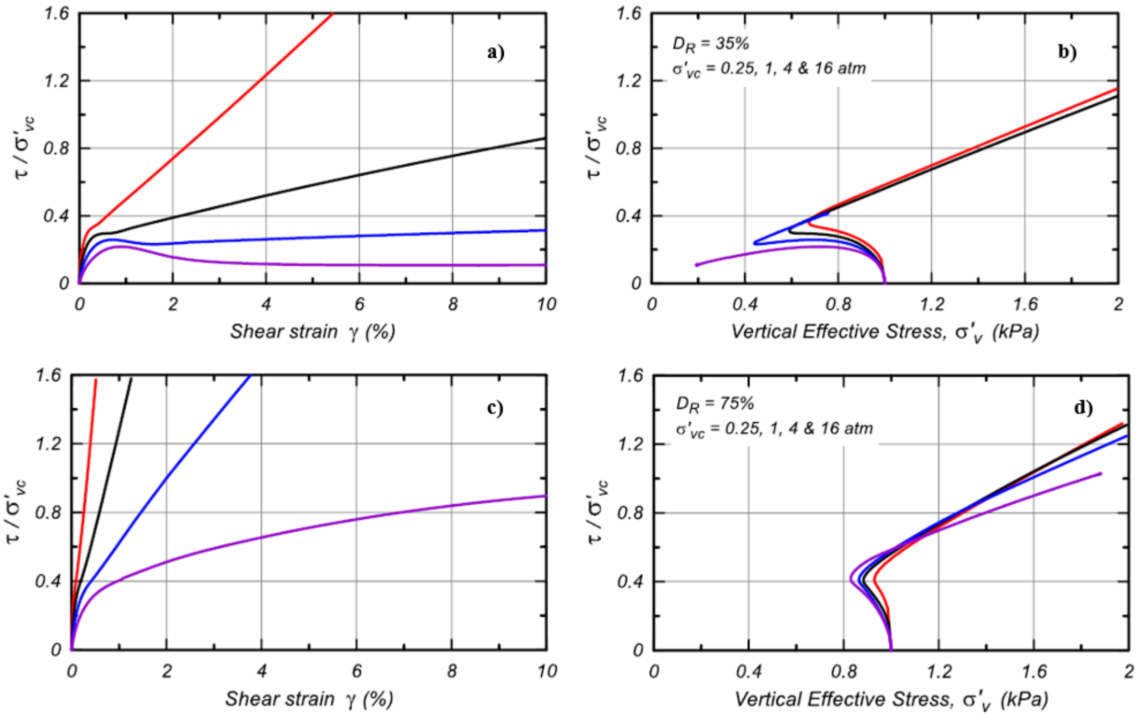

Figure 4-4 Example normalized responses in PM4SAND: (a) Shear stress normalized by vertical effective consolidation stress vs shear strain for D_R=35% under vertical effective consolidation stresses of 1/4, 1, 4, and 16 atm; (b) Shear stress normalized by vertical effective consolidation stress vs vertical effective stress for D_R=35% under vertical effective consolidation stresses mentioned in (a); (c) Shear stress normalized by vertical effective consolidation stress vs shear strain for D_R=75% under vertical effective consolidation stresses mentioned in (a); (d) Shear stress normalized by vertical effective consolidation stress vs vertical effective stress for D_R=75% under vertical effective consolidation stresses mentioned in (a) (from Boulanger & Ziotopoulou, 2022).

PM4Silt:

PM4Silt is a stress-ratio controlled, critical state-based, bounding surface plasticity model for clays and plastic silts, developed following the framework of PM4SAND. This model extends the capabilities of PM4Sand to approximate the undrained monotonic and cyclic loading responses of clay and plastic silt, as opposed to sand and nonplastic silt (Boulanger & Ziotopoulou, 2018). The model features four primary input parameters: undrained shear strength at critical state ($s_{u,cs}$) or undrained shear strength ratio at critical state ($s_{u,cs}/\sigma'_{vc}$), shear modulus coefficient (G_o), contraction rate parameter (h_{po}), and post-strong-shaking shear strength reduction factor (F_{su}). The specified value of $s_{u,cs}$ value controls the location of the critical state line during model initialization, contingent on the other input parameters.

The second input parameter, G_o, is similar to the PM4SAND model and should be selected to match G_{max} corresponding to the measured or estimated V_s. Equation 11 provides the correlation between G_{max} and G_o, where the exponent n_G has a default value of 0.75 but may be adjusted for calibration. Here, p_a is the atmospheric pressure and is 101.3 kPa (Boulanger & Ziotopoulou, 2018).

$$G_{max} = G_o p_a (\frac{p}{p_a})^{n_G} \tag{11}$$

The third primary input parameter, h_{po}, is calibrated using the same procedure described in the PM4SAND section. Lastly, F_{su} is used to reduce the $s_{u,cs}$ value relative to its value at initialization. This parameter can be used to evaluate post-strong-shaking static stability by incorporating appropriate strengths for slower loading rates and accounting for cyclic degradation or remolding effects. The value for this parameter should be selected based on the soil characteristics and the shear strains that develop during strong shaking (Boulanger & Ziotopoulou, 2018).

The model includes 20 secondary parameters that can be adjusted to reflect site-specific soil responses, based on laboratory testing. Table 4.6 summarizes the primary and secondary parameters along with their default values. According to Boulanger and Ziotopoulou (2018), parameters such as h_o, $n^{b,wet}$, z_{max}, C_e, and C_z have been shown to significantly improve site-specific calibrations, while parameters such as $r_{up,max}$, C_{DG}, and $C_{k\alpha}$ can also be effective in some cases.

Table 4.6 Input parameters for PM4Silt (from Boulanger & Wijewickreme, 2019).

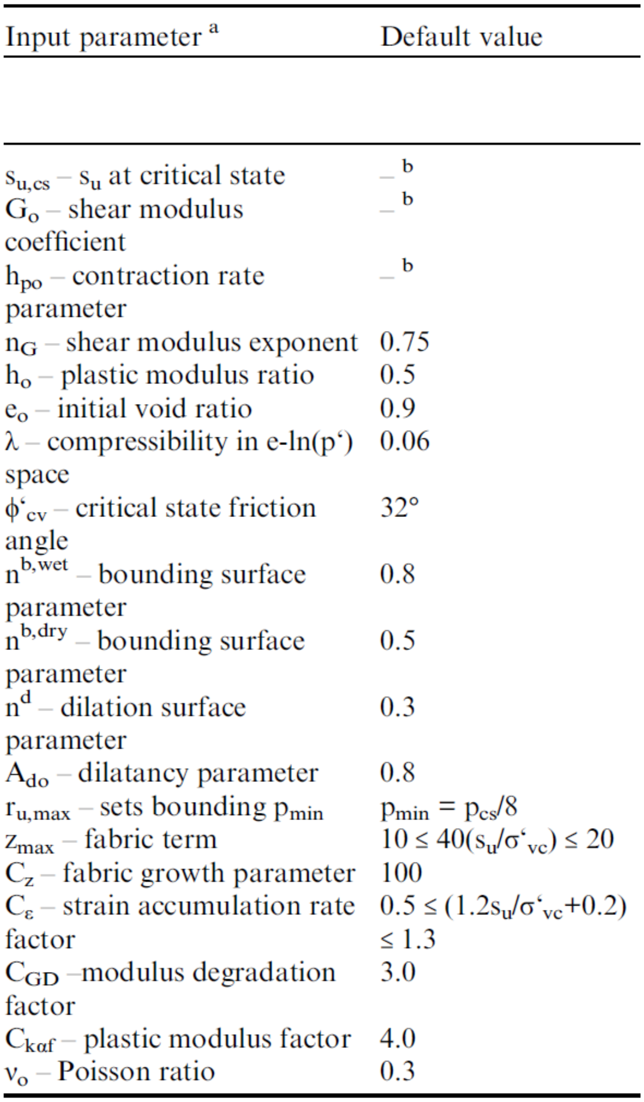

Input parameter [a]	Default value
$s_{u,cs}$ – s_u at critical state	– [b]
G_o – shear modulus coefficient	– [b]
h_{po} – contraction rate parameter	– [b]
n_G – shear modulus exponent	0.75
h_o – plastic modulus ratio	0.5
e_o – initial void ratio	0.9
λ – compressibility in e-ln(p‘) space	0.06
ϕ'_{cv} – critical state friction angle	32°
$n^{b,wet}$ – bounding surface parameter	0.8
$n^{b,dry}$ – bounding surface parameter	0.5
n^d – dilation surface parameter	0.3
A_{do} – dilatancy parameter	0.8
$r_{u,max}$ – sets bounding p_{min}	$p_{min} = p_{cs}/8$
z_{max} – fabric term	$10 \le 40(s_u/\sigma'_{vc}) \le 20$
C_z – fabric growth parameter	100
C_ε – strain accumulation rate factor	$0.5 \le (1.2s_u/\sigma'_{vc}+0.2) \le 1.3$
C_{GD} –modulus degradation factor	3.0
$C_{k\alpha f}$ – plastic modulus factor	4.0
ν_o – Poisson ratio	0.3

Similar to PM4SAND, PM4Silt defines the critical state line (CSL) using the concept of state parameter (ξ) (Equation 12). However, the CSL is represented in the void ratio (e) vs natural logarithm of mean effective stress (ln(p')) space, with a slope λ and intercept e_{1kPa} when $p' = 1$ kPa (Equation 13).

$$\xi = \mathrm{e} - e_{cs} \tag{12}$$

$$e_{cs} = e_{1kPa} - \lambda \ \ln\left(\frac{p}{1\ kPa}\right) \tag{13}$$

For clay and moderately plastic to highly plastic silt, the slope of the CSL, λ can be approximated using the slope of the virgin consolidation line (C_c) as shown in Equation 14 below:

$$\lambda = 0.434\ C_c \tag{14}$$

The model incorporates bounding, dilatancy, and critical stress ratio surfaces, similar to PM4Sand, with the yield function defined as a cone in stress space. Refer to Boulanger & Ziotopoulou (2018) for additional details.

Calibration process for PM4Silt is iterative similar to the PM4Sand. The process can be summarized as follows (Boulanger & Wijewickreme, 2019):

1. Select a value for $s_{u,cs}/\sigma'_{vc}$ that describes the variation of s_u with depth;
2. Select values for secondary parameters e_o, λ, and φ_{cv} based on the available laboratory test data;
3. Select values for G_o and secondary parameters n_G that describe the variation of V_s with depth;
4. Assign a trial value to h_{po} to start the iterative process:
5. Simulate monotonic undrained DSS loading and use $n^{b,wet}$ to adjust the peak s_u if the soil is initially wet of critical (loose);
6. Simulate cyclic undrained DSS loading at different strain amplitudes and use h_o to adject the dependence of secant shear moduli and equivalent damping ratios on cyclic shear strain amplitudes;
7. Simulate cyclic undrained DSS loading with uniform cyclic stress ratios and use h_{po} to adjust the fit to the cyclic DSS laboratory test results for CRR vs number of cycles to cause a peak shear strain of 3%;
8. Examine the stress-strain and stress-path responses from the simulations and use the secondary parameters C_e, C_z, C_{DG}, $r_{u,max}$ and n_G to adjust the shear strain accumulation rate and other feature behaviors;
9. Repeat steps [5] to [8] until no revisions to parameters are required.

Despite its effectiveness in many earthquake engineering applications, PM4Silt has some limitations. It lacks the ability to model consolidation settlements or capture strength evolution with consolidation stress history due to the absence of a cap. Additionally, it is not formulated to approximate anisotropic strengths and is restricted to plane strain applications (Boulanger & Ziotopoulou, 2018). However, the model provides reasonable approximations of soil responses relevant to many practical cases and is relatively straightforward to calibrate, making it a valuable tool for specific geotechnical earthquake engineering analyses.

An example of the responses provided by PM4Silt is illustrated in Figures 4-5 to 4-7. Figure 4-5 compares PM4Silt simulation results with measured responses under monotonic undrained DSS loading for high PI and low PI soils. The measured and simulated shear strengths at the critical state are consistent for both soils. For the high PI soil (PI=20), the simulated stress-strain response is initially much stiffer than the test results. This discrepancy arises from the decision to base G_o and the target G/G_{max} behavior on empirical correlations rather than matching the laboratory data, as measured DSS responses often underestimate the true small-strain stiffness (Boulanger & Ziotopoulou, 2018). However, the response at lower shear strains can be aligned with laboratory results by adjusting the model parameters. A similar trend is observed for the low PI soil (PI=6). This example highlights PM4Silt's capability to accurately capture responses in monotonic tests for a range of soils with varying plasticity indices.

Figures 4-6 and 4-7 present the stress-strain and stress-path responses, respectively, for PI=6 and PI=20 soils under undrained cyclic DSS loading. In both cases, the rates of shear strain accumulation align well with laboratory DSS measurements. Additionally, the shape of the hysteresis loops closely matches the observed data (Boulanger & Ziotopoulou, 2018). These results further demonstrate PM4Silt's ability to replicate responses for soils with differing characteristics under cyclic loading, underscoring its applicability to a variety of earthquake engineering problems.

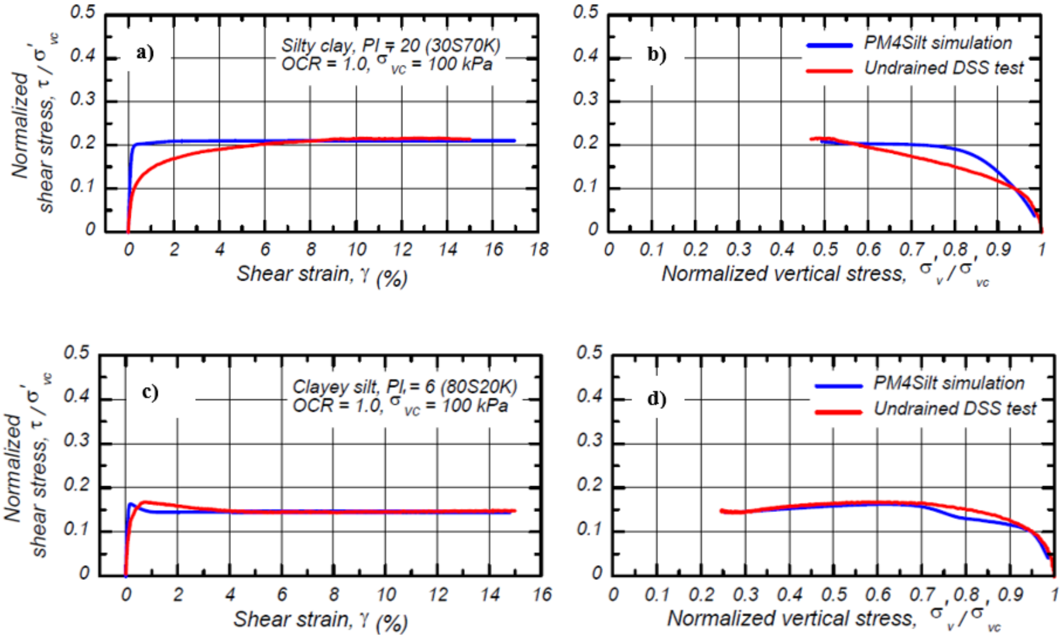

Figure 4-5 Measured and simulated responses in monotonic undrained DSS loading for: (a) and (b) PI=20 silty clay and (c) and (d) PI=6 clayey silt (from Boulanger & Ziotopoulou, 2018).

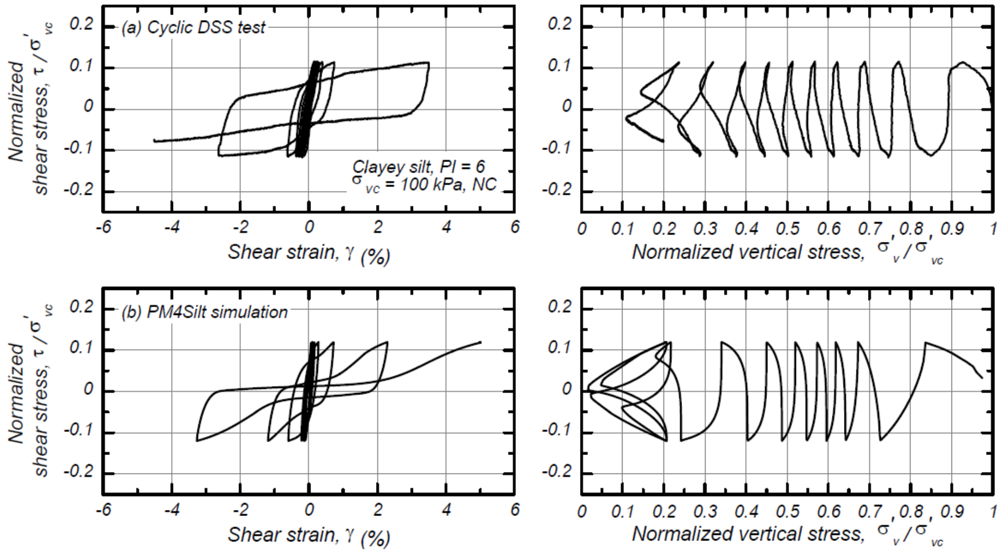

Figure 4-6 Stress-strain and stress path responses in undrained cyclic DSS loading at a relative high loading for PI=6 clayey silt (from Boulanger & Ziotopoulou, 2018).

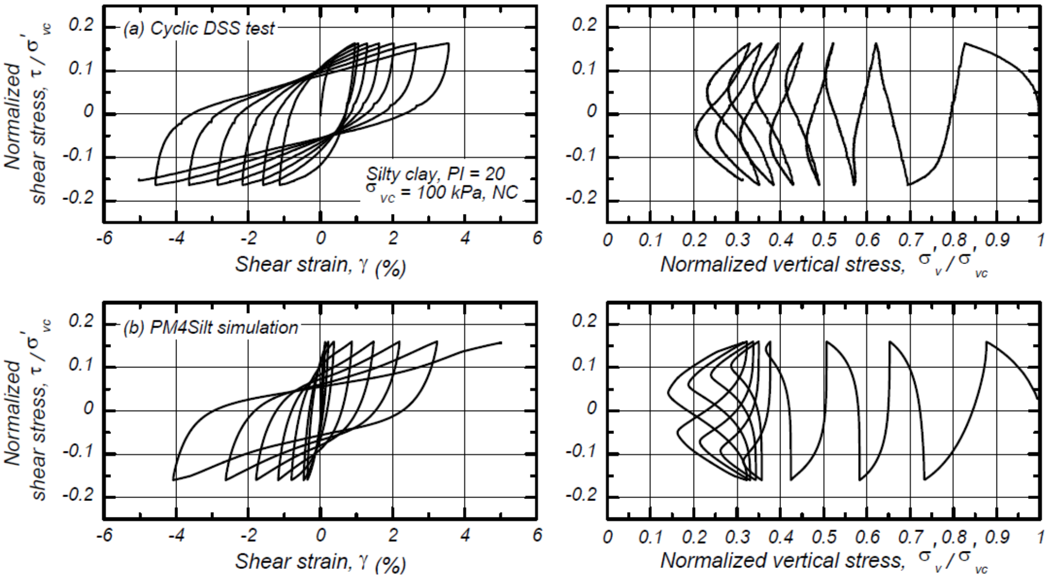

Figure 4-7 Stress-strain and stress path responses in undrained cyclic DSS loading at a relative high loading for PI=20 silty clay (from Boulanger & Ziotopoulou, 2018).

4.3 Overview of Previous Numerical Modeling Studies

Numerous studies have focused on identifying mechanisms and parameters that influence the seismic response of buildings with shallow foundations affected by liquefied soil. This review of previous studies of numerical analysis of shallow-founded structures atop liquefiable soil focuses on recent studies that provide insights into the seismic performance of shallow bridge foundations.

Dashti and Bray (2013) performed a series of nonlinear effective stress dynamic back-analysis of geotechnical centrifuge experiments using FLAC2D with the UBCSAND constitutive model. They studied the important parameters contributing to the results observed in their centrifuge tests on shallow building foundations. Bray and Dashti (2014) expanded this study by summarizing observations from field case histories and the numerical analyses. They concluded that when the liquefiable layer is shallow, shear-induced deformations dominate as buildings push into liquefied soil under cyclic loading.

SSI-induced foundation ratcheting deformation ($\varepsilon_{q\text{-}SSI}$) and partial bearing failure due to strength loss-induced bearing capacity deformation ($\varepsilon_{q\text{-}BC}$) largely govern the building movement during earthquake strong shaking. Localized volumetric strains from partial drainage ($\varepsilon_{p\text{-}DR}$), and removal of soils from underneath foundations due to the formation of sand ejecta are also important. However, since the liquefaction-induced building settlements in cases with thin, shallow deposits of saturated granular soils are governed by shear strains, the thickness of the liquefiable layer is not directly proportional to the settlement as would be suggested if it were governed by volumetric strains as indicated in the studies of Liu and Dobry (1997). If the ratio of excess pore water pressure to the effective stress (r_u) nearly reaches 1, the sedimentation after liquefication ($\varepsilon_{p\text{-}SED}$) also contributes to the failure.

Examples of these mechanisms are evident in the results from numerical modeling of the centrifuge experiments in FLAC2D. Figure 4-8 illustrates the contours of localized volumetric strains that developed along the edges of the structure during Experiment T3-50 under the large Port Island (P.I.) event. These observations are consistent with those recorded during the centrifuge experiments, validating the numerical model's ability to replicate the physical phenomena.

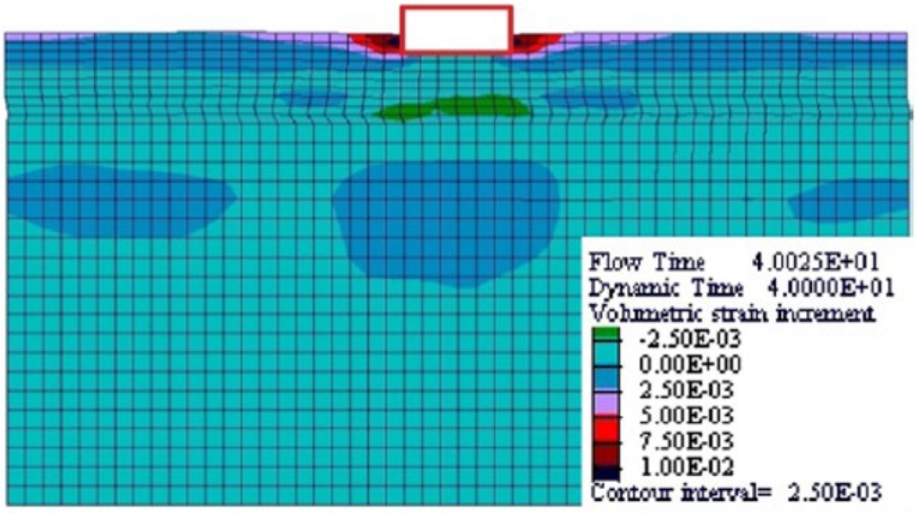

Figure 4-8 FLAC2D simulations of structure BL in experiment T3-50 during the large Port Island event: contours of accumulated volumetric strain (from Bray & Dashti, 2014).

Figure 4-9 compares the simulated and measured responses from Experiment T3-50 under moderate P.I. motion. As shown in Figure 4-9a, both the centrifuge experiment and numerical simulations reveal that the structure began settling after one significant cycle of loading. The settlement rate was approximately linear with time during the shaking phase, and it reduced dramatically once the strong shaking subsided (around 20 seconds). This indicates that post-liquefaction reconsolidation settlements did not significantly contribute to the total settlement in this scenario. Instead, other mechanisms, such as localized volumetric and deviatoric strains, were responsible (Dashti & Bray, 2013).

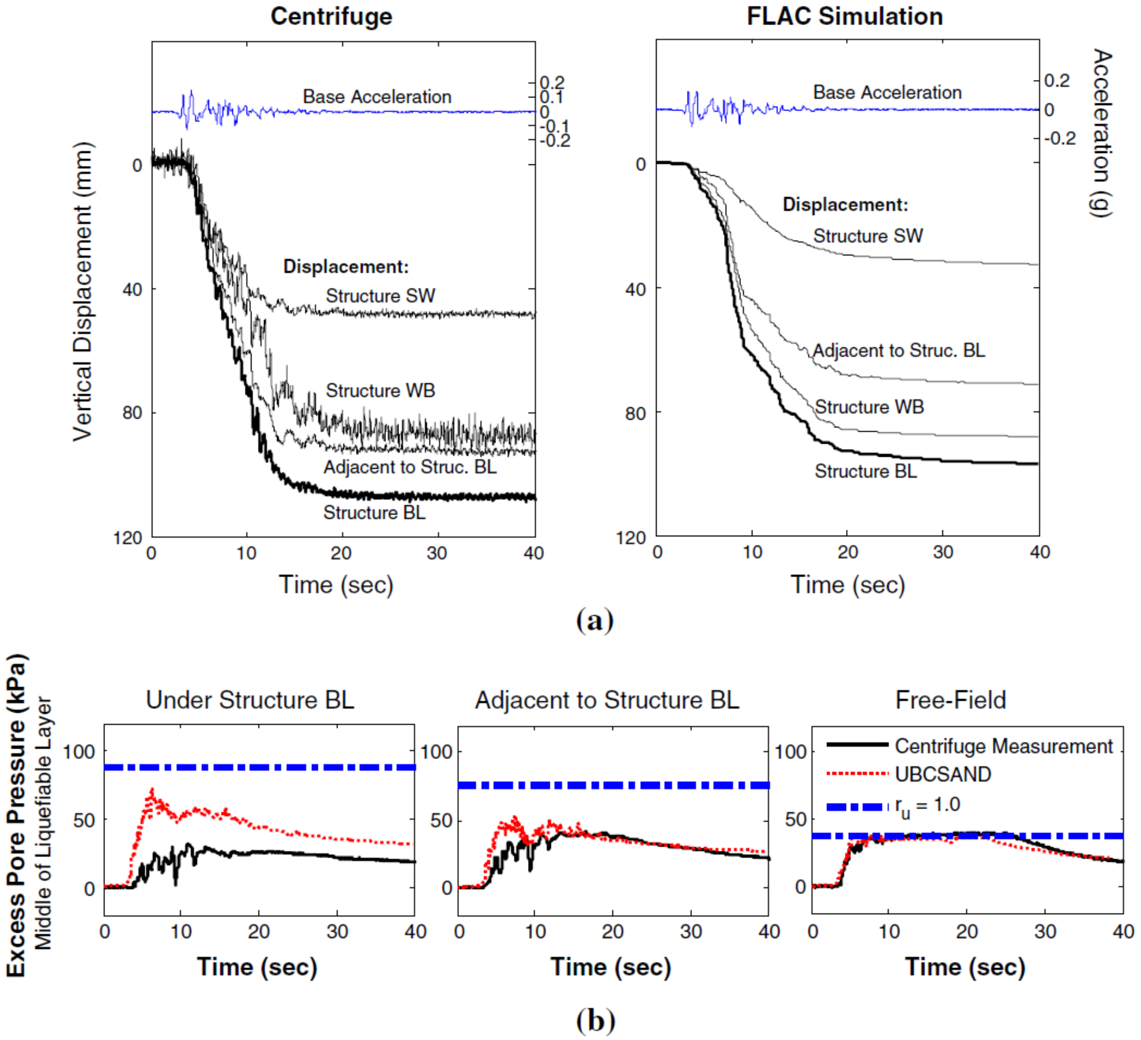

Figure 4-9 Comparison of simulated and measured response in T3-50, moderate P.I. motion: (a) displacement near structures BL, SW, and WB; (b) excess pore water pressure (Dashti & Bray 2013).

Figure 4-9b presents the excess pore pressure beneath and adjacent to the structure and in the free-field. The numerical simulation slightly overestimated the excess pore pressure under the structure compared to the measured values but showed good agreement for other locations. In both the experiment and simulations, excess pore pressure remained high and oscillated throughout the strong shaking phase. Post-shaking, the excess pore pressure rapidly dissipated under the structure, as no significant additional pore pressure was generated. This behavior highlights the significant role of water dissipation in governing settlement patterns (Dashti & Bray, Numerical Simulations of Building Response on Liquefiable Sand, 2013).

Dashti and Bray (2013) note that the relative importance of each mechanism depends on the characteristics of the earthquake motion, liquefiable soil, and the building properties. In general, the initiation, rate, and the amount of liquefaction-induced building settlement depends on the shaking intensity rate (*SIR*) as defined in Chapter 3. Higher *SIR* values and lower D_R were associated with faster rates of building settlement and greater final building settlement.

Similar to other studies, Bray and Dashti (2014) concluded that the width and the contact pressure of the foundation are important parameters. Although free-field settlements are typically smaller than the liquefaction-induced foundation settlements, Bray and Dashti (2014), citing previous research by Ishii and Tokimatsu (1988), noted that if the width of the foundation is two or three times larger than the thickness of the liquefiable layer, the settlement of the structure is about equal to the settlement in the free-field. Therefore, the ratio between the thickness of the liquefiable layer and the foundation width is important (Bray & Dashti, 2014).

Bearing capacity degradation is another critical failure mechanism for shallow foundations, as it increases settlement and uneven settling of structures. Karamitros et al. (2013) showed that bearing capacity degradation persists throughout seismic excitation and continues until the excess pore water pressure dissipates. Their study found that a sufficiently thick and shear-resistant non-liquefiable soil crust, such as clay, dense or dry gravel, or improved soil, can reduce bearing capacity degradation and settlement. Consequently, the site's stratigraphy and the location of the liquefiable layer play crucial roles in settlement outcomes.

Karimi et al. (2018) conducted an extensive, fully coupled, 3D nonlinear effective stress finite element parametric study to evaluate the sensitivity of foundation settlement to various parameters using the FEM software OpenSEES (McKenna, Fenves, & Scott, 2000) and the PDMY02 model (Khosravifar et al. 2018). Soil parameters such as D_R and thickness of the liquefiable layer and the depth to the liquefiable layer were found to be the most influential. Structural properties such as bearing pressure, dimensions, aspect ratio, and embedment depth were found to be most important (Karimi et al., 2018).

Their findings show that D_R values between 60% and 70% mark a transition from medium-dense to dense soils, with settlement decreasing significantly as D_R increased from 60% to 70%. The thickness of the top liquefiable layer was positively correlated with the building settlement. Building settlement was positively correlated with the thickness of the top liquefiable layer, while increasing the depth to the liquefiable layer enhanced soil resistance to strength loss and shear deformation due to greater confinement pressures. Additionally, the presence of a low-permeability layer over the liquefiable layer could increase building settlement by delaying pore water pressure dissipation, with the extent of impact depending on the intensity of the ground motion.

For structural factors, Karimi et al (2018) found that foundation contact pressure (q) increases building settlement until it eventually plateaus with the plateau level influenced by D_R of the soil and the shaking intensity. Building settlement sensitivity to q was higher for intense shaking and looser soils. An increase in building foundation area or width (B) reduced settlement at lower shaking intensities due to greater stress distribution, but at higher intensities, larger footings induced greater shear stresses and deformation. A higher length to width aspect ratio (L/B) of mat foundations reduced shear strains, flow potential, and building settlement. Embedment depth was negatively correlated with building settlement, as deeper embedment reduced movement. However, increasing structural height and inertial mass slightly increased settlement due to higher seismic moments and shear, contributing to foundation ratcheting (Karimi et al., 2018).

Macedo and Bray (2018) performed nonlinear dynamic SSI effective stress analyses in 2D plane strain in FLAC using the PM4Sand constitutive model. Their goal was to assess the effects of specific soil conditions, building configurations, and ground motion characteristics on the performance of shallow foundation buildings. They found that shear-induced deformation mechanisms dominate during strong shaking, while volumetric-induced mechanisms contribute more post-shaking. As with other studies, soil relative density, liquefiable layer thickness, and depth were found to be primary factors affecting failure. Building contact pressure was the most critical structural parameter, followed by foundation width. Ground motion intensity parameters that correlated best with the structure's settlements were found to be standardized cumulative absolute velocity (CAV_{dp}), Arias intensity (I_a), and 5% damped 1-second spectral acceleration (S_a1).

The authors found that building settlement is less sensitive to variations of the liquefiable layer's relative density when it is in the ranges of very loose to loose, or dense to very dense. However, building settlement reduction was most significant when the relative density of the liquefiable layer increased from 50% to 75% (medium density). Similarly, the liquefiable layer thickness was influential up to a point, beyond which further increases did not affect building settlement (Figure 4-10).

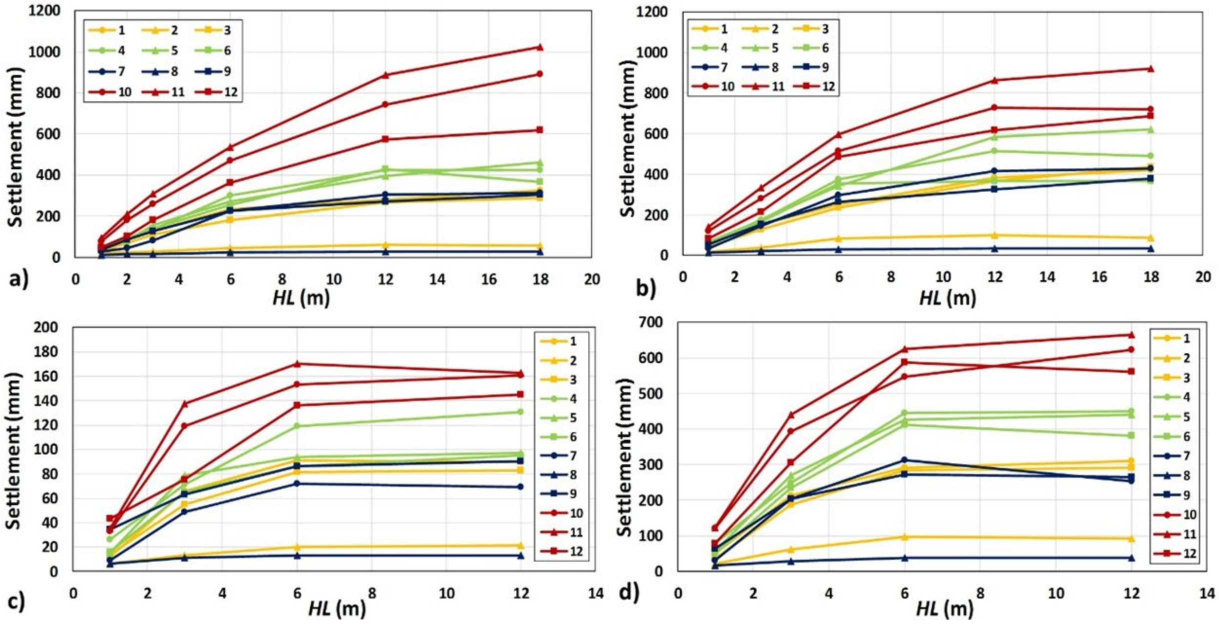

Figure 4-10 Building settlement vs thickness of the liquefiable layer for ground motions 1-12: (a) model with D_r=50%, bearing pressure (Q)=80 kPa, foundation width (B)=12 m, building height (H)=12 m, and non-liquefiable crust layer thickness (HC)=2 m; (b) model with Dr= 35%, Q=80 kPa, B=12 m, H=12 m and HC= 2m; (c) model with Dr=50%, Q=40 kPa, B=6 m, H= 6 m and HC=2 m; and (d) model with D_r= 35%, Q=80 kPa, B=6 m, H=12 m, and HC=2 m (from Macedo & Bray, 2018).

Building contact pressure was found to be an important structural factor, but the influence of it stops at some point where the magnitude of the liquefaction-induced settlement does not continue to increase (Figure 4-11). Building height was found to be correlated to the bearing pressure which captures most of the aspects of the building performance.

Other researchers have also examined ground motion intensity measures (*IMs*) for selecting and scaling motions to assess the seismic performance of structures founded on liquefiable soil deposits. Dashti and Karimi (2017) validated their extensive numerical parametric study against centrifuge results, using fully coupled 3D nonlinear finite element analyses with the PDMY02 model in OpenSees (Khosravifar, et al. 2018). Elastic SDOF structures on stiff mat foundations were modeled. Their findings suggested that the optimal *IM* for analysis depends on the choice of the engineering demand parameter (*EDP*) and modeling conditions. The peak excess pore pressure ratio ($r_{u,peak}$) was the *EDP* in this study.

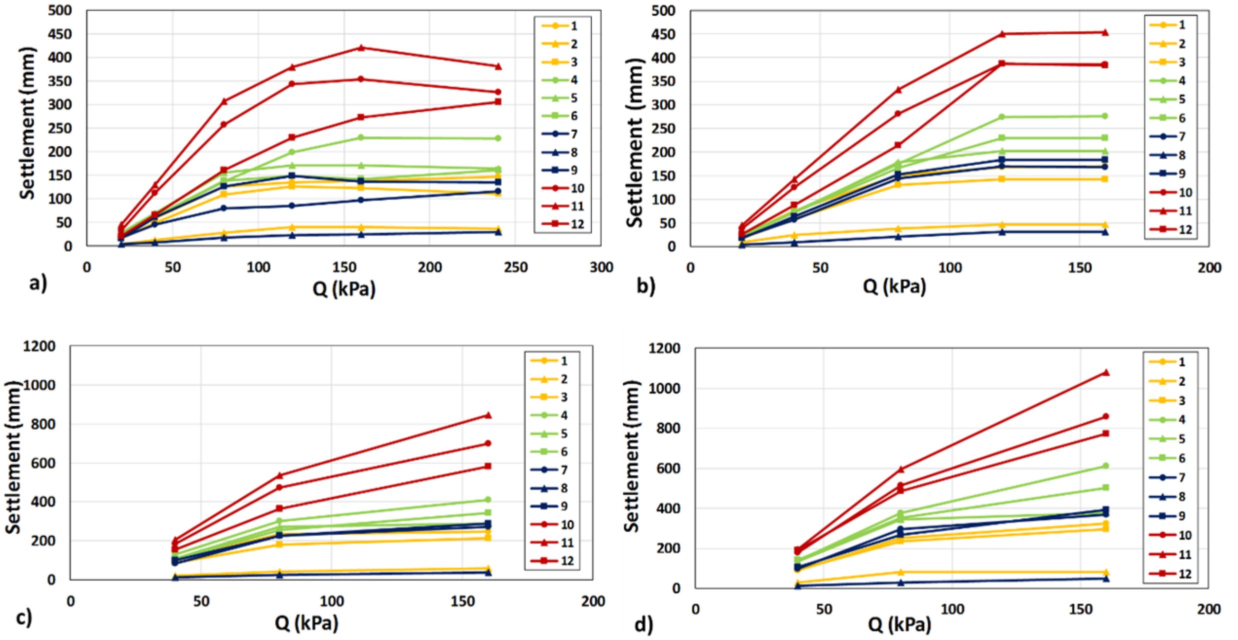

Figure 4-11 Building settlement vs building contact pressure (Q) for ground motions 1-12: (a) model with D_r=50%, H_L=3 m, B=12 m, H=12 m, and non-liquefiable crust layer thickness (HC)=2 m; (b) model with Dr= 35%, H_L=3 m, B=12 m, H=12 m and HC= 2m; (c) model with D_r=50%, H_L=6 m, B=12 m, H= 12 m and HC=2 m; and (d) model with D_r= 35%, H_L=6 m , B=12 m, H=12 m, and HC=2 m (from Macedo & Bray, 2018).

The following IMs at the base rock, far-field soil surface, and foundations were found to be the most optimal for predicting each parameter by Dashti and Karimi (2017):

- Pseudo-spectral acceleration at the site's initial fundamental period ($PSA(T_{so})$) for estimating $r_{u,peak}$ in the far-field.
- PGA for estimating $r_{u,peak}$ under the center of the structure.
- I_a for estimating $r_{u,peak}$ under the edge of the foundation.

Karimi and Dashti (2017) also identified primary IMs influencing permanent settlement, tilt, and transient inter-story drift ratios of the superstructure, which include:

- Cumulative Absolute Velocity (CAV) and Cumulative Absolute Velocity with 5 cm/s2 threshold acceleration (CAV_5) for estimating permanent foundation settlement.
- $PSA(T_{so})$ for estimating total and flexural drift ratios.
- Peak Ground Velocity (PGV) for estimating rocking drift ratio.

Luque and Bray (2017) conducted nonlinear dynamic soil-structure interaction analyses in FLAC 2D using PM4Sand to calculate and compare the settlements of two shallow-founded multistory buildings during the 2010-2011 Canterbury earthquake sequence with field measurements. The soils in the model were calibrated using laboratory and field test data for the CTUC Building and the FTG-7 Building discussed in Section 2.3.3. The study concluded that the primary mechanism of failure in the CTUC building was bearing capacity failure. This was evidenced by accumulated shear strains on the order of 8% below the building's southeast corner (Figure 4-12). Due to different soil conditions at the southeast (SE) and northeast (NE) corners of the building (refer to Section 2.3.3), significant shear strains developed in the SE corner, while the NE corner remained largely unaffected. This disparity resulted in differential settlement (Luque & Bray, 2017).

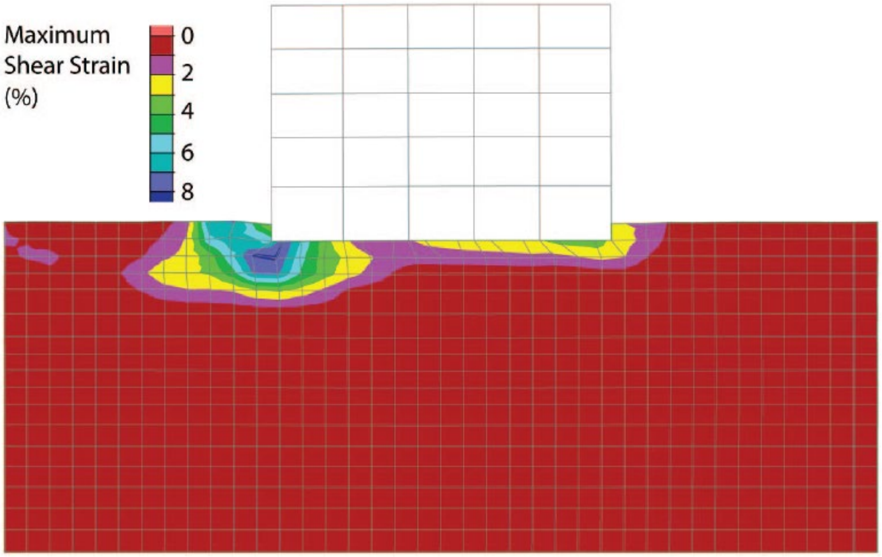

Figure 4-12 Shear strain contours for soils beneath the CTUC building at the end of the Christchurch earthquake (from Luque & Bray, 2017).

Figure 4-13 compares the calculated and measured vertical settlement profiles for seismic settlement during the strong shaking. Most of the settlement observed is attributed to shear-induced deformation. Settlement due to sand ejecta is not represented due to the limitations of continuum analysis.

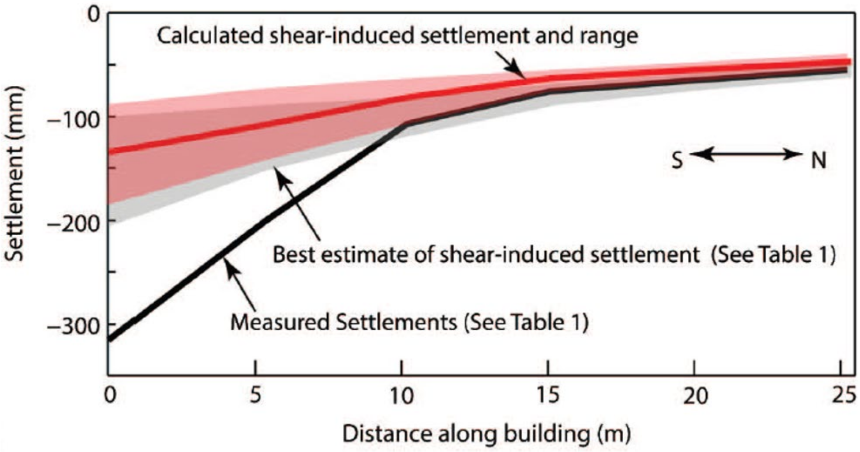

Figure 4-13 Settlement profile along the CTUC Building (from Luque and Bray, 2017).

For Building FTG-7, SSI ratcheting was identified as the main mechanism contributing to the total settlement. This was evident in the calculated displacement time histories for two exterior columns and one interior column. The exterior columns exhibited oscillatory behavior, with one side displacing downward while the other displaced upward, indicative of a rocking response (Figure 4-14). In contrast, the interior column displaced steadily downward without oscillation. High seismic demands caused lateral displacement of the soil beneath the building edges toward the free-field, inducing downward cyclic movement of the structure. Consequently, vertical displacement was larger for the exterior columns compared to the interior column.

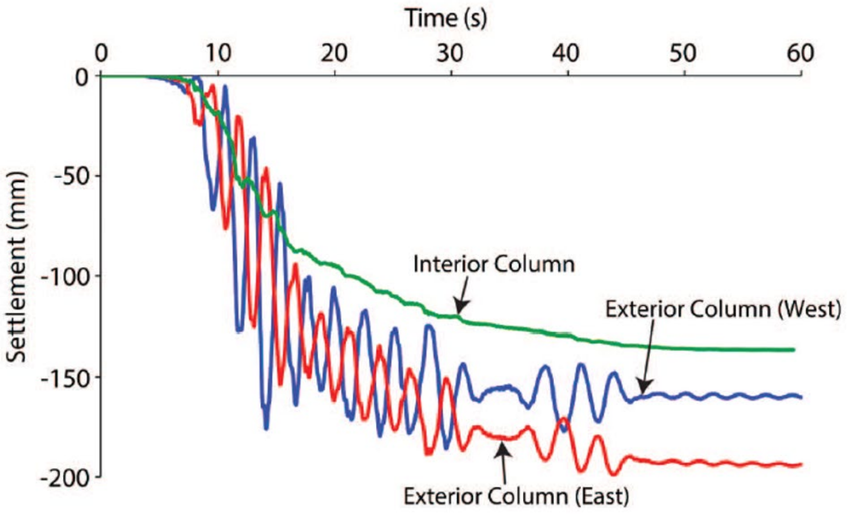

Figure 4-14 Displacement time histories at the western, eastern and interior columns in FTG-7 (from Luque & Bray, 2017).

The study also highlighted the significant impact of foundation design on structural performance. The CTUC building's foundation consisted of a relatively narrow, isolated spread footing supported on weak soil, with tie beams extending to the corner footing. In contrast, the FTG-7 building featured a robust, stiff foundation with interconnected larger spread footings in both directions, minimizing differential movement. As a result, FTG-7 experienced significantly less settlement compared to the CTUC building. Additionally, the nonuniformity of the liquefiable layer beneath the CTUC building increased permanent differential settlement compared to the more uniform layer beneath the FTG-7 building, further contributing to the disparity in settlement behavior between the two structures (Luque & Bray, 2017).

Several methods for settlement calculations have been developed through numerical analyses of case histories and sensitivity analyses. As previously mentioned, liquefaction-induced building settlement (S_t) is the combination of shear-induced settlement (S_s), volumetric-induced settlement (S_v), and ejecta-induced settlement (S_e) (Equation 15).

$$S_t = S_s + S_v + S_e \tag{15}$$

The Bray and Macedo (2017) method is often used for calculation of the shear-induced settlements. In this method, S_s is calculated using Equation below:

$$Ln(S_s) = c_1 + 4.59 * Ln(Q) - 0.42 * Ln(Q)^2 + c_2 * LBS + 0.58 * Ln\left(Tanh\left(\frac{H_L}{6}\right)\right) - 0.02 * B$$

$$+0.84 * Ln\left(CAV_{dp}\right) + 0.41 * Ln(S_a1) + \varepsilon \tag{16}$$

$$LBS = \int W * \frac{\varepsilon_{shear}}{z} dz \tag{17}$$

where S_s is measured in mm, c_1=-7.48 and c_2=0.014 for LBS>16, and c_1=-8.35 and c_2=0.072 for $LBS \leq$ 16. Liquefaction-induced Building Settlement Index (LBS) is calculated using Equation 17, where z is the depth measured from the ground surface and must be greater than 0, W is a foundation-weighting factor with W=0.0 for z less than D_f (embedment depth of the foundation) and W=1.0 otherwise. The shear strain parameter (ε_{shear}) is the liquefaction-induced free-field shear strain (in %) estimated using the Zhang et al. (2002) CPT-based procedure. In Equation 16, H_L is the cumulative thickness of liquefiable layers, Q is the foundation contact pressure (kPa), and B is the foundation width (m). The intensity measures CAV_{dp}

(g-s) and $S_a 1$ (g) are estimated for free-field ground motions at sites with no liquefactions. ε is a normal random variable with zero mean and 0.5 standard deviation in Ln units (Bray & Macedo, 2017).

S_v is often estimated using the CPT-based method by Zhang et al. (2002). S_v is calculated using Equation 18:

$$S_v = \sum_{i=1}^{j} \varepsilon_{vi} \Delta z_i \tag{18}$$

where ε_{vi} is the post-liquefaction volumetric strain for the soil sublayer i, Δz_i is thickness of the sublayer i, and j is the total number of soil sublayers. To calculate ε_{vi}, the factor of safety against liquefaction (*FS*) and a soil strength parameter such as the corrected CPT tip resistance $(q_{c1N})_{cs}$ are required. These parameters can be determined using CPT-based methods, such as Boulanger and Idriss (2014). The relationship between *FS*, ε_{vi}, $(q_{c1N})_{cs}$ is illustrated in Figure 4-15 (Zheng et al., 2002).

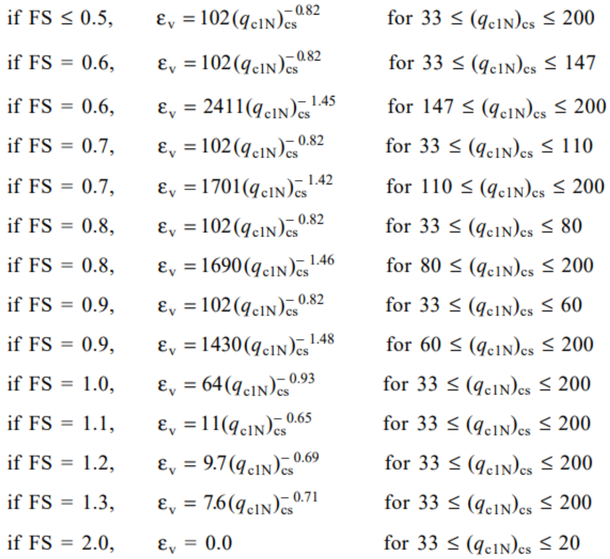

if FS ≤ 0.5, $\varepsilon_v = 102(q_{c1N})_{cs}^{-0.82}$ for $33 \le (q_{c1N})_{cs} \le 200$

if FS $= 0.6$, $\varepsilon_v = 102(q_{c1N})_{cs}^{-0.82}$ for $33 \le (q_{c1N})_{cs} \le 147$

if FS $= 0.6$, $\varepsilon_v = 2411(q_{c1N})_{cs}^{-1.45}$ for $147 \le (q_{c1N})_{cs} \le 200$

if FS $= 0.7$, $\varepsilon_v = 102(q_{c1N})_{cs}^{-0.82}$ for $33 \le (q_{c1N})_{cs} \le 110$

if FS $= 0.7$, $\varepsilon_v = 1701(q_{c1N})_{cs}^{-1.42}$ for $110 \le (q_{c1N})_{cs} \le 200$

if FS $= 0.8$, $\varepsilon_v = 102(q_{c1N})_{cs}^{-0.82}$ for $33 \le (q_{c1N})_{cs} \le 80$

if FS $= 0.8$, $\varepsilon_v = 1690(q_{c1N})_{cs}^{-1.46}$ for $80 \le (q_{c1N})_{cs} \le 200$

if FS $= 0.9$, $\varepsilon_v = 102(q_{c1N})_{cs}^{-0.82}$ for $33 \le (q_{c1N})_{cs} \le 60$

if FS $= 0.9$, $\varepsilon_v = 1430(q_{c1N})_{cs}^{-1.48}$ for $60 \le (q_{c1N})_{cs} \le 200$

if FS $= 1.0$, $\varepsilon_v = 64(q_{c1N})_{cs}^{-0.93}$ for $33 \le (q_{c1N})_{cs} \le 200$

if FS $= 1.1$, $\varepsilon_v = 11(q_{c1N})_{cs}^{-0.65}$ for $33 \le (q_{c1N})_{cs} \le 200$

if FS $= 1.2$, $\varepsilon_v = 9.7(q_{c1N})_{cs}^{-0.69}$ for $33 \le (q_{c1N})_{cs} \le 200$

if FS $= 1.3$, $\varepsilon_v = 7.6(q_{c1N})_{cs}^{-0.71}$ for $33 \le (q_{c1N})_{cs} \le 200$

if FS $= 2.0$, $\varepsilon_v = 0.0$ for $33 \le (q_{c1N})_{cs} \le 20$

Figure 4-15 Relationship between post-liquefaction volumetric strain, factor of safety against liquefaction and corrected CPT tip resistance (from Zheng et al., 2002).

In addition to direct calculation of settlement components, indices have been developed to evaluate liquefaction risks at a regional level. Bullock et al. (2021) examined the applicability of some of these indices for predicting liquefaction-induced foundation settlements. The indices include: (1) the liquefaction potential index, *LPI* (Iwasaki et al., 1978); (2) the Ishihara-inspired liquefaction potential index, LPI_{ISH} (Maurer et al., 2015); and (3) the liquefaction severity number, *LSN* (Van Ballegooy et al., 2014).

Both *LPI* and LPI_{ISH} are functions of factor of safety against liquefaction triggering (FS_{liq}) and depth (*z*) in the top 20 m (65.6 ft) of the soil profile. FS_{liq} is defined as shown in Equation 19.

$$FS_{liq} = \frac{CRR}{CSR} \tag{19}$$

where *CRR* and *CSR* are determined using liquefaction assessment methods such as Boulanger and Idriss (2014). Equations 20 through 23 provide definitions for *LPI* and LPI_{ISH}:

$$LPI = \int_0^{20m} \max\left(FS_{liq}, 1\right) \times \max(\,10 - 0.5z, 0)\,dz \tag{20}$$

$$LPI_{ISH} = \int_{H_1}^{20m} F(FS_{liq}) \times \left(\frac{25.56}{z}\right) dz \tag{21}$$

$$F(FS_{liq}) = \begin{cases} 1 - FS_{liq}, FS_{liq} < 1 \; and \; H_1.m(FS_{liq}) \le 3 \\ 0, otherwise \end{cases} \tag{22}$$

$$m(FS_{liq}) = \exp\left(\frac{5}{[25.56(1 - FS_{liq})]}\right) - 1 \tag{23}$$

where in Equation 23, $m(FS_{liq})$ adds a dependence on the thickness of non-liquefiable crust above the uppermost liquefiable layer (H_1). LSN, on the other hand, is a function of volumetric strain (ε_v) that can be calculated using methods such as Zhang et al. (2002) as described before. LSN is calculated using Equation 24:

$$LSN = \frac{1000 \int \varepsilon_v (z)}{z} dz \tag{24}$$

Bullock et al. (2021) identified *LPI_{ISH}* as the most effective geotechnical liquefaction index for estimating foundation settlement. *LPI_{ISH}* incorporates the thickness of the non-liquefiable layer in its equation, which they found to be a critical parameter in liquefaction-induced settlement calculation. In contrast, *LPI* does not include this parameter. While *LSN* could reflect this factor, current methods for calculating ε_v are based on free-field observations and do not account for structural effects (Bullock et al., 2021). For estimating foundation settlement on liquefiable deposits, the median cumulative absolute velocity (*CAV*) at outcropping rock (V_{s30}=1100 m/sec) as predicted by Campbell and Bozorgnia (2010, 2019) was found to be the optimal *IM* (Bullock et al., 2021).

Later Hutabarat and Bray (2021) introduced the Ejecta Potential Index (*EPI*), which accounts for the hydraulic process behind the formation of sediment ejecta. *EPI* is defined as shown in Equation 25.

$$EPI\ (m^3.s) = \int_{t_0}^{t_f} \int_{z_o}^{z_{GWL}} (h_{exc} - h_A)^2 dzdt \tag{25}$$

where t_0 is the initial time when the input acceleration reaches 0.05g, and t_f=150 seconds, based on previous earthquake field observations suggesting that extensive crust cracking occurs 2-3 min after the start of shaking, z_o=10 m represents the upper 10 m of the profile, which is assumed to provide most of the hydraulic demand, and z_{GWL}= depth to the water table.

The primary parameter controlling the potential for liquefied sediments to be transported to the ground surface is the magnitude of excess pressure head ($h_{exc} = EPWP/\gamma_W$) that exceeds the artesian excess head (h_A), represented as a 1:1 sloped line across the depth profile (Hutabarat & Bray, 2021).

If indices such as *EPI*, *LPI*, *LPI_{ISH}*, and *LSN* indicate significant ejecta formation, the resulting ejecta-induced building settlement (S_e) can be estimated by considering the ground loss beneath the foundation. This estimation is best approached by using relevant case histories to quantify the ejecta volume and assuming that the sediment ejecta have been entirely removed from beneath the building foundation (Bray & Macedo, 2017).

Other researchers have developed simplified methods for total settlement calculations. For example, Lu (2017) proposed a practical method for estimating liquefaction-induced settlement of shallow foundations based on Meyerhof's settlement equation. This method considers only vertical displacement, excluding rotational effects, and is unsuitable for long shallow-founded structures like embankments. However, it provides a straightforward approach for estimating total liquefaction-induced settlements for structures with shorter or medium-length shallow foundations. The total settlement (*S*) in meters is calculated using Equation 26:

$$S = C_D \frac{q}{N_{LR}} \times \left(\frac{B}{B + 0.33}\right)^2, B > 1.2\ m \qquad (26)$$

where C_D is the embedment depth correction factor (1- ($D_f/4B$)), q is the foundation's bearing pressure (kPa), B is the width of the foundation (m), and N_{LR} is the strength index of liquefied soil, which can be obtained from Figure 4-16 (Lu, 2017).

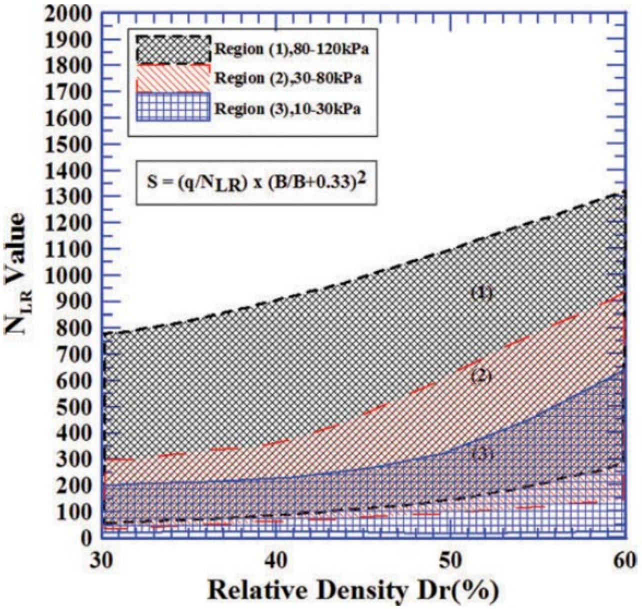

Figure 4-16 Chart of proposed N_{LR} (from Lu, 2017).

4.4 Key Insights

4.4.1 General

The results of these numerical studies identified the primary parameters for characterizing soil response, structural response, and earthquake ground motions for estimating liquefaction-induced building settlement. The primary parameters are summarized in this section, which provides the primary insights for identifying what is important for evaluating the seismic performance of shallow bridge foundations on liquefiable soil deposits. However, as these studies largely focused on the effects of shallow liquefiable soil deposits on building settlement, more work is warranted to evaluate the effects of deep liquefiable soil layers.

4.4.2 Primary Parameters for Characterizing Soil Response

These parameters were found to be most important for characterizing soil response:

- Relative Density: D_R was found to be the most critical parameter in most studies. Structure settlement was higher for loose soil deposits (i.e., $D_R < 50\%$) and structure settlement was lower for dense soil deposits (i.e., $D_R > 70\%$). Structure settlement decreased significantly as the liquefiable soil's D_R increased from around 50% to 70%. The amount of structure settlement is only moderately sensitive to variations in the relative density of the liquefiable soil layer in very loose to loose soil deposits or in dense to very dense soil deposits. Shallow foundation settlement is sensitive to small variations in relative density in medium-density sand deposits. The importance of this parameter is evident in its inclusion in many settlement calculation methods. While it may not always be explicitly considered, parameters such as the CPT tip resistance or SPT *N*-value are often utilized (e.g., Zhang et al., 2002; Lu, 2017), as they are correlated with D_R.

- Thickness of the Liquefiable Layer: The thickness of the liquefiable layer affects the liquefaction-induced shear component and volumetric component of structure settlement up to a threshold thickness, beyond which the shear component of settlement does not continue to increase as the layer thickness increases. The shear component of liquefaction-induced structure settlement is generally more significant than the volumetric component of settlement. Thus, thicker layers generally lead to greater settlement until the threshold is reached, beyond which further increases in layer thickness only modestly increase structure settlement. This threshold is influenced by factors such as the structure's bearing pressure, width of the foundation, height of the structure, and depth to the liquefiable layer.

- Depth to the Liquefiable Layer: As the depth to the top of the liquefiable layer increases, structure settlement decreases due to reduced shear deformation from SSI-ratcheting and partial bearing loss. A thicker, more competent non-liquefiable crust layer better supports the shallow foundation of a structure. However, Karimi et al. (2018) recognized that if the non-liquefiable crust has low permeability, settlement could increase in some cases because it prevents the dissipation of excess pore pressure, depending on the intensity of the ground motion, among other factors.

- Stratigraphy and Soil Profile Characteristics: The uniformity or nonuniformity of the liquefiable layer, along with the depth to the water table and the permeability of the non-liquefiable crust, are critical factors influencing settlement behavior. For example, during the Christchurch earthquake, the nonuniformity of the liquefiable layer beneath the CTUC building led to significant differential settlement. Additionally, low permeability in the crust and surrounding layers can hinder the dissipation of excess pore water pressure, which contributes to bearing capacity degradation and post-liquefaction sedimentation. Karamitros et al. (2013) highlighted that this degradation continues throughout shaking as long as it takes the excess pore pressure to dissipate. These observations emphasize the importance of understanding the stratigraphy and soil profile characteristics in estimating liquefaction-induced structure settlement.

4.4.3 Primary Parameters for Characterizing Structural Response

These parameters were found to be most important for characterizing structural response:

- Structure Contact Pressure: The contact pressure of the structure's foundation is typically the most significant structural parameter affecting its response, especially during strong earthquake shaking. Structure settlement increases as the building contact pressure increases, up to a point. After this point, the impact of contact pressure plateaus. The threshold of the structure contact pressure effect on building settlement is influenced by soil relative density and earthquake shaking intensity.

- Structure Width, Length, and Height: Increasing the foundation width (*B*) or its area (i.e., length (*L*) x *B*) reduces structure settlement at lower shaking intensities. Increasing the length-to-width aspect ratio (*L/B*) of the mat foundation reduces shear strains and settlement for lower levels of ground shaking. For taller structures, height (*H*) becomes more critical due to increased rocking tendencies. The effective height-to-width ratio (*H/B*) can also influence the dynamic response of the structure during shaking. Increasing the width of the foundation relative to the thickness of the liquefiable layer (B/H_L) decreases shear-induced settlement. Increasing the width to the depth of the liquefiable layer (B/D_L) can induce rocking behavior in structures and increases the settlement. The width of the foundation is a crucial parameter, as it is directly used in calculating shear-induced settlement while also playing an indirect role in volumetric-induced settlement.

- Foundation Embedment Depth: Structure settlement decreases as the foundation embedment depth of the building increases in most cases.

- Structural Mass: Structural settlement increases as the inertial mass of the structures increases. However, structural mass is correlated to the structure contact pressure and its height, so it may not need to be considered in addition to these parameters for conventional structures.

4.4.4 Primary Parameters for Characterizing Earthquake Ground Motions

Several ground motion intensity measures were found to significantly influence the amount of liquefaction-induced structure settlement. The intensity, frequency content, and duration of earthquake strong shaking influences its effects on the ground and structures. Thus, ground motion parameters that capture all these characteristics tend to perform best in estimating liquefaction-induced structure settlement. Of these 'combined' ground motion parameters, the most promising *IM*s are:

- *SIR* correlates well with the initiation, rate, and amount of liquefaction-induced structure settlement.

- I_a and *CAV* (either *CAV*, CAV_5 or CAV_{dp}) are also effective and efficient combined ground motion parameters. Structure settlement increases as these IMs increase.

Some 'single characteristic' ground motion parameters perform well in estimating liquefaction-induced structure settlement. Of these the most promising IMs are:

- S_a1 captures important aspects of the site response of most deep soil deposits, and it correlates well with the amount of liquefaction-induced structure settlement. $PSA(T_{so})$ may capture these characteristics better, but it requires an estimate of the site period, which requires additional information.

- *PGA* has been traditionally used with earthquake magnitude to assess liquefaction triggering. Hence, it is typically available at the start of a liquefaction assessment and can be used to estimate the threshold of liquefaction triggering and thus the threshold of structure settlement. *PGV* also provides useful ground motion intensity information; it has been found to correlate well with structural rocking drift ratio.

Chapter 5 KEY FINDINGS

This chapter summarizes the key findings from previous field case histories, experiments, and numerical simulations to highlight the critical mechanisms and parameters influencing the performance of shallow foundations on liquefiable soils under strong ground motions. While research specifically targeting bridges is limited, transferable insights from studies on buildings with shallow foundations provide valuable insights to understanding bridge performance.

Previous field case histories have demonstrated that lateral spreading is one of the most common failure mechanisms in bridges located on liquefiable soils. There are several cases where pile foundations failed to adequately support bridge superstructures during significant liquefaction-induced lateral spreading. This phenomenon can exert lateral loads on piles extending from the liquefiable soil layer into a firmer layer, leading to damage such as bending, shear deformations, and ultimately the rotation of pile-supported bridge abutments. To mitigate hazards associated with lateral spreading, ground improvement measures should be considered when using shallow foundations. Designing shallow foundations for bridges at sites with unmitigated lateral spreading hazards is unlikely to be cost-effective. Therefore, shallow-founded bridges should generally be avoided under such conditions. This research study focuses on cases where lateral spreading does not pose a hazard to shallow foundations.

Liquefaction-induced settlement consists of three distinct types: shear-induced settlement (S_s), volumetric-induced settlement (S_v), and ejecta-induced settlement (S_e). Several researchers (e.g., Bray & Dashti, 2014) have emphasized that total settlement near or beneath a structure exceeds free-field settlement, primarily because shear-induced settlement is the predominant mechanism contributing to structural settlement. Centrifuge tests also demonstrated that post-liquefaction reconsolidation plays a minor role in the overall settlement. However, the relative significance of each settlement mechanism varies based on the characteristics of the earthquake motions, the properties of the liquefiable soil, and the structural characteristics of the building.

Critical soil parameters influencing settlement include relative density (D_r), thickness of the liquefiable layer (H_L), depth to the liquefiable layer (D_L), and site stratigraphy. Relative density emerged as the most significant parameter in most studies. Loose materials ($D_r < 50\%$) result in higher settlement, while dense materials ($D_r > 70\%$) lead to lower settlement. Shallow foundations were shown to be particularly sensitive to variations in relative density within the range of 50% to 70%.

The thickness of the liquefiable layer influences both volumetric and shear-induced settlements up to a threshold, beyond which the shear component of settlement does not continue to increase. This threshold depends on several factors, including the structure's bearing pressure, foundation width, structure height, and depth to the liquefiable layer.

Depth to the liquefiable layer (D_L) is another critical parameter affecting soil response. As the depth to the top of the liquefiable layer increases, structural settlement decreases due to reduced shear deformation caused by soil-structure interaction (SSI) ratcheting and partial bearing loss. Shallow liquefiable layers tend to increase a structure's propensity for rocking, while deep liquefiable layers ($B/D_L < 1$) induce settlement primarily through lateral soil displacement beneath a bulb of stiffer soil extending roughly $1B$ below the foundation. For heavier structures subjected to prolonged strong shaking, embedment accumulation may occur, accompanied by rocking behavior.

A thicker and more competent non-liquefiable crust layer generally enhances support for shallow foundations. However, stratigraphic factors such as the permeability of soil layers, depth to the water table, and the uniformity of the soil profile can significantly influence settlement. Low-permeability non-liquefiable crusts may exacerbate settlement by inhibiting the dissipation of excess pore pressure, leading to bearing capacity degradation and post-liquefaction sedimentation, especially under intense ground motions. Additionally, nonuniform stratigraphy can result in differential settlements. Consequently, the site's stratigraphic characteristics play a crucial role in settlement behavior.

Structural parameters also play a significant role in the settlement mechanism. Key contributors include foundation bearing pressure (q), foundation width (B), foundation area (B x L), the structure's aspect ratio (height of the structure to foundation width, H/B), the material composition of the foundation, the structure's mass, foundation embedment depth, and the spacing between foundations. Among these, the structure's contact pressure (q) is often the most influential parameter affecting structural response during strong earthquake shaking. Past centrifuge experiments have shown that during moderate shaking events, foundations with higher bearing pressures experienced less settlement than those with lighter bearing pressures and even less than the free-field settlement.

Structure settlement tends to increase with higher bearing pressure until it reaches a plateau, with the threshold of contact pressure being influenced by factors such as soil relative density and the intensity of seismic shaking. Increasing the foundation width (B) or foundation area can lead to higher volumetric settlement but can simultaneously reduce shear-induced settlement. Because shear deformation is the primary mechanism driving structure settlement, expanding the foundation area at lower shaking intensities can help minimize overall settlement.

However, increasing the aspect ratio of a building (H/B) can amplify differential settlement and tilting, posing a risk to structural stability. Similarly, a higher structural mass increases inertial forces during seismic events, ultimately leading to greater settlement. Conversely, increasing the foundation embedment depth has been shown to reduce settlement.

The design of a shallow foundation also plays a vital role in mitigating liquefaction-induced damage. A strong and stiff shallow foundation can effectively accommodate ground settlement through uniform settlement or rigid-body tilt without causing internal distortion to the overlying structure. However, excessive rigid-body tilt can lead to toppling failures, which is particularly detrimental to bridges, as the tilt of their piers directly impacts their stability and functionality. Conversely, flexible foundations can create issues, such as sagging which damages the foundation. This highlights the importance of finding an optimal balance between stiffness and flexibility to ensure the foundation can perform effectively under seismic conditions without introducing additional failure modes such as toppling.

The distance between adjacent structures can significantly influence ground deformation, leading to issues such as hogging or differential settlements. Observations in Iskenderun during the 2023 Kahramanmaraş earthquake revealed that areas with closer building proximity experienced larger building settlement compared to those with greater spacing, despite having similar subsurface conditions. This finding suggests that the spacing between shallow foundations, such as those supporting bridge piers, plays a critical role in settlement-related damage.

Ground motion characteristics, including intensity, frequency content, and duration, significantly affect liquefaction-induced structure settlement. Combined intensity measures, such as SIR, I_a, and CAV, provide efficient settlement estimates, while single characteristic measures like S_a1, PGA, and PGV also correlate well with settlement outcomes. Among these, the median CAV as estimated by ground motion models (GMMs) is one of the most efficient intensity measures (IMs) for estimating foundation settlement on liquefiable deposits.

In conclusion, this research aimed to investigate the parameters contributing to liquefaction-induced settlement of shallow-founded structures, with a specific focus on bridges, to identify key mechanisms. By analyzing field case histories, experimental, and numerical studies, critical parameters related to soil characteristics, structural features, and ground motion effects were identified. Further research is warranted to fully understand these mechanisms and to develop effective mitigation strategies for bridges subjected to the liquefaction hazard.

REFERENCES

Adamidis, O., & Madabushi, S. (2018). Deformation mechanisms under shallow foundations on liquefiable layers of varying thickness. *Geotechnique*(7), 602-613. Retrieved from https://doi.org/10.1680/jgeot.17.P.067

Allmond, J., Kutter, B. L., Bray, J., & Hayden, C. (2015). New Database for Foundation and Ground Performance in Liquefaction Experiments. *Earthquake Spectra, 31*(4), 2485-2509.

Arnold, C., Macedo, J., Bray, J., Moug, D., Atalay, F., Bassal, P., . . . Durgunoglu, T. (2025). Field Characterization of Areas in Iskenderun Affected by Liquefaction during the 2023 Kahramanmaras Earthquake. *Earthquake Spectra*, submitted, under review.

Ansal, A., Abrahamson, N., Bardet, J. P., Barka, A., Baturay, M. B., Berilgen, B. M., . . . Youd, L. (1999). *Initial Geotechnical Observations of the August 17, 1999, Kocaeili Earthquake.* GEER Association.

Beaty, M. H. (2021). *Itasca* . Retrieved from Itasca UDM .

Berrill, J. B., Christensen, S. A., Keenan, R. P., Okada, W., & Pettinga, J. R. (2001). Case Study of Lateral Spreading Forces on a Piled Foundation. *Geotechnique, 51*(6), 501-517.

Bertalot, D., & Brennan, A. (2015). Influence of Initial Stress Distribution on Liquefaction-Induced Settlement of Shallow Foundations. *Géotechnique, No.5*, 418-428. doi:http://dx.doi.org/10.1680/geot.SIP.15.P.002

Bhattacharya, S., Tokimatsu, K., Goda, K., Sarkar, R., Shadlou, M., & Rouholamin, M. (2014). Collapse of Show Bridge During 1964 Niigata earthquake: A Quantitative Reappraisal on the Failure Mechansims. *Soil Dynamics and Earthquake Engineering* .

Boulanger, R. W., & Wijewickreme, D. (2019). Calibration of a constitutive model for the cyclic loading responses of Fraser River Delta silt. *International Society for Soil Mechanics and Geotechnical Engineering.* Rome, Italy.

Boulanger, R., & Idriss, I. M. (2014). *CPT and SPT Based Liquefaction Triggering Procedures.* UC Davis Center for Geotechnical Modeling.

Boulanger, R., & Ziotopoulou, K. (2018). *PM4SILT (Version 1): A Silt Plasticity Model for Earthquake Engineering* . Department of Civil and Environmental Engineering University of California, Davis.

Boulanger, R., & Ziotopoulou, K. (2022). *PM4SAND (VERSION 3.2): A Sand Plasticity Model for Earthquake Engineering Applications.* Department of Civil and Environmental Engineering University of California, Davis.

Bray, J. D., & Dashti, S. (2014). Liquefaction-induced Building Movements. *Bulletin of Earthquake Engineering, 12*, 1129-1156. doi:10.1007/s10518-014-9619-8

Bray, J. D., & Macedo, J. (2017). Simplified Evaluation of Liquefaction-Induced Building Settlements. *Geotechnical Earthquake Engineering and Soil Dynamics V.*

Bray, J. D., & Sancio, R. B. (2004). Subsurface Characterization at Ground Failure Sites in Adapazari, Turkey. *Journal of Geotechnical and Geoenvironmental Engineering* . doi:10.1061/(ASCE)1090-0241(2004)130:7(673)

Bray, J. D., & Sancio, R. B. (2009). *Performance of Buildings in Adapazari during the 1999 Kocaeli, Turkey Earthquake.* Taylor & Francis Group.

Bray, J. D., Markham, C. S., & Cubrinovski, M. (2017). Liquefaction assessments at shallow foundation building sites in the Central Business District of Christchurch, New Zealand . *Soil Dynamics and Earthquake Engineering* .

Bray, J., & Frost, D. (2010). *Geo-engineering Reconnaissance of the 2010 Maule, Chile Earthquake.* GEER Association Report No. GEER-022.

Bray, J., Cubrinovski, M., Zupan, J., & Taylor, M. (2014). Liquefaction Effects on Buildings in the Central Business District of Christchurch. *Earthquake Spectra, 30*(1), 85-109.

Bray, J., Rollins, K., Hutchinson, T., Verdugo, R., Ledezma, C., Mylonakis, G., . . . Candia, G. (2012). Effects of ground failure on buildings, ports, and industrial facilities. *Earthquake Spectra*(J 28(S1):S97–S118).

Bullock , Z., Dashti, S., Liel, A. B., & Porter, A. K. (2021). Can geotechnical liquefaction indices serve as predictors of foundation settlement? *Earthquake Spectra, 37*(4), 2271-2287. doi:DOI: 10.1177/8755293021994844

Campbell, K., & Bozorgnia, Y. (2010). ground motion prediction equation for the horizontal component of cumulative absolute velocity (CAV) based on the PEER-NGA strong motion database. *Earthquake Spectra*, 635-650.

Campbell, K., & Bozorgnia, Y. (2019). Ground motion models for the horizontal components of Arias intensity (AI) and cumulative absolute velocity (CAV) using the NGA-West2 database. *Earthquake Spectra, 35*(3), 1289-1310.

Coetzee, C. J. (2001). Reviewer: Calibration of Discrete Element Method. *Elsevier*. doi:http://dx.doi.org/10.1016/j.powtec.2017.01.015

Cubrinovski, M., & Ishihara, K. (1998). Modeling of Sand behavior based on state concept . *Japanese Geotechnical Society*.

Cubrinovski, M., & Ishihara, K. (1998). State Concept and Modified Elastiplasticity for Sand Modeling . *Japanese Geotechnical Society*.

Cubrinovski, M., Winkley, A., Haskell, J., Palermo, A., Wotherspoon, L., Robinson, K., . . . Hughes, M. (2014). Spreading-Induced Damage to Short Span Bridges in Christchurch, New Zealand. *Earthquake Spectra, 30*(1), 57-83. doi:10.1193/030513EQS063M]

Dafalias, Y. F., & Manzari, M. T. (2004). Simple Plasticity Sand Model Accounting for Fabric Change Effects. *Journal of Engineering Mechanics*. doi:10.1061/(ASCE)0733-9399(2004)130:6(622)

Dashti, S., & Bray, J. (2013). Numerical Simulations of Building Response on Liquefiable Sand. *Journal of Geotechnical and Geoenvironmental Engineering, 139*(8).

Dashti, S., & Karimi, Z. (2017). Ground Motion Intensity Measure to Evaluate I: The Liquefaction Hazard in the Vicinity of shallow-founded structures. *Earthquake Engineering Research Institute*. doi:10.1193/103015EQS162M

Dashti, S., Bray, J. D., Pestana, J. M., Riemer, M., & Wilson, D. (2010b). Centrifuge Testing to Evaluate and Mitigate Liquefaction-Induced Building Settlement Mechanisms. *Journal of Geotechnical and Geoenvironmental Engineering, 136*, 918-929.

Dashti, S., Bray, J., Pestana, J. M., Riemer, M., & Wilson, D. (2010a). Mechanisms of Seismically Induced Settlement of Buildings With Shallow Foundations on Liquefiable Soil. (ASCE, Ed.) *Journal of Geotechnical and Geoenvironmental Engineering*, 151-164.

Elbadawy, M. A., Zhou, Y.-G., & Liu, K. (2022). A modified pressure dependent multi-yield surface model for simulation of LEAP-Asia-2019 centrifuge experiments. *Soil Dynamics and Earthquake Engineering*.

Elgamal, A., Yang, Z., & Parra, E. (2002). Computational Modeling of cyclic mobility and post0liquefaction site response. *Soil Dynamics and Earthquake Engineering*.

Engineering, S. R. (2023). *Soga Research Group Berkeley Engineering* . Retrieved from https://geomechanics.berkeley.edu/research/comp-geo/mpm/#:~:text=MPM%20is%20a%20particle%2Dbased,and%20a%20fixed%20computational%20grid

Hamada, M., & O'Rourke, T. D. (1992). *Case Studies of Liquefaction and Lifeline Performance During Past Earthquakes.* National Center for Earthquake Engineering Research.

Hayden, C. P., Zupan, J. D., Bray, J. D., Allmond, J. D., & Kutter, B. L. (2015). Centrifuge Tests of Adjacent Mat-Supported Buildings Affected by Liquefaction. *Journal of Geotechnical and Geonvironmental Engineering*.

Hutabarat, D., & Bray, J. (2021). Estimating the Severity of Liquefaction Ejecta Using theCone Penetration Test. *Journal of Geotechnical and Geoenvironmental Engineering, 148*(3). Retrieved from https://doi.org/10.1061/(ASCE)GT.1943-5606.000274

Ishii, Y., & Tokimatsu, K. (1988). Simplified procedures for the evaluation of settlements of structures during earthquakes. *9th world conference on earthquake engineering*, *3*, pp. 95-100. Tokyo-Kyoto, Japan.

Itasca Consulting Group, Inc. (2019). *FLAC — Fast Lagrangian Analysis of Continua, Ver. 8.1.* Minneapolis: Itasca.

Iwasaki, T., Tatsuoka, F., Tokida, K., & Yasuda, S. (1978). A practical method for assessing soil liquefaction potential based on case studies at various sites in Japan. *Proceedings of the second international conference on Microzonation*, *2.* San Francisco, CA.

Karamitros, D. K., Bouckovalas, G. D., Chaloulos, Y. K., & Andianopoulos, K. (2013). Numerical Analysis of Liquefaction-Induced Bearing Capasity Degradation of Shallow Foundations on a two-layered Soil Profile. *Soil Dynamics and Earthquake Engineering*.

Karimi, Z., & Dashti, S. (2017). Ground Motion Intensity Measure to Evaluate II: the Performance of Shallow-Fuonded Structures on Liquifiable Ground. *Earthquake Engineering Research Institute* .

Karimi, Z., Dashti, S., Bullock, Z., Portera, K., & Liel, A. (2018). Key predictors of structure settlement on liquefiable ground: a numerical parametric study. *Soil Dynamics and Earthquake Engineering* .

Khosravifar, A., Elgamal, A., Lu, J., & Li, J. (2018). A 3D model for eathquak-induced liquefaction triggering and post-liquefaction response. *Soil Dynamics and Earthquake Engineering, 110*, 43-52.

Khosravifar, A., Elgamal, A., Lu, J., & Li, J. (2022). A 3D model for earthquake-induced liquefaction triggering and post-liquefaction response. *Soil Dynamics and Earthquake Engineering*.

Kutter, B. (1992). Dynamic Centrifuge Modeling of Geotechnical Structures. *Transportation Research Record*. Retrieved from http://onlinepubs.trb.org/Onlinepubs/trr/1992/1336/1336-004.pdf

Ledezma, C., Hutchinson, T., Ashford, S. A., Moss, R., Arduino, P., Bray, J. D., . . . Rollins, K. (2012). Effects of Ground Failure on Bridges, Roads, and Railroads. *Earthuake Spectra, 28*. doi:10.1193/1.4000024

Liu, L., & Dobry, R. (1997). Seismic Response of Shallow Foundation on Liquefiable Sand. *Journal of Geotechnical and Geoenvironmental Engineering, 123*(6).

Lu, C. (2017). A simplified Calculation Method for Liquefaction-Induced Settlement of Shallow Foundation. *Journal of Earthquake Engineering*, 1385-1405. doi:DOI: 10.1080/13632469.2016.1264327

Luque, R. X. (2017). *PhD Thesis: Numerical Analyses of Liquefaction-Induced Building Settlement.* University of California, Berkeley.

Luque, R., & Bray, J. D. (2017). Dynamic Analysis of Two Buildings Founded on Liquefiable Soils During the Canterbury Earthquake Sequence. *Journal of Geotechnical and Geoenvironmental Engineering*. doi:10.1061/(ASCE)GT.1943-5606.0001736

Macedo, J., & Bray, J. (2018). Key Trends in Liquefaction-Induced Building Settlement . *Journal of Geotechnical and Geoenvironmental Engineering*.

Mason, H. B., Trombetta, N. W., Chen, Z., Bray, J. D., Hutchinson, T. C., & Kutter, B. L. (2013). Seismic soil-foundation-structure interaction observed in geotechnical centrifuge experiments. *Soil Dynamics and Earthquake Engineering*.

Maurer, B., Green, R., Cubrinovski, M., & Bradley, B. (2014). Evaluation of the liquefaction potential index for assessing liquefaction hazard in Christchurch, New Zealand. *Journal of Geotechnical and Geoenvironmental Engineering*.

McKenna, F., Fenves, G. L., & Scott, M. H. (2000). Open System for Earthquake Engineering Simulation. University of California, Berkeley. Retrieved from http://opensees.berkeley.edu.

Moug, D. M., Bray, J. D., Bassal, P., Macedo, J., Ulmer, K., Cetin, K. O., . . . Bikce, M. (2024). Liquefaction-induced ground and building interactions in Iskenderun from the 2023 Kahramanmaras earthquake sequence. *Eearthquake Spectra, 40*(2), 913-938. doi:10.1177/87552930241232994

Potts, D., & Zdravkovic, L. (1999). *Finite Element Analysis in Geotechnical Engineering: Theory and Application.*

Samtani, N., Nowatzki, E., & Mertz, D. (2010). *Selection of Spread Footings on Soils to Support Highway Brudge Structures (FHWA-RC-TD-10-001).* U.S. Department of Transportation Federal Highway Administration.

Seed, R. B., Cetin, K. O., Moss, R., Kammerer, A. M., Wu, J., Pestana, J. M., . . . Faris, A. (2003). *Recent Advances in Soil Liquefaction Engieering: A Unified and Consistent Framework.*

Solowski, W. T., Berzins, M., Coombs, W. M., Guilkey, J. E., Matthias, M., Tran, Q., . . . Soga, K. (2021). Chapter two-Material Point Method: Overview and Challenger ahead. *Elsevier*. doi:https://doi.org/10.1016/bs.aams.2020.12.002

Stewart, D. P., Chen, Y. R., & Kutter, B. L. (1998). Experience with the Use of Methylcellulose as a Viscous Pore Fluid in Centrifuge Models. (ASTM, Ed.) *Geotechnical Testing Journal, 21*(4), 365-369. doi:https://doi.org/10.1520/GTJ11376J

Tanaka, K., Nishida, M. T., & Kunimochi, T. T. (2001). Numerical and Experimental studies for the impact of projectiles on granular materials. *Elsevier*. doi:https://doi.org/10.1016/S0167-3785(01)80028-2

Tokimatsu, K., Suzuki, H., Katsumata, K., & Tamura, S. (2013). Geotechnical Problems in the 2011 Tohoku Pacific Earthquakes. *International Conference on Case Histories in Geotechnical*.

Trombetta, N. W., Mason, H. B., Hutchinson, T. C., Zupan, J. D., Bray, J. D., & Kutter, B. L. (2014). Nonlinear Soil-Foundation-Structure and Structure-Soil-Structure Interaction: Centrifuge Test Observations. *Journal of Geotechnical and Geoenvironmental Engineering*. doi:10.1061/(ASCE)GT.1943-5606.0001074.

Van Ballegooy, S., Malan, P., Lacrosse, V., Jacka, M., Cubrinovski, M., Bray, J., . . . Cowan, H. (2014). Assessment of liquefaction-induced land damage for residential Christchurch. *Earthquake Spectra, 30*(1), 31-55.

Voyagaki, E., Kishida, T., Aldulaimi, R., & Mylonakis, G. (2023). Integration and Calibration of UBCSAND model for drained monotonic and cylic triaxial compression of aggregates. *Soil Dynamics and Earthquake Engineering*.

Yen, W.-H. P., Chen, G., Buckle, I., Allen, T., Alzamora, D., Ger, J., & Arias, J. G. (2011). *Post-Earthquake Reconnaissance Report on Transportation Infrastructure: Impact of the February 27, 2010, Offshore Maule Earthquake in Chile.* Federal Highwat Administration Research and Technology.

Youd, L. (1993). Liquefaction-Induced Damage to Bridges. *Transportation Research Record*.

Youd, L., & Perkins, D. (1978). Mapping Liquefaction-Induced Ground Failure Potential. *Journal of the Geotechnical Engineering Division*.

Zhang, G., Robertson, P., & Brachman, R. (2002). Estimating liquefaction-induced ground settlements from CPT for level ground. *Canadian Geotechnical Journal*. doi: 10.1139/T02-047